IPP-Report

Max-Planck-Institut
für Plasmaphysik

Annabelle Spanier

Characterisation of Neutral Beam Injection into the Wendelstein 7-X Stellarator

IPP 2021-06
Februar 2021

Technische
Universität
Berlin

CHARACTERISATION OF NEUTRAL BEAM INJECTION INTO THE WENDELSTEIN 7-X STELLARATOR

MASTERARBEIT

vorgelegt von

Annabelle Spanier

18. September 2020

Zentrum für Astronomie und Astrophysik
Technische Universität Berlin

ERSTPRÜFER:
Prof. Dr. Robert C. Wolf

ZWEITPRÜFER:
Prof. Dr. Dieter Breitschwerdt

BETREUER:
Dr. Dirk Hartmann

Annabelle Spanier: *Characterisation of Neutral Beam Injection into the Wendelstein 7-X Stellarator,* © 18. September 2020

ERSTGUTACHTER: Prof. Dr. Robert C. Wolf
ZWEITGUTACHTER: Prof. Dr. Dieter Breitschwerdt
BETREUER: Dr. Dirk Hartmann

ACKNOWLEDGEMENTS

This research was carried out at the Max Planck Institute for Plasma Physics in Greifswald and I want to sincerely thank everyone who was involved. I was always welcomed cordially and given help whenever I needed it. There are some people I would like to thank in particular.

First and foremost, I would like to thank Prof. Robert C. Wolf, for giving me the wonderful opportunity to write this thesis and steered me in the right direction whenever I needed it with his sense for the whole picture. He supported me with fruitful discussions and good advice during the whole time and especially in the end to refine this thesis. Additionally, I would like to thank my second university supervisor Prof. Dieter Breitschwerdt. Furthermore, I would like to thank my supervisor Dr. Dirk Hartmann. The door to his office was always open whenever I ran into a trouble spot or had a question about my research or writing. I cannot be thankful enough for his guidance and support through each stage of the process. The inspiring discussions have strongly contributed in expanding my knowledge and my horizons in such an interesting and challenging research field.

I would also like to thank the experts who were involved in the validation survey for this research project for many inspiring discussions and data support: Péter Pölöskei, Dr. Norbert Rust, Dr. Paul McNeely, Dr. Simppa Äkäslompolo, Dr. Oliver Ford, Roland Kairys and Peter Rong from IPP Greifswald and Dr. Nicolaas den Harder, Dr. Christian Hopf and Guillermo Orozco from Garching. Without their passionate participation and input, this research could not have been successfully conducted.

Additionally, I am grateful for the support and warm welcome by the whole E3 team, especially the NBI group, and by the Python User Group and the Young Reasearchers group at IPP Greifswald.

In my office, Lilla Vanó, Dr. Felix Warmer and Dr. Fabian Wilde always made sure the atmosphere was good and otherwise bravely endured my moaning and groaning and answered all kinds of questions. Speaking of colleagues, I have to mention Jan Paul Koschinsky, Marco Zanini, Juan F. Guerrero Arnaiz, Dr. Lukas Rudischhauser and Dr. Daniel F. Böckenhoff. They stayed with me through the ups and downs that such a master thesis comes with. Thanks for the motivation, the many suggestions, interesting conversations and the nice time together.

A special and immeasurable thankfulness must be, finally, given to all the people that, during my life and my studies, believed in me, because I would only have been a shadow of the woman I am now without the teachings they gave me, the trust they placed in me, and the moments spent together during these years. Big thanks to my whole family, for always respecting my choices and for always supporting me in whatever I did, especially to my parents, Anna and Gerd, and to my brother Robin. I am infinitely grateful to Philipp. He is a wonderful man and the best person one can have as a partner. Thanks to all my friends for listening, motivating and never making me feel alone during each step of the long and winding road that brought me up to here, especially to Pia, Rebecca and the Octopussies.

... and to many others whose names and deeds are not mentioned here. I thank you!

ABSTRACT

Neutral Beam Injection (NBI) was used at the superconducting optimised stellarator Wendelstein 7-X (W7-X) for the first time during the experimental campaign OP1.2b in 2018. The injector is equipped with two inductively coupled ion sources that can accelerate hydrogen ions up to 54 kV. The performance of this injector is investigated. The injected power of the NBI system is of particular interest for evaluating the energy confinement time, which is one of the three parameters of the fusion product. But the injected power P_{inj} cannot be measured directly. In this thesis, the average injected power is determined with calorimetry to be $P_{inj} \approx (3.1 \pm 0.8)\,\mathrm{MW}$ for a full power NBI pulse. Therefore, the efficiency of the NBI system is about 33 %. This injected power leads to an energy confinement time of $\tau_E \approx 150\,\mathrm{ms}$ for pure NBI heating plasma experiments at W7-X with an electron density of about $4 \times 10^{19}/\mathrm{m}^3$ and an ion and electron temperature of $T_i \approx T_e \approx 1.3\,\mathrm{keV}$.

Moreover, the qualitative dependence of the neutralisation efficiency on the target thickness and the kinetic energy per beam atom is confirmed for this NBI system.

All in all, $(89 \pm 6)\,\%$ of the generated beam power of a test pulse can be accounted for with calorimetric analysis of the heat loads on the individual NBI components. Perspectives to improve this power accountability of the NBI system are identified. The heat loads at the liners of the deflection magnet need to be investigated to fully understand the energy and particle flow in the magnet area and to allow optimisation of the deflection process for future NBI operation. The calorimetry of the components in the W7-X vessel can be improved by temperature and flow rate sensors with higher accuracy and separate measurement of the region of interest. Additionally, it is required to determine the exact acceleration voltage and extracted current to reduce the error on the power accountability and the NBI heating power.

ZUSAMMENFASSUNG

Die Neutralteilchen-Injektions-Heizung (NBI) am supraleitenden und optimierten Stellarator Wendelstein 7-X (W7-X) wurde zum ersten Mal während der Experimentkampagne OP1.2b in 2018 eingesetzt. Der Injektor ist mit zwei induktiv gekoppleten Ionenquellen ausgestattet, die einfache Wasserstoffionen mit bis zu 54 kV beschleunigen können. Die Performance dieses Injektors wurde untersucht. Die injizierte Leistung des NBI-Systems ist besonders für die Bestimmung der Energieeinschlusszeit relevant, welche eine der drei Parameter des Fusionsprodukts ist. Allerdings kann die injizierte Leistung P_{inj} nicht direkt gemessen werden. Im Rahmen dieser Arbeit wurde die gemittelte injizierte Leistung eines NBI-Pulses mit voller Leistung zu $P_{inj} \approx (3.1 \pm 0.8)$ MW bestimmt. Die Effizienz des NBI-Systems liegt damit bei rund 33 %. Diese NBI Leistung wurde in ein Plasma in W7-X mit einer Elektronendichte von etwa $4 \times 10^{19}/\mathrm{m}^3$ und Ionen- und Elektronentemperatur $T_i \approx T_e \approx 1.3$ keV injiziert, ohne zusätzliche Heizsysteme, und führte so zu einer Energieeinschlusszeit von $\tau_E \approx 150$ ms.
Darüber hinaus konnten die Abhängigkeit der Neutralisationseffizienz von der Hintergrundgasdichte und der kinetischen Energie pro Strahlatom qualitativ an diesem NBI-System beobachtet werden.
Desweiteren gelang es (89 ± 6) % der erzeugten Strahlleistung eines Testpulses mittels kalorimetrischer Untersuchung der Wärmelasten auf den einzelnen NBI Komponenten nachzuweisen. Mögliche Verbesserungen dieser Leistungsbilanzmessung des NBI-Systems wurden identifiziert. Die Wärmelast auf der Auskleidung des Ablenkmagneten sollte gemessen werden, um den Energie- und Teilchenfluss im Bereich des Magneten nachvollziehen und für zukünftige Anwendungen optimieren zu können. Die Genauigkeit der kalorimetrischen Messungen an den Komponenten im W7-X Plasmagefäß kann verbessert werden, indem Temperatur- und Volumenstrom-Sensoren mit höherer Messpräzision verwendet werden. Dazu sollten die Messungen möglichst auf den zu untersuchenden Bereich begrenzt werden. Zusätzlich können die Unsicherheit der injizierten Leistung und der Anteile der Leistungsbilanz des gesamten NBI-Systems durch genauere Bestimmung von Beschleunigungsspannung und extrahiertem Strom verringert werden.

CONTENTS

1 INTRODUCTION 1
2 BACKGROUND 5
  2.1 Neutral Beam Injection Heating 5
    2.1.1 Creation of High Energetic Neutral Beams 5
    2.1.2 Beam Plasma Interaction 8
  2.2 Calorimetry 10
3 EXPERIMENTAL SETUP 13
  3.1 Neutral Beam Injection System at Wendelstein 7-X 13
  3.2 Water Cooling System 19
    3.2.1 The High Flow Rate Cooling Circuit With the Actively Cooled Components 19
    3.2.2 The Low Flow Rate Cooling Circuit With the Inertially Cooled Components 20
    3.2.3 The Vessel Cooling Circuit With the NBI Duct and Beam Dump Components 23
  3.3 Magnetic Shielding and Magnetic Configurations of W7-X 26
4 EVALUATION 29
  4.1 Calorimetry 29
    4.1.1 Preparation of the Measurement Data 30
    4.1.2 Energy Accountability 36
    4.1.3 Commissioning Studies 40
    4.1.4 Calorimetry in Duct and Beam Dump 47
  4.2 Influence of the Magnetic Stray Field of W7-X on the Extracted Current . 53
  4.3 Error Estimation 56
    4.3.1 Systematic Errors 58
    4.3.2 Statistic Errors 62
    4.3.3 Conclusion 65
5 CONCLUSION AND OUTLOOK 71
A APPENDIX A: COOLING WATER CIRCUIT DIAGRAMS 75
B APPENDIX B: PULSE AND CALORIMETRY DATA 79

BIBLIOGRAPHY 81

LIST OF FIGURES

Figure 2.1 A Neutral Beam Injection System 6
Figure 2.2 Neutralisation Efficiency 8
Figure 2.3 Calorimetry 11
Figure 3.1 Top View of Both Injectors with Connection to Torus 14
Figure 3.2 Plasma Cross Section in the Plane of the NI21 Beams 14
Figure 3.3 Side View of NI21 15
Figure 3.4 Heat Load Schema 16
Figure 3.5 Schematic Cut Through an RF Source 17
Figure 3.6 NBI Schema With Grouped Components 18
Figure 3.7 Cross Sections of a Panel 20
Figure 3.8 High Flow Rate Cooling Circuit and Actively Cooled Components 21
Figure 3.9 Low Flow Rate Cooling Circuit and Inertially Cooled Components 21
Figure 3.10 Cross Section of a Grid 22
Figure 3.11 Cross Section of a Part Cooled From Behind 23
Figure 3.12 Vessel Cooling Circuit With Duct and Beam Dump Components 24
Figure 3.13 Water Pipes in the Beam Dump Area 25
Figure 3.14 Magnetic Stray Field of W7-X 27
Figure 4.1 Flow Rate Measurement Disturbance and Its Correction 31
Figure 4.2 Time Delay Between Inlet and Outlet Temperature Signal 32
Figure 4.3 Temperature Signals of Actively Cooled Components 33
Figure 4.4 Temperature of the Cooling Water for the W7-X Vessel Components 34
Figure 4.5 Integration Time Limit for Inertially Cooled Injector Box Components 35
Figure 4.6 Energy Accountability of the NBI System at W7-X 39
Figure 4.7 Energy or Power Accountability of the NBI System at AUG . . . 40
Figure 4.8 Calorimetry for Various Neutral Gas Flow Rates with S7 42
Figure 4.9 Calorimetry for Various Acceleration Voltages 44
Figure 4.10 Influence of Magnet Operation for S7 45
Figure 4.11 Trajectories of D_2^+ and D_3^+ in the Injector Box 47
Figure 4.12 Comparison of Modelled and Measured Energies on the Vessel Components for 20180917.002 48
Figure 4.13 Beam Emission Spectroscopy Geometry 51
Figure 4.14 Profiles of T_e, T_i, and n_e for 20180823.037 and 20181009.016 53
Figure 4.15 Influence of the Magnetic Stray Field of W7-X 54
Figure 4.16 Influence of the Magnetic Stray Field of the W7-X Trim Coil Located Between the Two Injectors 55
Figure 4.17 Schematic of the Energy Flow of an NBI Component 57
Figure 4.18 Cool Down Time of Inertially Cooled Injector Box Components . 59
Figure a.1 P & ID of the High Flow Rate Water Cooling Circuit 75
Figure a.2 P & ID of the Low Flow Rate Water Cooling Circuit 76
Figure a.3 P & ID of the Vessel Cooling Circuit 77

LIST OF TABLES

Table 4.1 Energy Accountability 37
Table 4.2 Source Parameters and Energy Fractions for Gas Flow Rate Scan 41
Table 4.3 Source Parameters and Energy Fractions for Acceleration Voltage Scan 43
Table 4.4 Source Parameters and Energy Fractions for the Deflection Magnet Operation Test 46
Table 4.5 Calorimetry Data for S7 Into Empty Vessel 49
Table 4.6 Comparison of FIDASIM and Calorimetry Results 52
Table 4.7 Installed Sensor Types 62
Table 4.8 Noise in the Temperature Signals of the Vessel Components . . . 63
Table 4.9 Error for Inertially Cooled Components of the Injector Box Due to Non-Constant Temperature of the Inlet Cooling Water 65
Table 4.10 Individual Errors That Are Taken Into Account for the Overall Error Estimate 68
Table 4.11 Final Results With Error Estimates for Calorimetrically Measured Energies at the Individual NBI Components and the Injected Power Exemplarily for 20181009n0718 and 20181009.016 69
Table b.1 Source Parameters and Energy Fractions for BES Comparison . . 79

ACRONYMS

AUG	ASDEX Upgrade
BBNBI	Beamlet Based NBI
BES	Beam Emission Spectroscopy
FIDASIM	Fast-Ion D_α Simulation
GDGN	Ground and Deceleration Grids and Neutraliser Part 1
JET	Joint European Torus
NBI	Neutral Beam Injection
OP	Operation Phase
P & ID	Piping and Instrumentation Diagram
RF	Radio Frequency
TFTR	Tokamak Fusion Test Reactor
W7-X	Wendelstein 7-X

1

INTRODUCTION

Scientists see the increase of greenhouse gases in the atmosphere - caused mainly by the combustion of fossil fuels - as only feasible reason for global warming [1]. Therefore it is of great interest to reduce the emission of these gases and find clean methods to produce energy. Renewable energies, such as wind and solar energy, are partially subject to strong fluctuations and so far suitable energy storage methods have not been implemented. That is why they can only substitute part of the energy supply, a base load is still needed in the current electricity grid. Nuclear fusion might be able to replace both fossil fuels and nuclear fission and provide this base load.

Nuclear fusion is a reaction where two atomic nuclei merge into one heavier nucleus. The fusion of light elements, e.g. hydrogen, is exothermic, which means that energy is released in the process. Therefore, fusion of light elements is attractive for usage in a power plant. At the moment, fusion research is still in a phase of exploring physics and technical concepts which could form the basis of a fusion power plant. There is no working fusion power plant, yet. In the early 1990ies the first controlled production of megawatts of fusion power was demonstrated in the Joint European Torus (JET) and the Tokamak Fusion Test Reactor (TFTR) [2–4]. With a peak outcome of 16.1 MW in 1997, JET still holds the record of the highest amount of achieved fusion power [5]. The achieved fusion power was 62 % of the input power. Still, the realisation of a nuclear fusion power plant requires further investigation and research into materials, technologies and the physics to optimise the efficiency and achieve a positive power balance.

Here, only magnetic confinement fusion is discussed in more detail. The aim is to fuse hydrogen nuclei to helium nuclei and neutrons. Fusion of the two hydrogen isotopes deuterium (D_1^2) and tritium (T_1^3) to helium (He_2^4), also called α-particle, and a neutron (n_0^1) releases 17.6 MeV in form of kinetic energy of the two products:

$$D_1^2 + T_1^3 \quad \longrightarrow \quad He_2^4(3.5\,\mathrm{MeV}) + n_0^1(14.1\,\mathrm{MeV}). \tag{1.1}$$

The α-particles generated are confined by the magnetic field of the magnetic fusion device. They heat the plasma with their energy. In a fusion power plant, the neutrons created are planned to be used to breed tritium from lithium for future operation and their kinetic energy is planned to be transformed to heat to be used to drive turbines for power generation. This is by far the most promising fusion reaction, because the required energy of the reactants to overcome the Coulomb repulsion and fuse is with 100 keV low compared to other reactions [6]. In a Maxwellian distribution, the average energy for optimal fusion is only about 10 keV. This is a temperature of about 100 million degrees Celsius. Moreover, the reactants are available or producible almost unlimited on earth.

Thermonuclear fusion requires high temperatures, at which the fuel, deuterium and tritium, is in form of an ionised gas. This state is called plasma. In addition to the high temperatures, sufficiently large density and confinement time of the plasma are needed to make the particles fuse before they transfer their energy to the plasma. If the temperature, density and confinement time are high enough, the plasma ignites, which means that the plasma becomes completely self-sustaining. From then on no external heating is necessary, because the energy released by the fusion processes keeps the plasma at the high temperature. In other words, the released fusion power at least equals the power losses.

The fusion product is the triple product of electron density n_e, plasma temperature T and energy confinement time τ_E. Derived from the power balance, it describes the conditions for the plasma to ignite. For fusion of the two hydrogen isotopes deuterium and tritium, the criterion is as follows [6]:

$$n_e T \tau_E \geq 3 \times 10^{21}\,\mathrm{keV\,s/m^3}. \tag{1.2}$$

The energy confinement time is defined as the ratio of the total plasma energy content W and the rate of energy loss P_L [6]:

$$\tau_E = \frac{W}{P_L} = \frac{W}{P_H + P_\alpha}. \tag{1.3}$$

For steady state plasma operation, the rate of energy loss is required to be balanced by the external heating P_H and the energy gain from the α-particles P_α that are absorbed by the plasma. The total plasma energy content can be determined experimentally. Thus, if heating power, plasma energy and absorbed fusion power P_α are known, the energy confinement time can be determined.

The plasma is confined with a helically wound magnetic field in the centre of a toroidal hermetic vessel to have a controlled thermic flow to the surrounding. Mainly two types of fusion devices have been developed so far. There is the tokamak creating the magnetic field with a combination of planar external coils and a toroidal current in the plasma that is induced by a transformer. Continuous operation is difficult due to the latter. And there is the stellarator, where a system of specially shaped coils allows continuous operation without any transformer action. This thesis presents experiments at Wendelstein 7-X (W7-X), one of the largest stellarators worldwide. In 2018, the highest fusion product value for stellarators was achieved in W7-X [7].

Special heating systems are used to reach high plasma temperatures. One of the plasma heating methods used at W7-X is Neutral Beam Injection (NBI). NBI was used for the first time at W7-X during the experimental campaign OP1.2b in 2018. Neutral particles with kinetic energies larger than those of the plasma particles are injected into the plasma. They transfer their energy to the plasma particles via collisions, thereby heating the plasma. To create these high energetic neutrals, ions are accelerated in an electric field forming a high energetic ion beam. The next step is the neutralisation of as many ions as possible, since only neutral particles can enter the magnetically confined plasma region without deflection by the magnetic field. Since the ions still have energies of tens of kilo electron volts, they could damage components when deflected randomly. This is why those ions that were not neutralised in the finite length neutraliser are separated from the neutrals and deflected specifically to suitable components. The injector NI21 at W7-X is equipped with two inductively coupled ion sources and individual extraction grids that can accelerate positively charged hydrogen ions up to 54 keV. Thus, two neutral hydrogen beams with estimated maximum combined heating power of 3.4 MW can be generated. A second injector is planned to be operational in autumn 2020.

The work presented here deals with the performance of the NBI system at W7-X. The heating power, also called injected beam power, is of great interest due to its connection to the energy confinement time (cf. Eq. 1.3). But the injected power cannot be measured directly. The conversion of initially generated electric beam power to injected beam power can only be calculated, if the conversion losses are known. Up to now, this was roughly estimated with experimental data from a very similar NBI system at the ASDEX Upgrade (AUG) tokamak [8]. In the frame of this work, the conversion losses are measured calorimetrically. Almost all components along the beam path, from the generation of the ions at the sources to the injection into the plasma, are water cooled with individually diagnosed water cooling circuits. Analysis of the temperature of the cooling water allows insights on the power losses at every single component. In this way, the power flow within the whole NBI system is studied. The electric power must equal the sum of the injected power and all losses at the beam path components, according to the principle of conservation of energy. This analysis is called power or energy accountability. Thereby, the injected power is measured indirectly. The calorimetrically derived power injected into the plasma is compared to the injected power derived from the spectroscopic measurement of the emission from excited beam neutrals travelling through the plasma [9–11]. Moreover, the influence of individual NBI operating parameters on the injected power and the losses, that means on the performance, is analysed. Thus, these operating parameters can be optimised for future applications.

The analysed NBI pulses belong to the first pulses performed with the two sources of injector NI21. The parameters of the pulses were mainly chosen to get the sources ready for operation. No further operation of the system was possible. The number of the available pulses and thus the parameter settings is therefore limited. In addition to calorimetry, the influence of the magnetic stray field of W7-X on the NBI source performance is investigated. The W7-X plasma is confined magnetically and different magnetic configurations are tested. The ions in the sources are influenced by electric and magnetic fields, because they are charged particles. Therefore, the performance of the sources could vary with the background field.

The structure of this thesis is as follows. An overview of the basic principles of NBI and calorimetry are given first. Because the NBI system was not designed for calorimetry, the measured flow rate and temperature data have to be corrected in various ways to get physically useful data. Therefore, the NBI system at W7-X and its water cooling system will be described in detail in Ch. 3. The function of the individual NBI components and their relation to physical processes will be explained first. The different cooling methods of the individual components and the cooling circuits they are connected to are described next. The correction of the measurement data is defined thereafter at the beginning of Ch. 4. In addition to calorimetry, the influence of the magnetic stray field of W7-X on the NBI source performance is investigated. Therefore, the magnetic shielding is described in Sec. 3.3. The main part of this work are the calorimetry results on the injected power and the operational parameters, which are presented in Ch. 4. The dependence of the extracted current on the ambient magnetic field of W7-X is analysed there, as well. Finally, the results are summarised and ideas for future progress and optimisation of the NBI system at W7-X are discussed in Ch. 5.

2

BACKGROUND

Neutral Beam Injection (NBI) is a well established method to fuel and heat plasmas in nuclear fusion devices. The performance of such a heating system can be analysed using calorimetry. This chapter is about theoretical foundations of NBI and calorimetry.

2.1 NEUTRAL BEAM INJECTION HEATING

NBI heating means feeding high energetic hydrogen neutrals into a plasma where they fuel and heat the plasma by transferring their energy via collisions. Therefore, the aim of an NBI system is to create as many neutral particles as possible, which transport as much energy as possible in order to heat and fuel the plasma efficiently. The power density injected into the plasma vessel should be as high as possible. For strong absorption of the beam in the plasma core a long interaction area in the plasma core is necessary. Therefore, the beam is injected preferably tangentially into the plasma.

This section will explain NBI heating in two parts. Firstly, the creation of the high energetic neutral beam is described. Secondly, a description of the beam plasma interaction is given. This section is based on a review paper of E. Speth [12] and chapters 5.3-5.5 of the textbook by J. Wesson [6].

2.1.1 *Creation of High Energetic Neutral Beams*

The creation of a high energetic neutral beam consists of four main steps: creation, acceleration and neutralisation of ions and in the end separation of the remaining ions from the neutrals. The reason for the neutralisation and separation processes is that charged particles can be accelerated but their trajectories are affected by Lorentz' force in a magnetic field. Since the plasma is confined by a magnetic field, charged particles from the outside are deflected and thereby slow charged particles are prevented from reaching the core. For charged particles that are so fast that they can reach the plasma core despite the Lorentz force, the interaction and thus the absorption by the plasma is lower. Therefore, the beam is created with charged particles which are neutralised before they are injected into the plasma vessel. The technical realisation of these steps leads to a large neutral beam system, which is explained in the following and depicted in Fig. 2.1.

Ion Creation

Atomic and molecular ions are created in an ion source. Hydrogen H_2, deuterium D_2 or tritium T_2 gas is used in NBI systems to create the following ion species: X^+, X_2^+, and X_3^+, with X being one of the isotopes H, D or T. The distribution of these species is called species mix or particle fractions. The general idea of an ion source is to supply energy to a neutral gas, so that a low-temperature plasma is generated. Since the energy can be supplied in various ways there are many different types of ion sources. An overview is

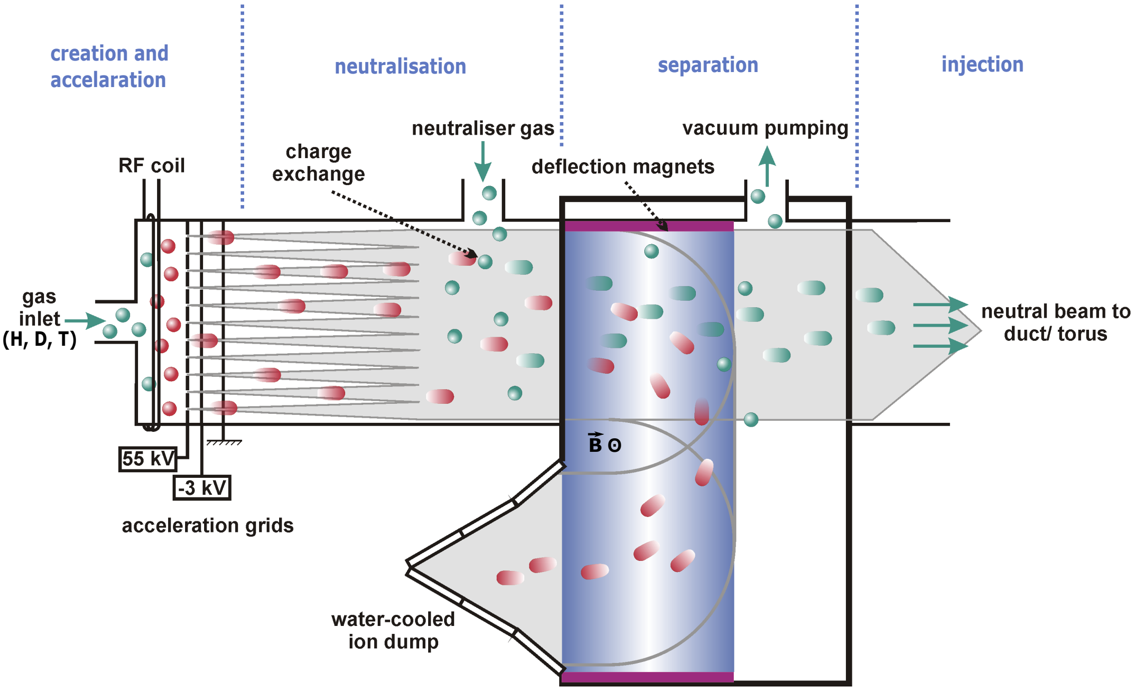

Figure 2.1: Diagram of neutral beam creation with one source (Schematic adapted from [13]). Slow particles are represented by circular dots, fast particles by elliptic dots. Neutral particles have green colour, ions have red colour. The beam creation and direction is from left to right in the diagram: Neutral gas particles are ionised in the source, here a Radio Frequency (RF) source is shown. The ions are accelerated by the electric field between the source walls and the voltage biased grid. Neutral gas is injected into the neutraliser to initiate charge exchange collisions of the fast-ions with neutrals. The deflection magnet deflects the remaining ions onto a water cooled ion dump and thereby separates them from the neutrals. At the end slow neutrals are pumped out of the neutral beam in order to inject only fast neutrals into the plasma for heating.

given in [14]. One type of inductively coupled radio frequency RF source of positive ions is shown schematically in Fig. 2.1 and explained in detail in Ch. 3.1, where the NBI setup at W7-X is described. The charge of the ions is an important characteristic. Hydrogen anions are more difficult to create than cations but are more easily neutralised especially at high energies (cf. *Neutralisation*). Neutral Beam Injection systems that work with anions are referred to as negative NBI and those with cations as positive NBI. The actual creation of the ions occurs generally by electron-impact ionisation or photoionisation of the feed gas. In the following, the focus is on positive NBI with hydrogen, since such a system was used for the experiments analysed in this thesis.

Ion Acceleration

All created ion species are accelerated out of the source by an electric field, which is implemented by a grid system. The acceleration voltage U and the charge q determine the energy $E_0 = qU$ of the beam particles. The electric energy E_0 is transformed to kinetic energy $E_{kin} = \frac{m_i}{2} v_i^2$ with the mass m_i and the the velocity v_i of the particles of the species mix, respectively. i is the index over the species. The extracted current of the total beam is defined as $I_{ext} = \sum_{i=1}^{3} q N_i v_i$ with the number of extracted ions N_i. The beam has the electric power of $P_{el} = UI_{ext}$. The duration of the beam operation is called beam time t_{NBI}. The total energy of the extracted ion beam, referred to as *electric beam energy* E_{el}, can be calculated with the beam time t_{NBI}:

$$E_{el} = UI_{ext}t_{NBI}. \tag{2.1}$$

All ion species are accelerated with the same voltage, so they have the same kinetic energy. But when a molecule dissociates, the energy is split up according to the mass ratio. For example:

$$\begin{array}{ccccc} H_2^+(E_0) & \longrightarrow & H^+(1/2E_0) & + & H(1/2E_0) \\ H_3^+(E_0) & \longrightarrow & H_2^+(1/3E_0) & + & H(2/3E_0) \end{array}$$

The generated beam is made up of many beamlets by the grid system. Thereby the divergence of the beam is much lower compared to a beam accelerated with a single aperture. The divergence describes the angular particle beam spread behind the apertures.

Neutralisation

Neutral gas is injected into the beam area close to the extraction from the source to initiate the neutralisation processes, as depicted in Fig. 2.1. Since the molecules can dissociate, also species with half, one or two third of the original energy are created. Therefore, a great variety of processes is possible, their probability is described by cross sections. Some of these processes also produce negative hydrogen. Here, this will not be discussed further. The processes and their cross sections can be found in [15] and [16]. The neutralisation efficiency η is defined as the ratio of the power of the neutrals to the power of all extracted ions, thus is a quality characteristic of an NBI system:

$$\eta = \frac{\text{power in neutral beam}}{\text{power in initial ion beam}}. \tag{2.2}$$

η depends on the cross sections of all possible processes. Thus, it depends on the target thickness, see Fig. 2.2a, and can be adjusted to a certain degree by the neutral gas density n and the length of the neutraliser L. The target thickness π is defined as

$$\pi = \int_0^L n dl \tag{2.3}$$

with the length coordinate l along the beam direction [17]. Furthermore, the neutralisation efficiency depends on the energy of the particles per atomic mass. As can be seen in Fig. 2.2b, the neutralisation efficiency is always below 100%. For positively charged particles it decreases with increasing energy per atom. For a positively charged atomic hydrogen ion H^+ with $E = 50\,\text{keV}$ the neutralisation efficiency is 55 % maximum, shown in red. The neutralisation efficiency is higher for a molecular ion H_2^+ with the same energy, because it has less energy per nucleus, shown in blue. But when dissociated those neutrals have also less energy to heat a plasma.

Separation

Only neutral particles can enter the magnetic confinement region without being deflected. The remaining charged particles still have a total energy in the order of the neutrals.

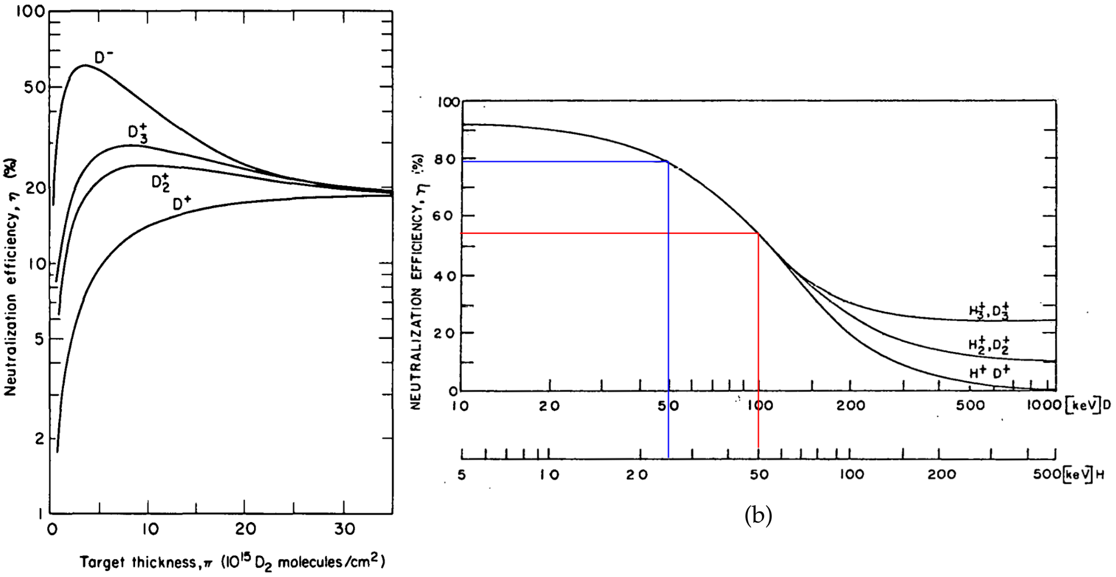

(a) (b)

Figure 2.2: Neutralisation efficiency η over (a) target thickness π (Figure from [16]) and (b) energy per atomic mass unit (Figure adapted from [18]).

Therefore, they need to be deflected by a specially designed magnetic field to cooled components called ion dumps. The neutral beam is not affected. Additional pumping is required to remove slow particles, that would otherwise cool the plasma to be heated.

2.1.2 *Beam Plasma Interaction*

This section briefly describes the main interaction processes of neutral beam particles in the plasma. For more detailed information the reader is referred to [6, 12] and for motivation of the formulas 2.5 - 2.8 to [19].

A certain number of neutral particles is injected, which have kinetic energy and momentum. If the neutrals get ionised, they become fast-ions H_f^+ and are from then on confined with the rest of the plasma by the magnetic field. Then they can transfer their energy to the other plasma particles via collisions and thereby heat the plasma, provided their energy is larger than the average energy of the plasma particles. Thereby, the temperature of the plasma ions T_i and electrons T_e increases. The energy of the plasma W, the external heating power P_H, e.g. absorbed NBI power, and in case of fusion also the absorbed power of the α-particles P_α allow the indirect measurement of the energy confinement time τ_E. The formula for steady state plasma operation is as follows:

$$\tau_E = \frac{W}{P_H + P_\alpha}. \tag{2.4}$$

The main processes leading to ionisation of the neutral beam hydrogen atoms H_b are

$$\begin{array}{llll} H_b + e^- & \longrightarrow & H_f^+ + 2e^- & \text{collisional ionisation by electrons,} \\ H_b + H^+ & \longrightarrow & H_f^+ + H^+ + e^- & \text{collisional ionisation by ions,} \\ H_b + H^+ & \longrightarrow & H_f^+ + H & \text{charge exchange by ions.} \end{array}$$

Fast-ions at the so-called critical energy E_c equally heat the ions and electrons during their slowing down. The higher their energy, the more of it is transferred to plasma electrons and the lower their energy, the more of it is transferred to plasma ions. The critical energy is defined as

$$E_c = 14.8\, T_e \left(\frac{A_f^{3/2}}{n_e} \sum_i \frac{n_i\, Z_i^2}{A_i} \right)^{2/3} . \tag{2.5}$$

E_c depends on the plasma electron temperature T_e and density n_e, the plasma ion charge Z_i, density n_i and mass number A_i and the mass number of the fast-ion A_f. For a pure hydrogen plasma and hydrogen beam E_c simplifies to

$$E_c(H) = 14.8\, T_e \left(\frac{n_i}{n_e} \right)^{2/3} . \tag{2.6}$$

The slowing down time of the fast-ions t_f is the time interval from creation to thermalisation. t_f depends on the slowing down time of the heated electrons t_e:

$$t_f = \frac{1}{3} t_e \ln \left(1 + \left(\frac{E_b}{E_c} \right)^{3/2} \right) , \tag{2.7}$$

$$t_e = 6.27 \times 10^8 \frac{A_f\, T_e^{3/2}}{Z_f^2\, n_e\, \ln \Lambda} \qquad (\mathrm{eV\, s\, /cm^3}). \tag{2.8}$$

E_b is the beam energy, Z_f is the charge of the fast-ion and $ln\Lambda$ is the Coulomb logarithm. If a fast-ion is not well confined or undergoes a charge exchange collision with a background neutral atom and thus is not confined any longer, it leaves the plasma and hits a wall component. These are called orbit- and charge exchange losses.

Moreover, the injected neutrals can become excited by the plasma particles and produce radiation in the de-excitation process. Of special interest with regard to NBI is the Balmer-alpha emission of the injected beam neutrals, measured with Beam Emission Spectroscopy (BES):

$$\begin{array}{lllll} H_b + e^- & \longrightarrow & H_b^* + e^- & \longrightarrow & H_b + \gamma + e^- \quad \text{electron excitation,} \\ H_b + H^+ & \longrightarrow & H_b^* + H^+ & \longrightarrow & H_b + \gamma + H^+ \quad \text{ion excitation.} \end{array}$$

The intensity of beam emission spectra is proportional to the neutral density and the probability of Balmer-alpha radiation transitions. The emission is Doppler shifted according to the velocities of the neutral particles in relation to the viewing geometry. Therefore, it depends on the energy of the neutrals. But the analysis of the emitted light of the beam neutrals is complicated. The measured spectrum shows the emission of the three energy components of the neutral beam with Stark splitting and other radiation, e.g. impurity lines [11]. Moreover, the beam emission spectrum can also be used to determine the local magnetic field because of the Stark effect [20].

2.2 CALORIMETRY

Calorimetry is the indirect measurement of the energy transferred from or to an object via its temperature change. The energy E, also called heat ΔQ, required to increase the temperature of a substance with mass m and specific heat capacity c by $\Delta T = T_1 - T_0$ is [21]:

$$E = \Delta Q = cm\Delta T. \tag{2.9}$$

In the case of an object, which is cooled with flowing water, the energy is transferred through the component to the water. This situation is shown in Fig. 2.3. Energy (pink arrows) is transferred to a water cooled component (grey rectangle), which is mounted with a support frame (grey columns). The thermal energy of the component is partially radiated (purple arrows), partially conducted to the support frame (yellow arrows) and mainly conducted to the water (orange arrows). Therefore, the temperature of the outlet (orange) is higher than that of the inlet (blue). The flow rate $\dot{V}$ and the rise in temperature ΔT of the water are measured with sensors in the water. Equation 2.9 is reformulated to calculate the energy transferred to the water: The mass is rewritten with the density ρ and the volume V of water as $m = \rho V$. Without thermal equilibrium an integration over time is necessary. This leads to

$$E = c\rho \int_{t_0}^{t_1} \dot{V}\Delta T dt \tag{2.10}$$

with $t_0 = -\infty$ and $t_1 = \infty$ for closed systems. Measuring the temperature of the water up- and downstream of the contact area to the component allows to calculate the energy transferred to the water for a given volume flow rate $\dot{V}$, hereinafter flow rate.

Losses in form of energy transfer to the surroundings, e.g. to the support frames, and thermal radiation have to be considered in the case of a non-isolated system or finite measuring time. The energy loss per unit time due to thermal radiation can be calculated with the Stefan-Boltzmann Law

$$\frac{\partial E}{\partial t} = \varepsilon A \sigma (T^4 - T_0^4), \tag{2.11}$$

where σ is the Stefan-Boltzmann constant, ε is the emissivity, A is the surface, T is the temperature of the component and T_0 is the temperature of the surrounding. Thermal radiation is represented by purple arrows in Fig. 2.3.

The heat flux $\dot{q}$ through the support frame is defined as

$$\dot{q} = -\lambda \frac{\partial T}{\partial x} \tag{2.12}$$

with the heat conduction λ of the material and the difference in temperature ∂T per distance ∂x [22, p. 18]. For a given contact area A, the energy loss per unit time due to heat conduction is

$$\frac{\partial E}{\partial t} = -\lambda \frac{\partial T}{\partial x} A. \tag{2.13}$$

In Fig. 2.3 heat conduction to the support frame and the water is represented by yellow arrows.

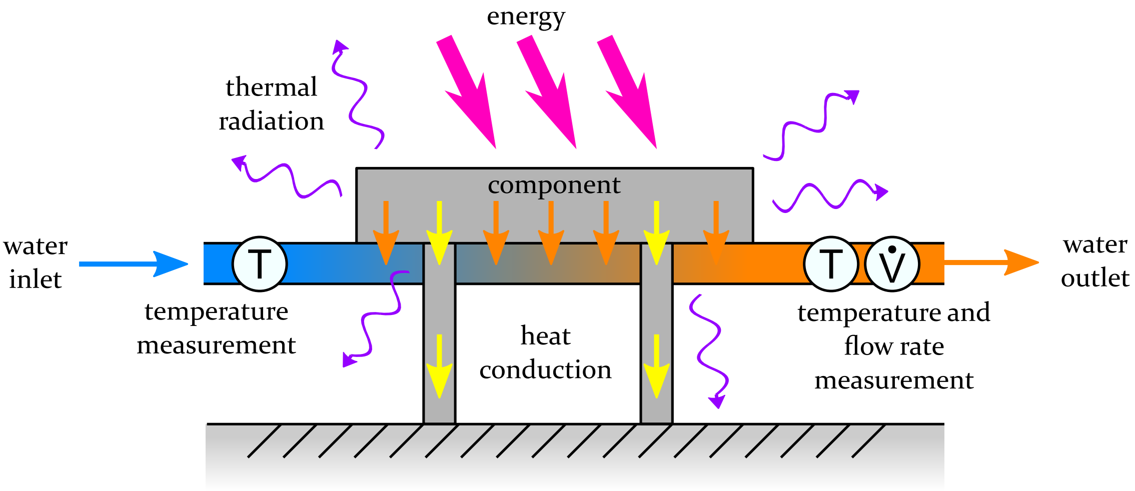
energy
thermal radiation
component
water inlet
T
temperature measurement
heat conduction
T
$\dot{V}$
temperature and flow rate measurement
water outlet

Figure 2.3: Pink arrows represent the energy flow to a water cooled component, shown as grey rectangle connected to a pipe. The thermal energy of the component is partially radiated (purple arrows), partially conducted to the support frame (yellow arrows) and mainly conducted to the water (orange arrows). Therefore, the temperature of the outlet (orange) is higher than that of the inlet (blue). The rise in temperature ΔT and the flow rate $\dot{V}$ of the water are measured with sensors in the water.

3

EXPERIMENTAL SETUP

Calorimetry is the main method used in this thesis for determining the energy deposited on the cooling elements. However, the NBI system was not designed for calorimetry. For this reason, the measured flow rate and temperature data have to be corrected in various ways to get physically useful data. Therefore, the NBI system at W7-X and its water cooling system will be described in detail in this chapter. The function of the individual components and their relation to physical processes will be explained first. The different cooling methods of the individual components and the cooling circuits they are connected to are described next. The correction of the measurement data is defined later (Ch. 4). In addition to calorimetry, the influence of the magnetic stray field of W7-X on the NBI source performance is investigated in this thesis. Therefore, the magnetic shielding is described in Sec. 3.3.

3.1 NEUTRAL BEAM INJECTION SYSTEM AT WENDELSTEIN 7-X

Two NBI injector boxes, NI20 and NI21, for hydrogen or deuterium injection, each with four positions for ion sources, are installed at the W7-X stellarator. The sources are numbered from one to eight and are therefore referred to as S1 to S8. NI21 was commissioned with S7 and S8 in operation phase OP1.2b in 2018. These two sources can generate two neutral hydrogen beams with an electric power of up to 5.0 MW, each. The estimated maximum combined heating power is 3.4 MW. S5 and S6 are not installed, yet. This thesis deals with the characterisation of this first injector box using experimental data from that operation phase. The second injector box, NI20, is planned to be operational in autumn 2020, also with two sources initially installed. Upgrade to four sources per injector box is still being considered.

This section describes the position of the injectors in relation to the torus. An overview of injector NI21 is given next. This is followed by a description of NBI operation. Detailed information on single components of injector NI21 is given at the end.

The two injectors are shown with one fifth of the fivefold quasi-symmetric W7-X plasma vessel in the top view in Fig. 3.1. Both injectors are connected to the plasma vessel with a gate valve (light blue) and duct. The positions are optimised for highest transmission through the duct and highest beam absorption by the plasma [23, 24]. The geometry and size of the ducts is limited, due to the limited space between the superconducting coils of W7-X. Therefore, the beams of the four sources of one injector are directed to meet inside the small duct. In addition, the injection angles are rather radial to the magnetic axis and the plasma core of W7-X than tangential [24, 25], as can be seen from the beam centre lines in magenta.

The cross section of the beams and the plasma flux surfaces is shown in Fig. 3.2. The sources mounted at the upper back side of the injector box, here S7 and S8 of NI21, are directed downwards. Thus, the beams pass through the centre of the plasma. The bottom two sources, here S5 and S6 of NI21, are directed upwards. Their beams miss the plasma core but the total path length through the plasma is longer than for S7 and S8.

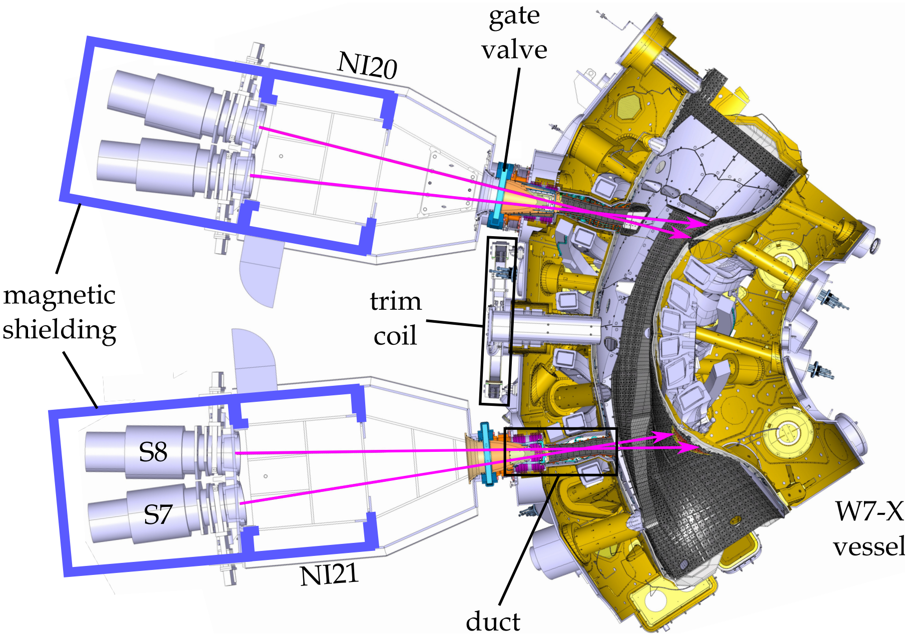

Figure 3.1: Top view of the neutral beam injectors NI20 and NI21 connected to the W7-X plasma vessel (Figure adapted from [23]). The beam centre lines are shown in magenta. They intersect in the duct. S7 injects almost radial, whereas S8 injects more tangential. The beam plasma cross sections are shown in Fig. 3.2 in side view. The gate valves (light blue) can separate the injectors from the plasma vessel for commissioning pulses onto the calorimeter. The magnetic shielding is shown schematically in blue. The sources and first part of the neutralisers are inside of an iron box. Additional iron plates are installed inside of the injector box. They shield the region of the second part of the neutralisers, the ion dumps and the deflection magnet from the stray field of W7-X. One of the five trim coils is positioned between the two injectors at the outside of the W7-X plasma vessel. The magnetic shielding of the injectors from the stray field of W7-X is described in Sec. 3.3.

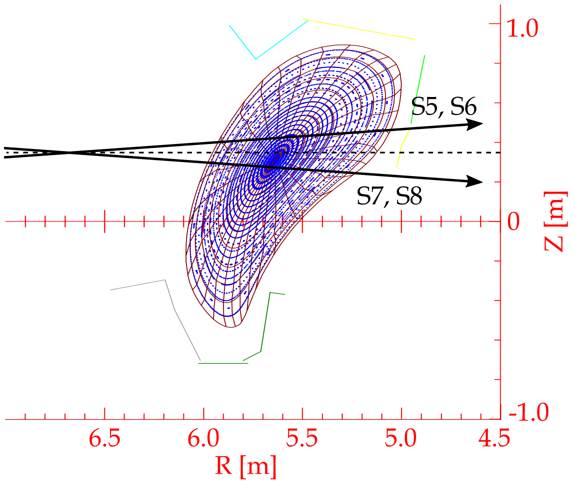

Figure 3.2: Plasma cross section in the plane of the NI21 beams (Figure adapted from [24]). S7 and S8 are mounted at the top back side of NI21. Their beams cross the plasma centre. S5 and S6 can be mounted at the bottom back side of the same injector. Their beams would then enter the plasma above S7 and S8.

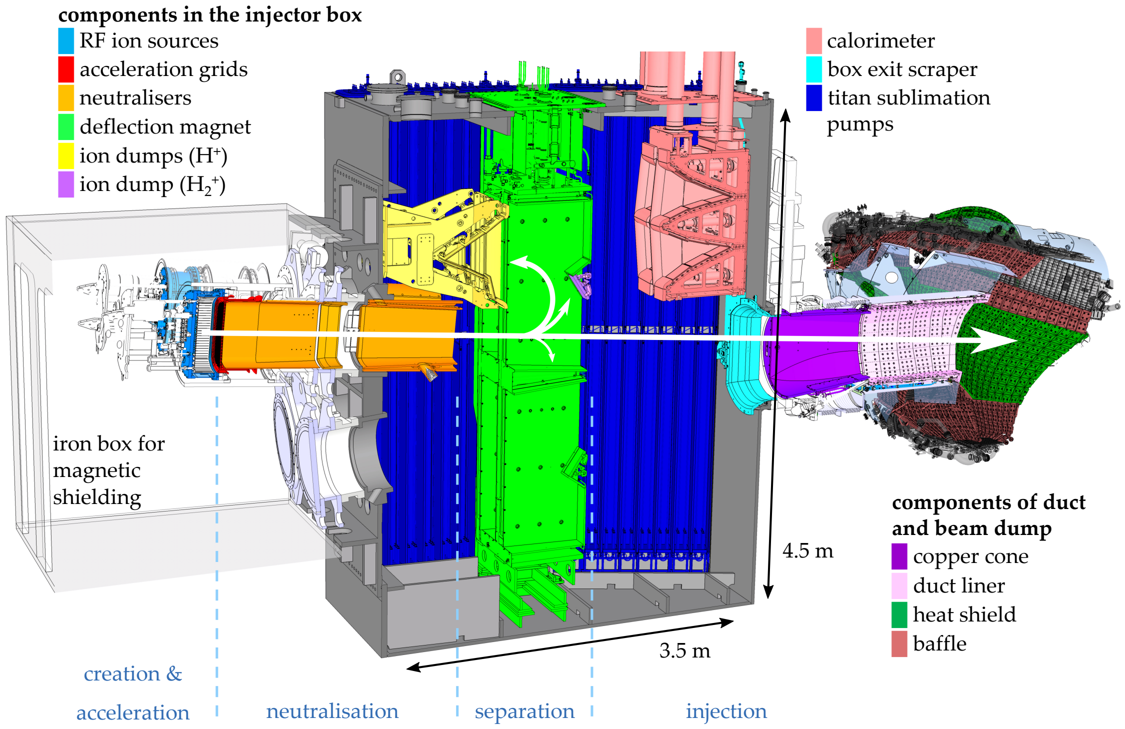
components in the injector box
RF ion sources
acceleration grids
neutralisers
deflection magnet
ion dumps (H+)
ion dump (H2+)
calorimeter
box exit scraper
titan sublimation pumps
iron box for magnetic shielding
components of duct and beam dump
copper cone
duct liner
heat shield
baffle
4.5 m
3.5 m
creation & acceleration
neutralisation
separation
injection

Figure 3.3: Side view of NI21. The components are listed with coloured markers that match the colour of the component. The direction of the neutral and ion beams is marked with white arrows. The beam plasma cross sections are shown in Fig. 3.2. The injector box is coloured in dark grey. The iron box to shield the sources of the magnetic stray field of W7-X is shown in light grey.

The NBI system at W7-X is an upgraded version of the one in operation at AUG [8]. Figure 3.3 shows the inside of injector NI21 and the connected vessel area from the side. The injector is equipped with two RF driven positive ion sources (left side, blue) that can generate positively charged hydrogen or deuterium. The hydrogen or deuterium ions are accelerated by the grid system (red) up to 54 keV or 60 keV, respectively, thereby forming a beam. The direction of the ion and neutral beams are represented by the white arrows. The extracted ion beam is directed through the neutralisers (orange), which are filled with the same neutral gas as the sources. The ions can become fast neutrals through charge exchange collisions with the background neutrals. The fast neutrals and ions are then separated in the magnetic field of the deflection magnet (light green), which is positioned in the centre of a vacuum box (dark grey). The injector box is cleared from neutral gas streaming out of the neutralisers by titanium sublimation pumps (dark blue). In the magnetic field of the deflection magnet, the remaining H^+ ions are deflected to the H^+ dumps (yellow), the remaining H_2^+ ions to the H_2^+ dumps (purple) and the H^- ions to the bottom magnet liner. The neutral beam ends in the calorimeter (pink), if the calorimeter is lowered (not shown in the figure). For plasma heating operation, the gate valve is opened and the calorimeter is raised as is the case in the drawing. Then the beam is directed through the duct into the plasma vessel. The beam particles that are not absorbed by the plasma hit the beam dump, which consists of heat shield (dark green) and baffle (brown) tiles.

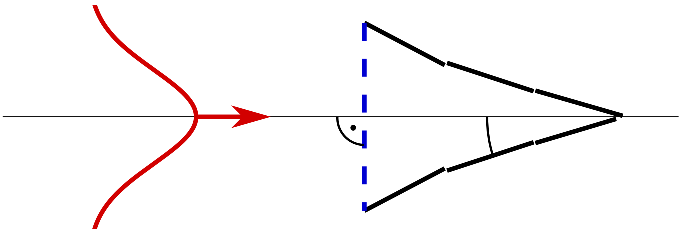

Figure 3.4: Schema of the beam hitting the calorimeter or H^+ dump. If the beam (red) were to hit a component directly (blue), the component would melt due to the high thermal load. Therefore, the target area of the calorimeter and the H^+ dump are shaped like a '>' so that the beam strikes the components in an angle between 0° and 54° to the beam axis (horizontal). This way, the effective target area is larger and the heat loads caused are reduced to a maximum power density of $25\,\mathrm{MW/m^2}$ that the components can withstand.

The fast beam particles that strike a component cause heat loads with power densities of up to $25\,\mathrm{MW/m^2}$, even though the components are oriented between 0° and 54° to the beam axis. This is shown schematically in Fig. 3.4. To prevent the components from melting and other damage due to the heat loads, almost all components along the beam path are cooled with water. The cooling of the components is described in the next section. Additionally, the injector is working in pulsed mode, so the components have time to cool down in between pulses. The time in between pulses is at least three minutes. Complete cool down of the components takes up to eleven minutes depending on the total power of the previous pulse. Moreover, the titanium sublimation pumps are prepared for the next pulse to preserve the vacuum. One pulse is several seconds long or consists of a series of short blips. The time interval, when a neutral beam is generated, is called beam time t_{NBI}. At full power the maximum beam time is five seconds. A pulse into the plasma vessel is called *in-vessel pulse* and has the pulse ID of the W7-X experiment: YYYYMMDD.EN. A pulse onto the calorimeter is called *commissioning pulse* and is given a pulse ID in this form: YYYYMMDDnhhmm. In both cases 'Y' is for year, 'M' for month and 'D' for the day. The W7-X plasma experiments have IDs already. They start with the date and end with a dot and the W7-X experiment number. The pulse IDs of commissioning pulses also start with the date and end with an 'n' for NBI and the start time of the beam in UTC.

The RF ion sources are identical to those of the newer injector at AUG [26–28]. They create ions via inductive coupling. Fig. 3.5 shows a schematic view of an RF source. One RF ion source mainly consists of a quartz vessel wrapped in an RF coil inside of a vacuum vessel and with a plasma grid at the front. A gas, here hydrogen, is injected into the inner vessel. The starter filament provides free electrons for the plasma build-up in the first 200 ms of every pulse. When operated, the RF coil induces a current that accelerates the electrons now present in the gas. The accelerated electrons collide with the neutral gas particles and ionise them, thereby releasing more electrons that ionise more neutrals. The quartz vessel separates the plasma from the coil, to prevent arcs and electrical breakdowns. Moreover, a Faraday screen protects the quartz vessel from the plasma to prevent sputtering of silicon, which subsequently is deposited on the source-plasma facing side of the plasma grid. The Faraday screen has small slits to allow the induction field to enter the inner vessel, while blocking direct capacitive coupling. The backplate of the source is equipped with magnets in chequerboard pattern to prevent the charged

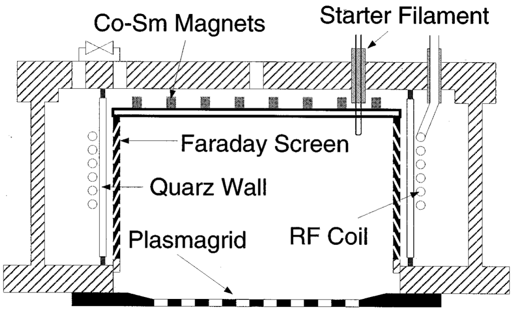

Figure 3.5: Schematic cut through an RF source (Figure from [26]). The RF coil induces an alternating magnetic field in the centre of the source, which is filled with hydrogen gas. The heated filament provides free electrons which are affected by the field and collide with the hydrogen gas particles, which generates more electrons and ions. This way a plasma is created. The quartz wall separates the plasma from the coil. To prevent sputtering of the quartz wall, a Faraday screen is implemented. The Faraday screen is slotted so that current is only induced in the plasma. Permanent Co-Sm Magnets in a chequerboard pattern cover the backplate of the source to prevent the charged particles from hitting the backplate and thereby leave the plasma.

particles from hitting the backplate and thereby leave the plasma. The sides of the source cannot be optimised like that, due to the inductive coupling of the RF field produced by the coils.

To extract the ions, the Faraday screen and the plasma grid are charged with the acceleration voltage U, here up to 54 kV. Plane-parallel to the plasma grid is a deceleration grid, which is biased to about -2 kV, and a ground grid that, as the name suggests, is grounded. This setup shields the plasma grid from the electrons of the neutraliser and works as a lens to minimise the beam divergence. The distances between the grids are optimised for the lowest divergence of a 54 keV hydrogen beam. The charged particles at the holes in the plasma grid see the electric field created by the plasma grid and the deceleration grid. For every ion that leaves the source and thus, leaves the plasma, an electron leaves the plasma, too, due to the requirement to maintain the macroscopic neutrality of the plasma. The ions are accelerated at the holes in the plasma grid in the direction of the deceleration grid, while the electrons are repelled by the electric field but randomly hit the walls of the source. This way, the extracted current of ions I_{ext} is indirectly measured as current of electrons from the ion source. When an accelerated ion strikes the deceleration grid, it heats the deceleration grid and electrons are released. These electrons are accelerated onto the plasma grid or into the source, where they heat the material they hit, or they collide with the ions, neutrals or electrons in their way. Collisions in the source only create more ions and electrons in the source, but collisions in the grid region can lead to further interactions with again further subsequent processes, which more or less all lead to heat loads on the components. The exact dynamics are still under discussion.

Every grid system is connected to a two part neutraliser. The neutraliser is mounted at the rear of the injector box. The first part protrudes backwards out of the injector box, the second part protrudes inwards. The ground grid, deceleration grid and the first part of the neutraliser are considered as a group because of the collective temperature and flow rate measurement in the cooling water for these components (cf. Sec. 3.2) and are abbreviated with GDGN. The neutralisers, the magnet liners and the duct components

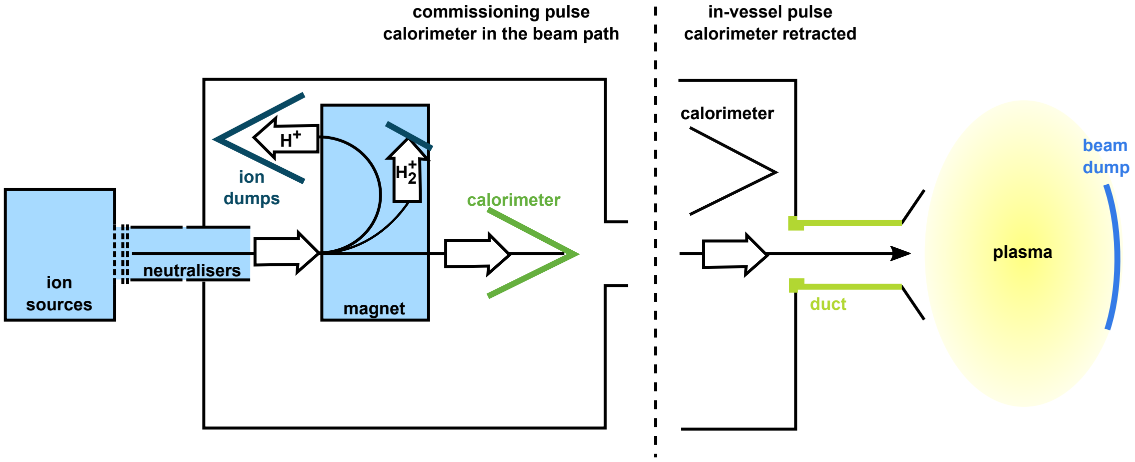

Figure 3.6: NBI Schema with Grouped Components (Figure adapted from [29]). The left part shows the injector with the calorimeter (green) in the beam path for commissioning pulses. The right part shows the calorimeter in the retracted position as is the case for in-vessel pulses. The combined heat load on the sources, the grids, both parts of the neutralisers and the magnet liners is called *box losses* (left side, light blue). The ions that were not neutralised in the neutraliser are deflected onto the ion dumps (dark blue). The neutrals are unaffected by the magnetic field of the deflection magnet and are directed to the calorimeter (commissioning pulses) or through the duct into the plasma (in-vessel pulses). The heat load on the calorimeter in the case of a commissioning pulse gives a first estimate of the injected power for a comparable in-vessel pulse. The heat loads on the duct components, namely the box exit scraper, the copper cone, and the duct liner, in case of an in-vessel pulse are referred to as *duct losses* (right side, light green). The heat loads on the heat shield and baffle in the beam dump at the plasma vessel are due to injected beam particles, that were not absorbed by the plasma.

scrape the beams. Therefore, the heat loads on these components increase with the beam divergence. Additionally, reionisation of neutrals in the stray field of W7-X in the duct and in the field of the deflection magnet can result in trajectories that end on the duct components and the magnet liners, respectively. The same is true for neutralisation of ions in the deflection magnet. In addition, negative ions are deflected to the bottom magnet liner. Space charge expansion of the ion beam is prevented by a high neutral gas density in the magnet region [30]. The neutral gas comes from the neutralisers into the magnet region.

Beam particles, and with them power, landing on all other components than the calorimeter are considered losses. In Fig. 3.6 the NBI system and its components are shown schematically. The heat load on the sources, the grids, both parts of the neutralisers and the magnet liners combined is referred to as *box losses* (light blue, left side). The heat loads on the duct components, namely the box exit scraper, the copper cone, and the duct liner, are called *duct losses* (light green). The heat load on the calorimeter (commissioning pulse, green) gives a first estimate of the injected power for a comparable in-vessel pulse. Moreover, the neutralisation efficiency can be calculated from the heat load on the calorimeter. The heat loads on the heat shield or baffle in the beam dump (blue, right side) at the plasma vessel are due to injected beam particles, that were not absorbed by the plasma. The ratio of the energy found on the beam dump to the injected energy is the *shine through*.

3.2 WATER COOLING SYSTEM

The hydrogen beam particles accelerated to tens of keV reach heat load power densities that can melt solids nearly instantaneously. Therefore, most NBI components are cooled with water from one of three cooling water circuits depending on the expected heat load power density and practicability. The cooling is different for almost every NBI component, because they differ in material, geometry and support frame. Thus, almost every NBI component is cooled with different flow rates of the cooling water during the pulses and in between pulses. Moreover, the distance between temperature sensor and component is different for the various components. Nevertheless, the components can be divided into two groups: The components with highest expected heat load power densities of up to 25 MW/m^2 consist of parts with a complex structure, which enables rapid heat transfer to the cooling water. Therefore, dynamic equilibrium of the heat transfer through the components to the water is reached within about two seconds, thus typically already during the pulse. These components are called *actively cooled*. Slow heat transfer is sufficient for the components with expected heat load power densities of less than 3 MW/m^2. This is why they consist of parts, which are less complex to manufacture. Hence, the heat transfer is slower and typically no dynamic equilibrium is reached within a pulse. These components are called *inertially cooled*.

Every water cooled NBI component is connected to one of three cooling water circuits: All actively cooled components are supplied with water by the *high flow rate cooling circuit*. The inertially cooled components are connected to the other two cooling water circuits. Those inside of the injector are connected to the *low flow rate cooling circuit*. Each one of the three separate cooling water circles is closed. Hence, the temperature of the cooling water is generally not constant, but shows fluctuations due to previous pulses. The temperature varies by up to one degree. The pipes for the components of the not yet installed sources number 5 and 6 are installed and connected to these cooling circuits as well. But the pipes are modified so that only less than 1 % of the overall water flow passes through them. This water is neglected for the calorimetric calculations.

In this section the three cooling water circuits are described in detail and with them the components connected to the cooling structures and the installed flow rate and temperature sensors. A list of the installed types of sensors and their uncertainties can be found in Sec. 4.3. The Piping and Instrumentation Diagrams (P & ID) of the three cooling water circuits are attached in the Appendix part a.

3.2.1 *The High Flow Rate Cooling Circuit With the Actively Cooled Components*

The high flow rate cooling circuit supplies all actively cooled components, namely the H_2^+ dump and the centre parts of calorimeter and H^+ dump with water. During NBI pulses about 300 m^3/h of deionized water is cooling these components with an inlet pressure of 16 bar. After each pulse the pumps slow down so that a flow rate of 160 m^3/h with 11 bar inlet pressure is generated. About 20 s before the next pulse the pump power increases again to reach the higher flow rate during the pulse.

The expected power density is the highest at the centre parts of the calorimeter and the H^+ dump as well as the entire H_2^+ dumps. Here, in fact, the copper would melt without active cooling. These parts are made of thin hollow copper tiles, called panels, with cooling fins on the inside where the water is guided through for the most efficient

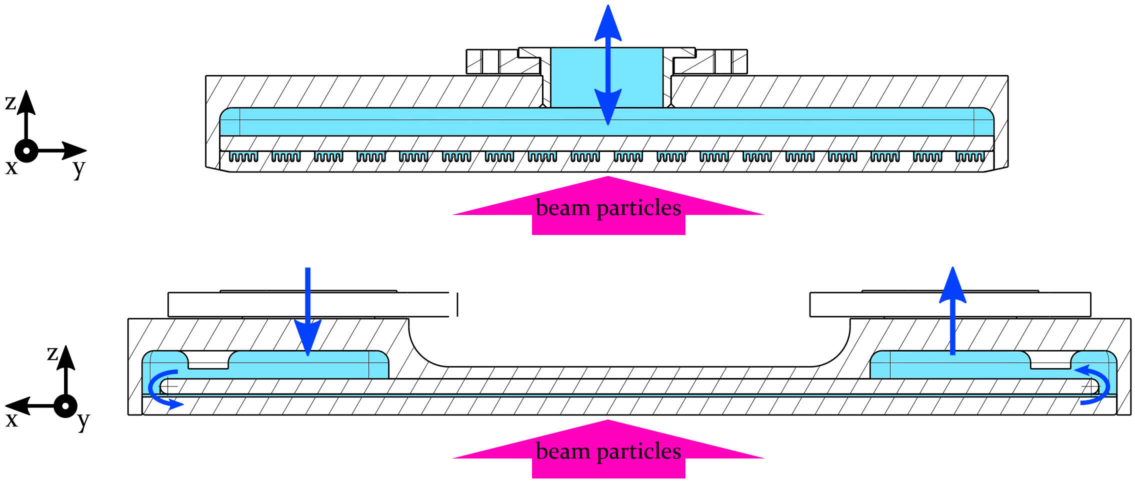

Figure 3.7: Two cross sections, one cut through the yz-plane and one cut through the xz-plane, of an actively cooled part of a component, called panel. The panel is equipped with cooling fins on the inside where the water is led through for the most efficient cooling. The hollow area filled with water is shown in light blue. The flow of the water is depicted with the blue arrows.

cooling. The copper between surface and cooling fins has a thickness of only 2.6 mm. This way these components cool down quickly. Less than five seconds after a pulse the outlet water temperature shows no difference from the inlet anymore. A cross section through a panel is shown in Fig. 3.7. The typical design of a panel is described in detail by the example of calorimeter panels in [31]. Optimisation of the design is still ongoing [32]. The centre parts of the H^+ dumps and the calorimeter are each equipped with six panels per NBI source. The H_2^+ dumps consist of one panel per source.
A diagram of the high flow rate cooling circuit with the sensors and an actively cooled component is shown in Fig. 3.8. The water is guided to all installed panels in parallel through supply lines from a water buffer tank, which is connected to a heat exchanger and is working as a hydraulic separator. There is one supply line for the calorimeter equipped with a thermocouple to measure the temperature of the inlet water. There is another supply line for the ion dumps. The one for the H_2^+ dumps in the magnet is also equipped with a thermocouple. The temperature of the inlets of the H^+ dumps is measured separately with a PT100 each. After several meters of pipes the water reaches the component and is guided through the panels with the cooling fins. Less than five centimeters behind each panel a thermocouple measures the individual outlet water temperature. At each of the two supply lines the flow rate is measured with a flowmeter. The flowmeter at the outlet of the H_2^+ dumps was not working during the measurements of this thesis.

3.2.2 *The Low Flow Rate Cooling Circuit With the Inertially Cooled Components*

The low flow rate cooling circuit supplies all other components of the injector that need cooling: the RF sources, grids, neutralisers, magnet liners, box exit scraper, titanium sublimation pumps and the outer parts of calorimeter and H^+ dumps. This water circuit is cooling with a flow rate of 45 $\mathrm{m^3/h}$ during pulses and 38 $\mathrm{m^3/h}$ in between. The inlet pressure is 10 bar. The inlet flow rate is increased during a pulse and actively reduced in

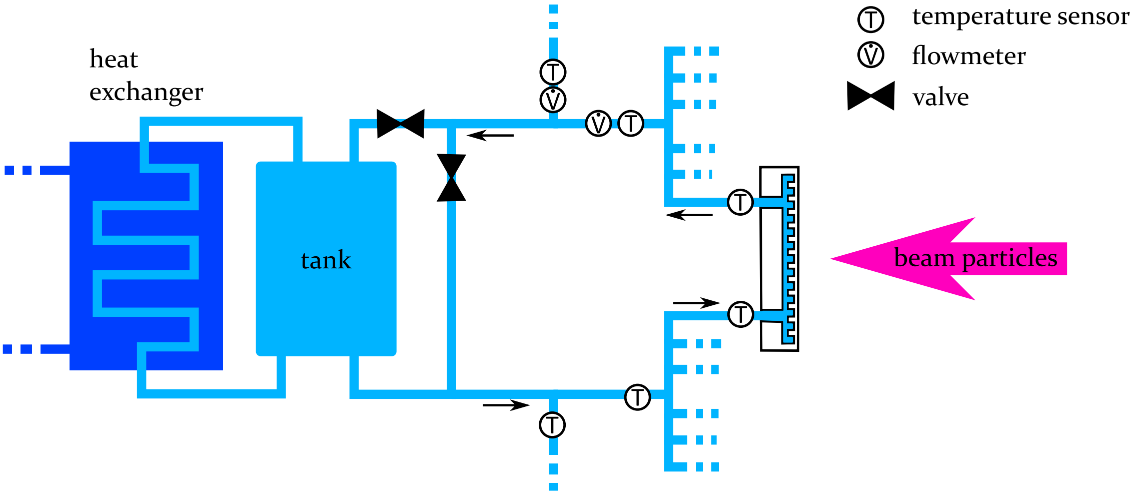

Figure 3.8: Diagram of the cooling method used for the high flow rate cooling circuit. Exemplarily, one actively cooled component is shown. The pipes to other components and parts are indicated. The cooling lines are connected via a buffer tank with temperature layering to the heat exchanger of the W7-X cooling circuit. This is shown on the left side of the diagram. The direction of flow is marked with black arrows.

between pulses to put less mechanical stress on the components, especially the plasma grid, the Ground and Deceleration Grids and Neutraliser Part 1 (GDGN) and the RF sources. All components are connected to the cooling circuit in parallel.

The components can be divided into two groups depending on the cooling structure. The acceleration grid systems and the back plates of the RF sources are cooled by water flowing through the components, but without cooling fins as the actively cooled components. They are described in the paragraph on the components which are *Cooled on the Inside*. All other components of the NBI injector have the pipes with the cooling water soldered to the back and are described under *Cooled from Behind*.

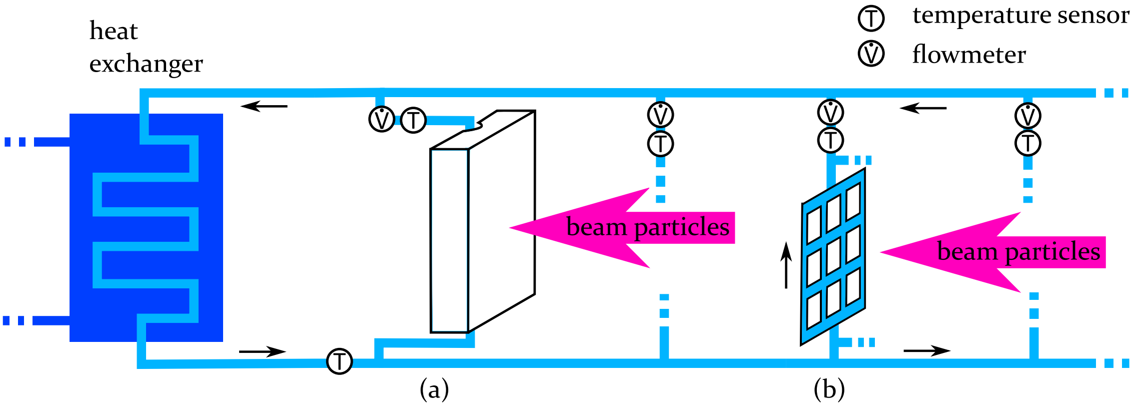

Figure 3.9: Diagram of the low flow rate cooling circuit and the used cooling methods at the supplied inertially cooled components. Exemplarily, one component cooled from behind (a) and one component cooled from the inside (b) are shown. The pipes to other components are indicated. The circuit is indirectly connected to the W7-X cooling circuit with a heat exchanger. This is shown on the left side of the diagram. The flow direction is marked with black arrows.

Cooled on the Inside

The acceleration grid systems and the backplates of the RF sources are also made of copper and cooled by water flowing through the components. At these components the heat load of a pulse is completely transferred to the cooling water within three minutes. A cross section of a part of a grid is shown in Fig. 3.10. The beam passes through the circular holes and the cooling water is led through the rectangular tunnels in between. The cross-sectional area of the water tunnels is 2.0 mm by 1.5 mm. The distance to the surface of the grid is at least 1.0 mm.

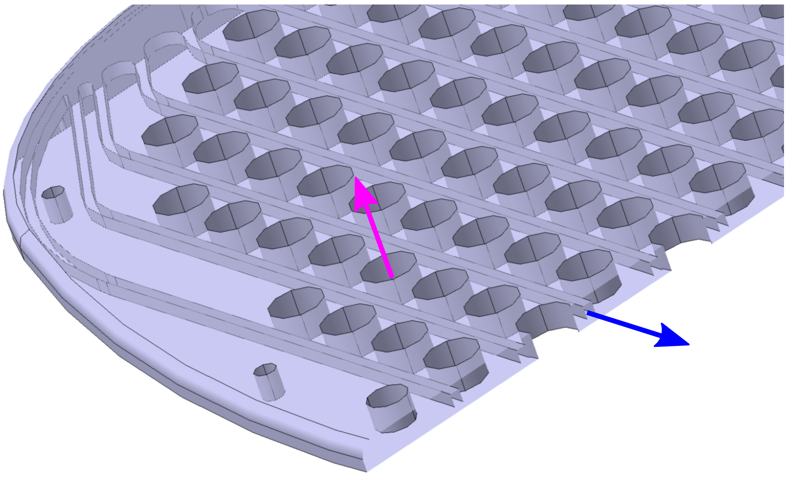

Figure 3.10: Cross section of a cut-out of a grid. The beam is directed through the holes, exemplarily shown for one hole with a pink arrow. The cooling water is led through the rectangular tunnels in between, exemplarily shown for one tunnel with a blue arrow.

This water cooling method is schematically shown in Fig. 3.9b. Thermocouples are installed several meters up- and downstream from the components. Flowmeters are installed only downstream from the components. The cooling water coming from the first parts of the neutralisers is mixed with the water coming from the ground- and deceleration grids. Also the cooling water coming from the backplate of every RF source is mixed with the water coming from the Faraday screen and the RF coil of the source. The temperature and flow rate of the water are measured in the supply pipes behind the junctions in both cases. Therefore, individual data for these components do not exist. The ground- and deceleration grids with the first parts of the neutralisers is referred to as GDGN and the backplate, the Faraday screen and the RF coil of each source are referred to as RF source in the following due to the combined measurement. The temperature sensor in the outlet of the first part of the neutraliser and the ground- and deceleration grid of S7 was not working throughout the campaign OP1.2b. The one related to S8 broke on 25.09.2018. The heat load for calculations of pulses afterwards are estimated on the basis of measurement data collected earlier. The titanium sublimation pumps have aluminium parts with stainless steel pipes for the cooling water grouted in. The temperature and flow rate of the cooling water of the titanium sublimation pumps is not measured. The first parts of the neutralisers as well as all other water cooled components inside the injector are cooled also with the water from the low flow rate cooling circuit but with the method explained in the next section.

Cooled from Behind

All other parts of components of the NBI injector, that is both parts of the neutralisers, the magnet liners, the box exit scraper, the copper cone, and the outer parts of the H^+ dumps and the calorimeter are equipped with cooling water pipes soldered to the back. Here the heat is transferred slowly compared to the methods described above. As an example, a cross section of one side part of the calorimeter is shown in Fig. 3.11.

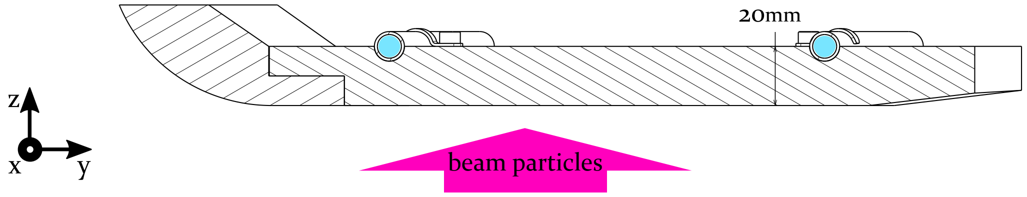

Figure 3.11: Cross section of one inertially cooled side part of the calorimeter. The cooling water shown in light blue is led through the pipes on the back of the part. Here, the heat is transferred through 1.5 cm (z direction) and up to 10 cm (y direction) of metal to the pipe and then through the nickel-based brazing solder and the 1 mm thick stainless steel pipe walls to the water.

The heat has to be transferred through the component to the water in the pipe, which means through the component, the nickel-based brazing solder and the 1 mm thick stainless steel pipe walls. The heat transfer path through the component varies from 2 mm to 20 mm in z-direction and up to several 10 cm in y-direction. The heat transfer through the various components takes place over distances from 2 to 20 mm in z-direction and up to several 10 cm in y-direction. Therefore, it takes up to ten minutes after a pulse until no significant difference between inlet and outlet water temperature is detected. Fig. 3.9a shows a diagram of the cooling method in the frame of the low flow rate water cooling circuit. The temperature of the inlet water is measured by one PT100 temperature sensor in the supply line several meters upstream of all the components. The temperature and flow rate of the outlet water is measured with thermocouples and flowmeters, respectively, in the various pipes several meters downstream each of the components. For the second parts of the neutralisers and the outer parts of the H^+ dumps the temperature is measured separately for each of the parts related to the sources. The copper cone is cooled with water from the W7-X cooling water circuit. Although the magnet liners are cooled this way as well, the temperature and flow rate of the cooling water is not measured.

3.2.3 *The Vessel Cooling Circuit With the NBI Duct and Beam Dump Components*

The duct liners, copper cone, baffle and heat shield are cooled with water from the vessel cooling circuit, that cools all W7-X vessel components in the NI21 port and beam dump area. The flow rate and inlet pressure are constant. The copper cone is the only component supplied by this cooling circuit, that is cooled from behind the same way as some inertially cooled components in the injector box described in the previous section. Inside the W7-X vessel in the NBI beam dump area and in the NBI duct the components heat shield, baffle and duct liners consist of separate tiles, cooled with water flowing through stainless steel pipes that are soldered to their backs. The tiles are made of copper chrome zirconium, short CuCrZr, and reinforced carbon fibre composite mounted on

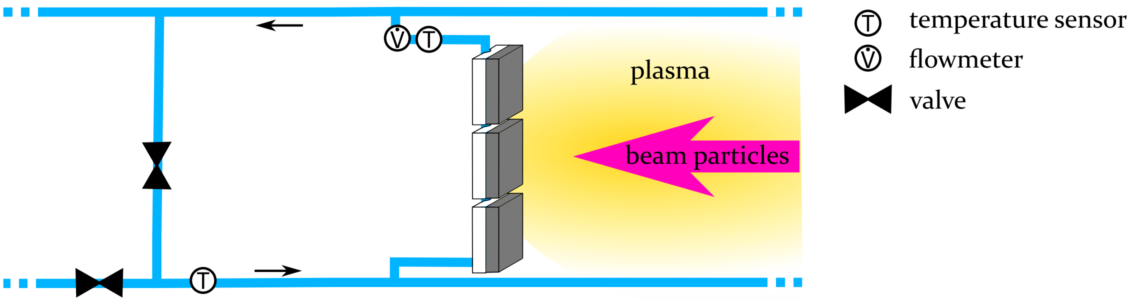

Figure 3.12: Diagram of the vessel cooling circuit. Exemplarily, three W7-X vessel tiles are shown, the pipes to other vessel sections are indicated. The cooling circuit is directly connected to the W7-X cooling circuit with valves. This is shown on the left side of the diagram. The direction of flow is marked with black arrows.

top, which is exposed to the plasma and shine through of the NBI beam. In between, there is a 1 mm layer of Sigraflex to improve the thermal contact. The construction of those tiles and the cooling method is described in detail in [33] and [34]. A diagram representing this cooling construction and the vessel cooling circuit is shown in Fig. 3.12. Flowmeters up- and downstream of every vessel component measure the flow rate and the temperature.

The heat shield and the baffle are areas of tiles in the vessel. But the area covered by the neutral beams is only a part of these areas. Therefore, the water cools NBI unrelated tiles in series or parallel as well and no pure/discrete beam dump information is available. Four sections of the heat shield are cooled in parallel but the water temperature is measured only after the cooling water is combined again. Thereby, the heat shield covers an area of about 1.5 m^2, whereas the beams cover only an area of the heat shield of approximately 0.2 m^2, that is 13 %. The baffle area that is cooled by the same circuit is about 0.3 m^2 of the vessel in total and maximum 0.1 m^2 is wetted by the beam. The pipes for the beam dump and surrounding vessel area can be seen in Fig. 3.13.

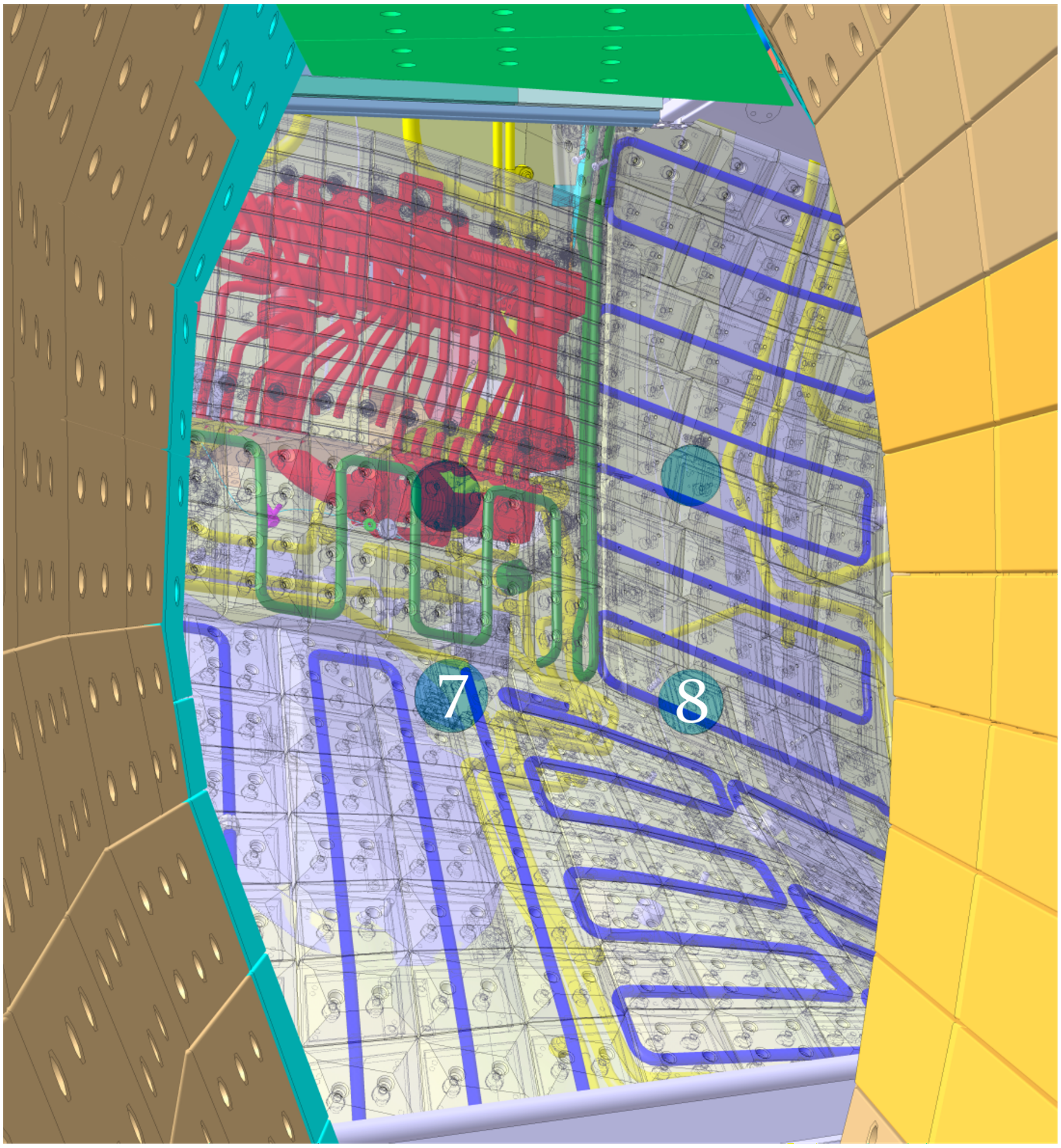

Figure 3.13: Water pipes in the beam dump and surrounding vessel area: In green the pipes of the baffle, in blue the pipes of the heat shield and in yellow the pipes of the in- and outlet. The centre of the beams is marked with turquoise circles. The centres of the beams related to S7 and S8 are marked with white numbers.

3.3 MAGNETIC SHIELDING AND MAGNETIC CONFIGURATIONS OF W7-X

The magnetic field of Wendelstein 7-X is produced by 85 coils. 70 of them are superconducting coils, fifty non planar ones and twenty planar ones, confining the plasma in a fivefold symmetric ring. Additionally, ten normally conducting coils are installed on the inside of the plasma vessel. And finally, five normal conducting trim coils are installed at the outer sides of the torus. These coils allow for correction of error fields and further control over the divertor heat loads. The currents through the different coils can be varied and result in various magnetic field configurations of W7-X. Detailed information on the magnetic configurations can be found in [35].

The magnetic field of W7-X outside of the plasma vessel is referred to as *magnetic stray field*. The expected magnetic stray field of W7-X from 2010 is shown for the high iota configuration in Fig. 3.14. The magnetic field strength in the centre of the plasma is up to 3 T. At the deflection magnets the stray field would be 10 to 20 mT without shielding. But only 2 to 3 mT are allowed for NBI operation in this region. At the RF sources the stray field strength would be in the range of 2 to 5 mT but only 0.2 to 0.3 mT are allowed. To minimise the influence of the magnetic stray field on the ions of the NBI system, there are two connected iron boxes for magnetic shielding around the NBI components [36]. On the one hand, the performance of the ion sources might vary for the different magnetic configurations. The ions in the sources are influenced by a magnetic field. If the magnetic field varies, the trajectories of the charged particles change and the sources performance might be different. On the other hand, the trajectories of the fast-ions have to end on the components that are designed for the power load and thus, need to be shielded from the influence of the magnetic stray field of W7-X. The shielding geometry was optimised for the smallest field in the injector box, but at the same time, the shielding introduces field errors of the confining magnetic field, which must not exceed critical values.

The final design of the shielding boxes was completed in 2010 for the expected magnetic stray field of W7-X. The five external trim coils were not planned at that time and were therefore not included in the shielding calculations. One trim coil is exactly in the middle between the two injectors, see Fig. 3.1 on p. 14. The final design of the shielding boxes for the injector boxes is shown schematically in blue in Fig. 3.1. The sources and first parts of the neutralisers are mounted at the back of the injector box. They are shielded by an iron box, shown in Fig. 3.3 on p. 15. The region of the second parts of the neutralisers, the ion dumps and the deflection magnet is shielded from the stray field of W7-X by iron plates inside of the injector box. The region between the deflection magnet and the torus is not shielded, because the optimised magnetic field of W7-X would otherwise be negatively influenced [37].

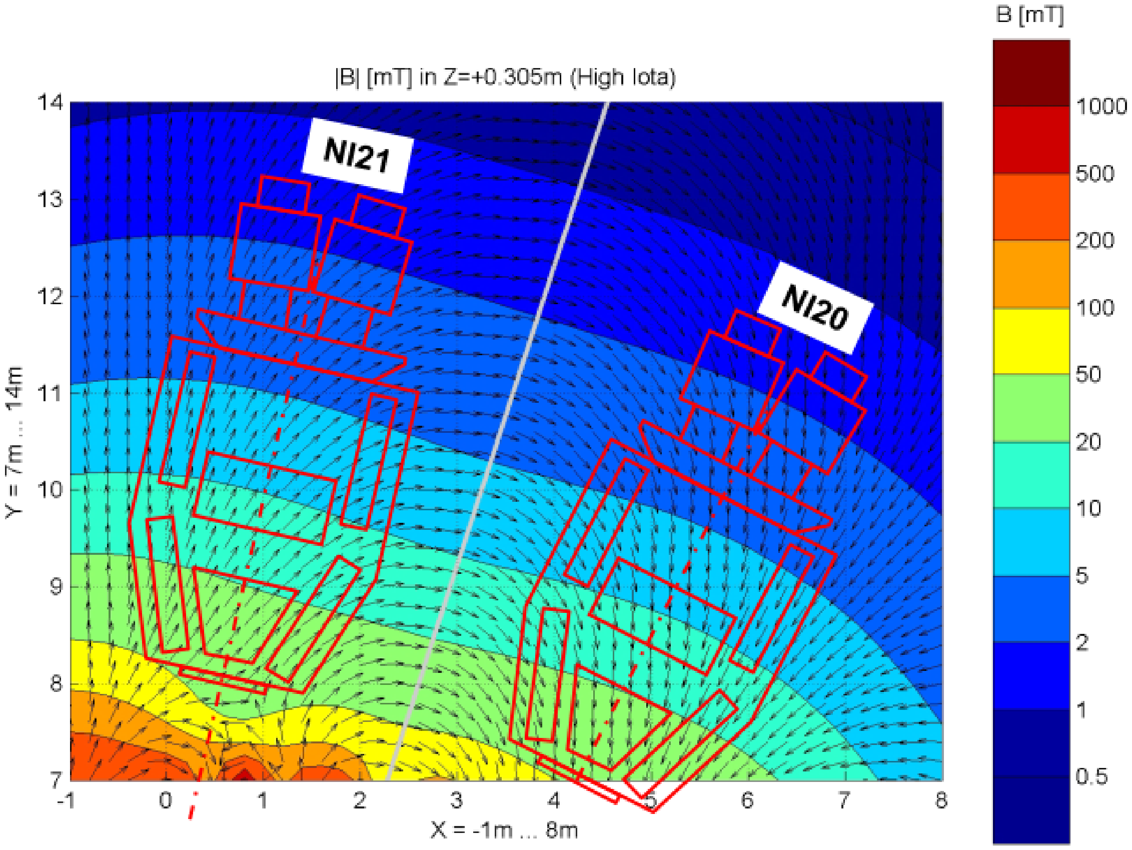

Figure 3.14: Pure magnetic stray field of W7-X for the high iota configuration without any shielding of the injectors (adapted Figure from [36]). The position of the injectors is marked in red. In the centre of the plasma the magnetic field strength is about 3 T. At the deflection magnets the stray field is between 10 and 20 mT but only 2 to 3 mT are allowed for NBI operation. Therefore, iron plates for magnetic shielding were installed inside the injector box. Since the stray field at the RF sources would be about 2 to 5 mT, which exceeds the allowed value of 0.2 to 0.3 mT, additional magnetic shielding around the sources has been installed.

4

EVALUATION

The analysed pulses are some of the first pulses of the first commissioning and operation phase of the NBI system at W7-X. Therefore, the parameters of the pulses were mainly chosen to get the sources ready for operation. Dedicated NBI pulses could not be done for this work. The number of the available pulses and thus the parameter settings, is therefore limited. For this reason, there are no systematic parameter scans, except for the operation of the deflection magnet with S7. All other pulses used for the analysis are chosen from the available data. They have the least deviation of other parameters and thus come closest to a systematic parameter scan.
This chapter is about the evaluation of the measurements and the results. There are two main topics. First, the calorimetric analysis leading to an estimate on the combined injected power of S7 and S8 of (3.1 ± 0.8) MW for a typical full power NBI pulse, is presented. This is about 33 % of the initially generated electric beam power of (9.4 ± 0.6) MW. Second, the influence of the magnetic stray field of W7-X on the extracted current in the NBI system is discussed. A clear dependence of the source performances on the stray fields of three different magnetic field configurations (KJM, EJM, FHS) or on the operation of the trim coil between the two beam boxes was not observed. However, independent of the stray field, S7 showed a better performance than S8.

4.1 CALORIMETRY

Calorimetry on the NBI system means the calculation of how much of the electric energy needed to generate the beam pulse is transferred to which of the NBI components by analysing the cooling water (cf. Sec. 2.2). The electric beam energy $E_{el} = UI_{ext}t_{NBI}$ is used to accelerate the beam particles and is thereby transformed to kinetic energy of the particles. The beam particles transfer their kinetic energy to any component they strike. The thermal energy of the component is transferred to the cooling water. This energy E in the cooling water is calculated according to:

$$E = c\rho \int_{t_0}^{t_1} \dot{V} \Delta T dt. \tag{4.1}$$

ρ is the density, c the specific heat capacity, $\dot{V}$ the flow rate of the water and ΔT is the increase of the water temperature caused by the absorbed energy. The temperature and flow rate of the cooling water are measured and saved in an archive as raw data. In the framework of this thesis, an evaluation routine for calorimetry on the NBI system was developed in Python. The routine loads the NBI data of a single pulse from the data archive and calculates the energy in the cooling water of the NBI components individually. The measured data have to be corrected in various ways to get physically meaningful data, because the NBI cooling system was not designed for calorimetry. The routine is described in detail in Sec. 4.1.1 *Preparation of the Measurement Data*. This is followed by the calorimetry results. At first, energy accounting is done on one commissioning and one in-vessel pulse. Next are comparisons of various NBI commissioning pulses with different gas settings, different acceleration voltages and with and without operation of the deflection magnet. Finally, the calorimetric results of in-vessel pulses with and without W7-X plasma are presented and compared to results of two different NBI models and spectroscopic measurements.

The calculated energies are given as a fraction of the electric beam energy of the pulse in percent, referred to as *energy fraction*, in order to compare different NBI pulses. Using Eq. 2.1 and 4.1 the energy fraction is then given by:

$$\begin{aligned} \text{energy fraction}[\%] &= 100 \cdot \frac{\text{energy detected calorimetrically (at a component)}}{\text{energy of the initial ion beam}} \\ &= 100 \cdot \frac{E_{calorimetry}}{E_{el}} = 100 \cdot \frac{c\rho \int \dot{V} \Delta T dt}{U\, I_{ext}\, t_{NBI}}. \end{aligned} \tag{4.2}$$

For commissioning pulses, ideally 100 % of the electric beam energy can be accounted for in the calorimetric analysis. However, in reality the energy fraction of the sum of all calorimetrically measured energies is below 100 %, since not all components are cooled with water and not all pipes are equipped with sensors and not all sensors were operational. For example, in the NBI system of AUG 92 % is measured [29]. If the neutral beam is injected into the plasma, the absorbed energy is not measured directly and the amount of total measured energy is lower. This amount depends on the absorption of the plasma and thus on the plasma parameters. Comparison of similar commissioning and in-vessel pulses provide information about the absorption by the plasma. Note that the energy fraction detected at the calorimeter is equivalent to the neutralisation efficiency η of the NBI system, since it is the ratio of the energy of the neutrals to the energy of all extracted particles, which is the electric beam energy of the pulse.

4.1.1 *Preparation of the Measurement Data*

The preparation of the measurement data for the calorimetric analysis is described in this section. It begins with a detailed description about how each parameter of Eq. 4.1 is inferred from the measurement data. This includes the treatment of signal disturbances or faulty sensors and other effects of the cooling system, which was not designed for calorimetry in the first place. The preparation is done automatically with an evaluation routine which was developed in the frame of this work.

The specific heat capacity c and density ρ of the cooling water are simple factors in Eq. 4.1. For all calculations $c = 4182\,\text{J}/(\text{kg}\,\text{K})$ and $\rho = 998.2\,\text{kg}/\text{m}^3$ are used [38]. The dependence on temperature and pressure are neglected in the calculation but discussed in Sec. 4.3. The other parameters in the equation depend on the time. The temperature and flow rate of the cooling water as functions of time are measured by thermocouples or PT100 temperature sensors and flowmeters as explained in Sec. 3.2. The collected data is saved and stored in the W7-X data archive. The evaluation routine is loading these data for the desired NBI pulse and converts the default measurement units to the desired units. The following describes how the flow rate $\dot{V}(t)$ and the rise in the temperature $\Delta T(t)$ are determined from the measurement data. Then, the identification of the optimal integration limits t_0 and t_1 is explained.

The Flow Rate $\dot{V}$

Systematic disturbances of flow rate measurement signals are observed in coincidence with the RF and voltage signals. A grounding issue is suspected. The affected flow rate measurement signals are those of the plasma grid and RF source, as well as of all parts of the NBI components, cooled with water from the high flow rate cooling circuit. Fig. 4.1 gives an example of the flow rate measurement of the cooling water of the ion dumps. The measurement (blue) compares two subsequent flow rate pulses. For the first one, the cooling water was operated as usual, but the RF sources were turned off so that no beam was created. Therefore, the orange RF source power signal and the green acceleration voltage signal were not turned on. In contrast, the second pulse is a usual NBI pulse with powered sources. Thus, the RF source power signal rises to 148 kW and the acceleration voltage signal to 49 kV. Two seconds before the NBI pulse the start of the RF pulse coincides with a sharp drop in the flow rate signal. During the high voltage pulse the flow rate measurement is disturbed again. A drop like this in the flow rate is unrealistic. The exact cause of the measurement disturbance is not clear. However, these disturbances scale with the RF and voltage signals and occur only in coincidence with them. Since all affected signals are in the same control cabinet, a grounding issue is suspected. In the developed evaluation routine, a linear interpolation of the signal is used to replace the perturbed signal during the RF power and high voltage pulses. Otherwise, the original values are used for the energy calculation. The linear correction is shown in Fig. 4.1 in red.

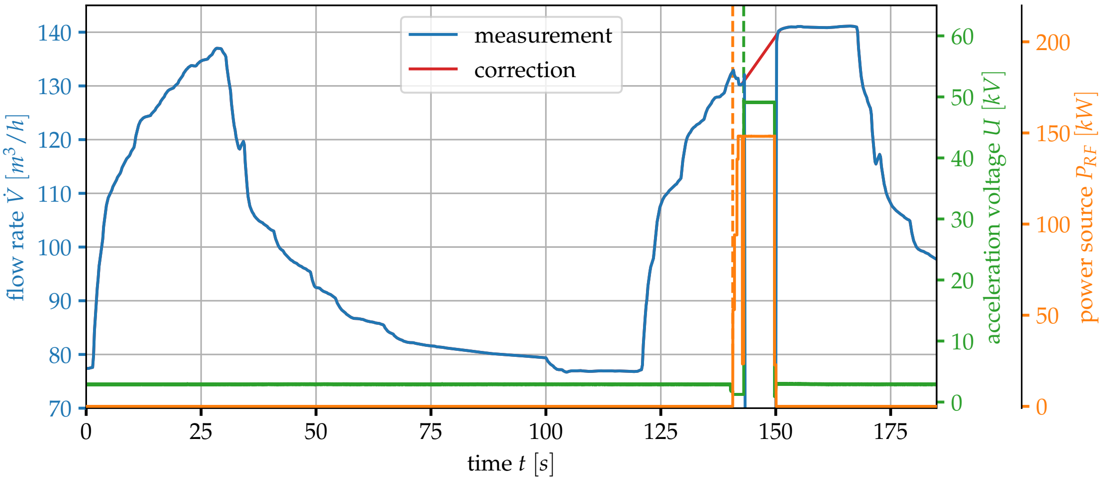

Figure 4.1: Exemplary flow rate measurement of the ion dumps cooling water from 09.10.2018 06:56:13 to 06:59:20 UTC. The measured flow rate signal in blue shows a decrease coinciding with the RF signal in orange and the high voltage signal in green. At $t = 141$, marked by the dashed orange line, the flow rate signal level decreases by $3\,\mathrm{m}^3/\mathrm{h}$ for 2 s. Then the signal level drops again at $t = 143$, marked by the dashed green line, and rises again after 7 s. This behaviour is physically unrealistic for the flow rate. Therefore, both signal drops are expected not to be due to a change in the flow rate but due to a technical error caused by perturbations of the RF amplifier or the switching of the high voltage. Thus, the measurement data during the RF and high voltage pulse are replaced by a linear interpolation between unperturbed signal parts. This linear correction of the blue measurement signal is shown in red.

The Temperature Rise ΔT

The challenge in getting the temperature rise $\Delta T(t) = T(t) - T_0(t - \Delta t)$ lies in the correct determination of the two temperatures $T(t)$ and $T_0(t - \Delta t)$ at the correct times, because the inlet temperature is not constant. Therefore, the different physical distances between inlet and outlet sensors and the measurement conditions must be taken into account. Different ways of determining the temperature rise are applied depending on the quality of the temperature measurements. These are described and motivated in detail in the following section, firstly, for the inertially cooled, secondly, for the actively cooled and thirdly, for the duct and beam dump components.

For the *inertially cooled components* of the injector the temperature signal rise is calculated by subtracting the inlet from the outlet water temperature signal. Since the water is moving several meters from the inlet sensor through or alongside the NBI component to the outlet sensor, a time shift Δt occurs. This shift was measured for every component without NBI operation using fluctuations in the temperature signal. Two corresponding maxima were identified and their positions compared. Fig. 4.2 shows the time shift for the box exit scraper.

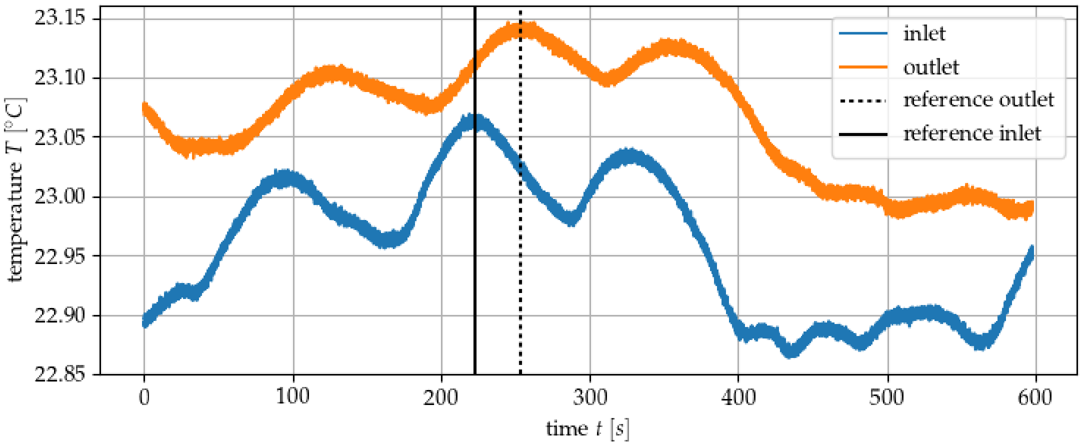

Figure 4.2: Time shift analysis exemplarily for the temperature signal of the box exit scraper. The signal in orange corresponds to the inlet water temperature and the one in blue to the outlet, delayed by approximately $\Delta t = 31\,\mathrm{s}$. The time shift is marked in black at the corresponding maxima.

There are two more differences in the signals. First, one can observe a broadening of the signal structure. This can be seen best in the temperature signal drop of the last of the three main maxima and in the relations of neighbouring maxima and minima. The effect is big in time but small in temperature. It is neglected in the evaluation routine, but taken into account for the error estimation in Sec. 4.3. Second, a discrepancy in the absolute values of the temperature signals of about 0.1 K can be observed. This discrepancy is not larger than 0.3 K for all inertially cooled components. It is compensated by subtracting the offset from the outlet values. The offset is calculated for the first values of the inlet and outlet temperature signals after the correction of the shift in time. This leads to a definition of the temperature rise as follows: $\Delta T_{ic\ box}$ is the difference between the

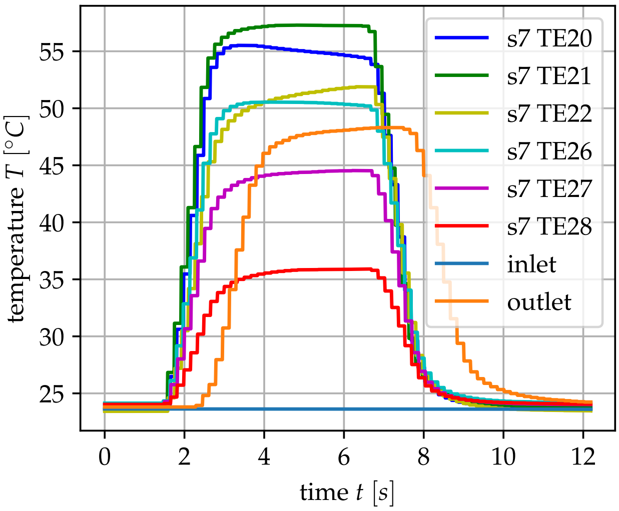

Figure 4.3: Temperature signals of the parts of the calorimeter for S7 that are actively cooled of the internal pulse 20181008n1257 with 54 kV for 5.2 s. The sensors TE20-22 and TE26-28 of the six panels measured the heat load in the water. The inlet water temperature is shown in blue. The outlet water is shown in orange. It is measured in the pipe where the water from the panels is combined again. As expected, it is delayed by about 0.8 s compared to the panel sensor signals and the outlet temperature agrees with the mean temperature of the six panels within the error margins (the exact hydraulics are not taken into consideration). The steps in the signals stem from the sampling rate.

current outlet water temperature $T(t)$ and the inlet one shifted in time $T_{inlet}(t - \Delta t)$ and the offset between the temperature signals T_{offset}:

$$\Delta T_{ic\ box}(t) = T(t) - T_{inlet}(t - \Delta t) - T_{offset} \tag{4.3}$$

For the *actively cooled components* the inlet water temperature is constant within the range of interest. Since the time scale of the heat pulse in the outlet signal is shorter than the fluctuations of the inlet signal, the calculation with the inlet water described above is neglected. Instead, the temperature rise $\Delta T_{ac\ box}$ is defined as the difference between the current outlet water temperature signal $T(t)$ and the outlet temperature immediately before the NBI pulse $T(0)$:

$$\Delta T_{ac\ box}(t) = T(t) - T(0) \tag{4.4}$$

The temperature signals of the actively cooled calorimeter panels of S7 are shown in Fig. 4.3. The sensors measuring the temperature of the water that is guided through the panels of the calorimeter show the heat load on these panels. The inlet water temperature signal is shown in blue, the outlet in orange. Although the pulse was done with almost maximum power, the temperature pulse in the signal is not much longer than the 5.2 s pulse, which demonstrates the effective cooling. The water temperature signal reaches the starting value within 4 s after the end of the pulse.
For the examined *components in the duct and beam dump* the temperature of the inlet is subtracted from the temperature of the outlet. Additionally, a linear approximation of the outlet signal noise before and after a pulse is chosen for T_0 and referred to as

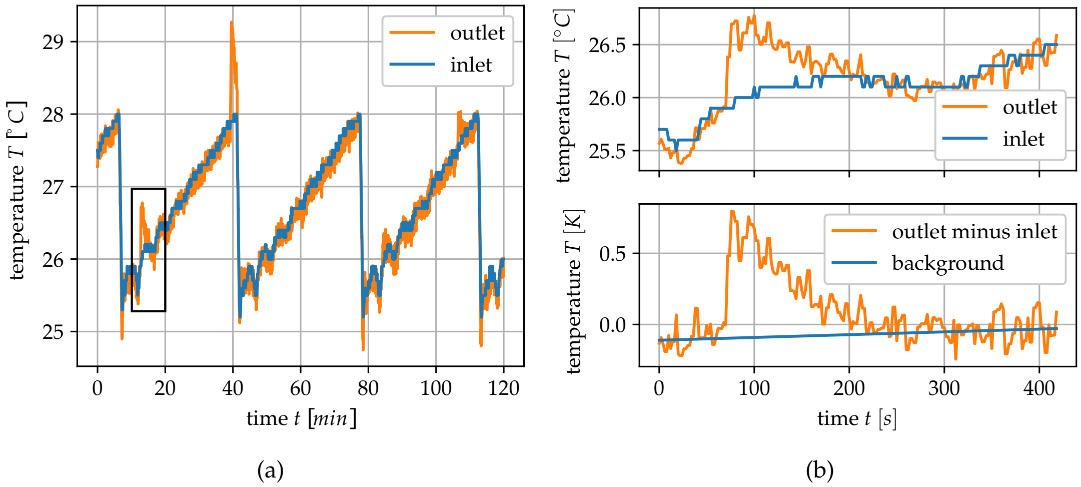

Figure 4.4: Temperature of the cooling water for the W7-X vessel components, exemplarily for the heat shield. (a) The inlet temperature is shown in blue and the outlet temperature of the heat shield cooling water in orange. In about 35 min the water temperature rises slowly by about 3 °C and then drops down again sharply. Water from a cooler reservoir is used as soon as the inlet water temperature reaches 28 °C. The pulse at $t = 12$ min (20181009.016), marked by the black frame, is presented in detail with reset time and different scaling of the axes in (b): (top) The output temperature signal related to the heat shield is shown in orange. The inlet temperature signal is shown in blue. (bottom) The output temperature signal minus the inlet one is shown in orange. The linear fit of the background is shown in blue.

the *background*. The temperature signal of the inlet cooling water shows a sawtooth-shaped behaviour: it rises from 25 °C to 28 °C within 35 min and then falls sharply back to 25 °C to slowly increase again as can be seen in Fig. 4.4a. This behaviour is caused by the automatic cooling water control mechanism, which keeps the inlet water temperature below 28 °C. In addition, the inlet water temperature measurement is performed with a low sampling rate and rough binning. Moreover, the signal of the outlet water temperature is affected by noise. The rise in the temperature of the cooling water shows signal to noise ratios not higher than 10. For this reason a linear approximation of the background is used for the calculation of the temperature rise:

$$\Delta T_{ic\ vessel}(t) = T(t) - T_{inlet}(t) - T_{background}(t). \tag{4.5}$$

In Fig. 4.4b the temperature signal of the outlet water from the heat shield of pulse 20181009.016 is shown in orange. The inlet water temperature (a, b top) and the linear approximation of the background (b bottom) are shown in blue. For the latter the measurement data of the first and the last minute of the 6 min interval around the pulse are used to fit the background. This leads to the time interval selection.

The Integration Limits t_0 and t_1

The integration time interval is selected so that preferably only the time of the heat pulse is taken into account. The integration time is chosen as short as possible, as will be described in detail in the following, particularly because of the fluctuations and broadening in the temperature signals. The integration end has to fulfil one boundary condition, namely to be in the time interval between the NBI pulse of interest and the next one. The high voltage signal of the NBI is used as an indicator for start and end times of the NBI pulse. The evaluation routine loads the high voltage signal for 11 min from a time entered by the user and checks for NBI pulses. In this paragraph, the integration time settings for the various components are presented one by one: firstly, the inertially cooled, secondly the actively cooled and thirdly, the duct and beam dump components.

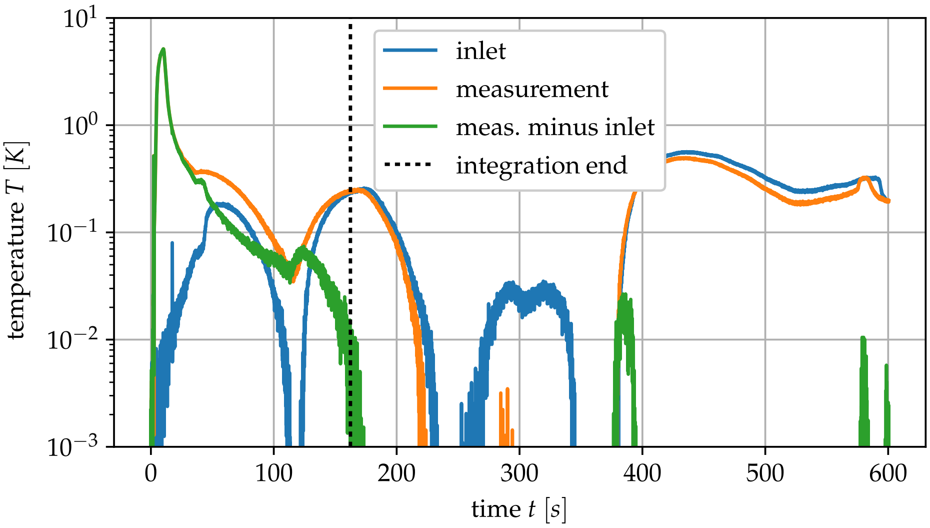

Figure 4.5: Integration time limit for inertially cooled components, using the example of the ground- and deceleration grids and the first half of the neutraliser. The temperature is plotted on a logarithmic scale. In orange the outlet water temperature, in blue the inlet and in green the outlet minus the inlet for pulse 20180925n0719. The latter is the one that is integrated for the calculation of the energy. The dashed black line marks the integration end for this component and for this pulse.

The integration time interval for the *inertially cooled components* in the injector box is defined as the time interval from 1 s before the NBI pulse starts to individual end times. Integration over the time before and after the temperature pulse would roughly equal zero, because there is no rise in temperature, so $\Delta T \approx 0$. But the remaining discrepancies of inlet and outlet water due to fluctuations and broadening in the temperature signal integrated over several minutes can lead to errors of the same order as the value itself. Therefore, the integration time interval is chosen as short as possible including the useful information and without disproportional effort. For this reason, the start time is set to be 1 s before the NBI pulse starts. And the end time is set at the first x axis crossing of the $\Delta T_{ic\ box}(t)$ signal, but at most 11 min after the start. In case the next pulse starts within the next 11 min, the maximum integration end is set to that time. In Fig. 4.5 the inlet water temperature of the Ground and Deceleration Grids and Neutraliser Part 1 (GDGN) is shown in blue. The outlet water temperature shifted in time is shown in orange and the signal $\Delta T_{ic\ box}$, which results from the subtraction, is shown in green. The value at $t = 0$ is subtracted from the three temperature signals, respectively, to show the increase caused by the pulse and for comparison. At around 162 s the end of the integration is marked by the dotted black line.

The integration time for the *actively cooled panels* is defined as the time interval from 1 s before the pulse starts to 6 s after the pulse ends.
The integration time for the *duct and beam dump components* is defined as the time interval from 1 min and 1 s before the pulse starts to 6 min later or to the start of the next NBI pulse, whichever comes first. The first and the last minute of the time interval are used to determine the background and, by subtracting the background, the integration equals zero before and after the pulse.

4.1.2 *Energy Accountability*

Energy accountability is the analysis of the energy flow in a system and thus, of the individual parts of the principle of conservation of energy. On the basis of conservation of energy, the total energy of the extracted ion beam (cf. Sec. 2.1.1) equals the energy of the various losses and of the injected beam (in-vessel pulses) or of the various losses and of the energy on the calorimeter (commissioning pulses). That means, for commissioning pulses the electric beam energy is converted completely to thermal energy in the components. For in-vessel pulses the total energy of the extracted beam is only partially converted to thermal energy at the components, because a significant amount of the neutral beam is absorbed by the plasma. Therefore, one can determine the uncertainty of the calorimetric measurements of the components in the injector box with a commissioning pulse. Additionally, one can determine the uncertainty of calorimetric measurements of the duct and vessel components with a pulse into the empty plasma vessel. Finally, one can calculate the injected energy with the previously determined uncertainty and the measured conversion losses. Moreover, the influence of single operating parameters on the energy flow can be analysed and, thus, the NBI operating parameters can be optimised.
In this first section of the calorimetry results the energy accountability of the NBI system is studied for one commissioning pulse. In addition, one in-vessel pulse is examined, analysing the energy flow in duct and plasma vessel, and the injected power is determined. A comparison to energy accountability studies of the NBI system at AUG concludes this section. In the following Sec. 4.1.3 *Commissioning Studies*, the influence of single operating parameters on the NBI performance are analysed. In Sec. 4.1.4 *Calorimetry in Duct and Beam Dump*, in-vessel pulses with and without plasma in the W7-X vessel are studied and the calorimetry results are compared to spectroscopic measurements and results of two different models, describing NBI at W7-X.
The calorimetrically measured thermal energies and the energy fractions of the commissioning pulse 20181009n0718 are listed in Tab. 4.1. Moreover, the energy fractions are presented in the left part of the schematic of the NBI system in Fig. 4.6. The extracted ion beams combined have an electric beam energy of $E_{el} = 48.8\,\mathrm{MJ}$. In the cooling water of the sources 4.0 % of the electric beam energy is detected. In the cooling water of the plasma grids 1.5 % is detected. These losses are caused, for example, by beam particles hitting one of the grids. This leads to heat loads there and to electrons, that are knocked out of the metal. The electrons can be accelerated into the source or at another grid, leading to further heat loads at these components. The energy in the cooling water of the GDGNs could not be measured for this pulse due to a defect sensor. The energy fraction of the GDGNs of similar pulses is about 2.1 %. Additional 7.8 % of the electric beam energy is lost in the second part of the neutralisers. This can be due to the beam

Table 4.1: Energy accountability of commissioning pulse 20181009n0718 and comparison to in-vessel pulse 20181009.016 and energy accountability of the NBI system at AUG [29]. Source parameters are listed in the first part and calorimetrically measured energies and energy fractions of the components in the second part of the table. *Box losses* is the sum of the energy fractions of RF sources, plasma grids and the second part of the neutralisers. *Duct losses* is the sum of the energy fractions of box exit scraper, copper cone and the duct liner. *Beam dump* is the sum of the energy fractions of heat shield and baffle. The energy at the calorimeter for the in-vessel pulse is expected to be due to the deflection process (*, cf. Sec. 4.1.3 *Influence of the Deflection Magnet*). Four sources are installed on the injector at AUG. The average acceleration voltage and the combined total electric beam energy and power for the presented pulse are given and marked with **.

Parameter	Values for the three pulses				
	W7-X				AUG
Pulse ID	20181009n0718		20181009.016		
Pulse Type	commissioning		in-vessel		
Beam Time [s]	5.2		4.0		5.0
Acc. Voltage S7 [kV]	54.2		53.1		**54.5
Acc. Voltage S8 [kV]	54.1		53.0		
Ext. Current S7 [A]	86.7		87.6		
Ext. Current S8 [A]	86.5		88.4		
El. Power S7 [MW]	4.7		4.7		**18.92
El. Power S8 [MW]	4.7		4.7		
El. Energy S7 [MJ]	24.4		18.6		**94.6
El. Energy S8 [MJ]	24.3		18.7		
Component	[MJ]	[%]	[MJ]	[%]	[%]
RF Sources	1.9	4.0	1.8	4.8	4.0
Plasma Grids	0.7	1.5	0.6	1.7	2.2
Neutralisers 2	3.8	7.8	3.2	8.5	4.4
H_2^+ Dumps	1.1	2.3	0.9	2.3	2.1
H^+ Dumps	12.3	25.2	9.5	25.3	31.0
Calorimeter	19.4	39.8	*0.2	*0.5	46.4
Box Exit Scraper			0.2	0.6	1.8
Copper Cone			0.8	2.1	
Duct Liner			1.5	3.9	3.3
Heat Shield			0.6	1.6	
Baffle			0.3	0.7	
Measured Total	39.3	80.6	19.3	51.6	92.0
Box Losses	6.4	13.2	5.6	15.0	10.6
Duct Losses			2.5	6.6	5.1
Beam Dump			0.8	2.3	

being scraped off: the larger the beam divergence, the more particles strike the walls of the neutraliser. Moreover, particles hit the walls of the neutraliser due to the collisions in the neutraliser. The *box losses* is the sum of the calorimetrically measured energy in the cooling water of the RF sources, the plasma grids and the neutralisers. At these components 13.2 % energy fraction is detected, plus the 2.1 % at the GDGNs. Therefore, the beams have only 84.7 % of their initial energy, when they come out of the neutralisers. The heat load at the magnet liners could also not be measured. It is expected to be about 6 % of the electric beam energy, according to test bed measurements at AUG. Positively charged molecules are deflected onto the H_2^+ dumps (2.3 %) and positively charged atoms onto the H^+ dumps (25.2 %). An energy fraction of 16.7 % is detected in the cooling water of the actively cooled centre parts of the H^+ dumps, 8.5 % in the cooling water of the inertially cooled parts around the centre. The neutrals are not affected by the magnetic field, so they hit the calorimeter. Here, 39.8 % is measured in the cooling water. An energy fraction of 37.1 % is detected in the cooling water of the actively cooled centre parts of the calorimeter, 2.8 % in that of the inertially cooled parts around the centre.

All calorimetrically measured energies sum up to 80.6 % of the electric beam energy of S7 and S8. Not included is the energy in the cooling water of the GDGNs (2.1 %) and the magnet liners (6 %), because it could not be measured. Additional 8.1 % are expected here, due to the measurements at AUG and at W7-X during earlier pulses, when the sensor at the GDGNs was still functional. Thus, 88.7 % of the electric beam energy can be accounted for. There are indications that additional losses occur due to the deflection process. A comparison of a pulse with operation of the deflection magnet to one without operation of the deflection magnet showed additional losses of about 8 % (cf. Sec. 4.1.3 *Influence of the Deflection Magnet*). Taking those additional losses into account, almost 100 % of the electric beam energy can be accounted for. However, further experiments are required to check whether these losses are not already covered by the estimation of the energy fraction of the magnet liners.

The calorimetry results of the in-vessel pulse 20181009.016 are also listed in Tab. 4.1 and shown in the right side of the schematic of the NBI system in Fig. 4.6. The calorimeter is retracted for the in-vessel pulse so that the beams are injected into the plasma vessel. The beams are scraped by the box exit scraper (0.6 %), the copper cone (2.1 %) and the duct liner (3.9 %). The duct losses, which is the sum of these three energy fractions, add up to 6.6 %. In this experiment, most of the injected beam particles are ionised in the plasma. The non-ionised beam particles end up on the beam dump. Here, 2.3 % of the electric beam energy is detected, 1.6 % in the cooling water of the heat shield and 0.7 % in the baffle. The ratio of the energy found on the beam dump to the injected beam energy is called shine through. The shine through for the beam and plasma parameters of the example shown (20181009.016) is about 6.8 %.

The injected beam power P_{inj} can be calculated by subtracting all known losses from the electric beam power apart from the beam dump. This would lead to 40.3 % of the electric beam power P_{el} as injected power P_{inj}. But since the energy accountability is not complete, this calculation results in an overestimate. It is considered to be more accurate to take the energy fraction of the calorimeter of a commissioning pulse and subtract only the duct losses. Thus, the uncertainty of the calorimetry of all components in the injector box but the calorimeter do not enter this calculation. Therefore, the operating parameters and losses along the beam path up to the calorimeter are required to be as similar as

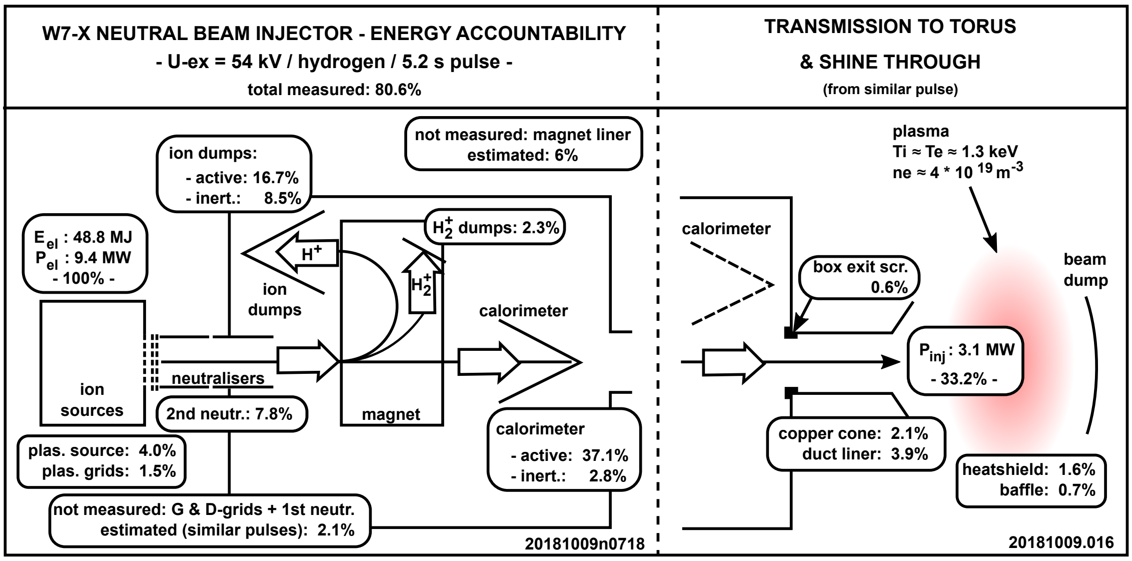
W7-X NEUTRAL BEAM INJECTOR - ENERGY ACCOUNTABILITY
- U-ex = 54 kV / hydrogen / 5.2 s pulse -
total measured: 80.6%
TRANSMISSION TO TORUS
& SHINE THROUGH
(from similar pulse)
ion dumps:
- active: 16.7%
- inert.: 8.5%
not measured: magnet liner
estimated: 6%
E_{el} : 48.8 MJ
P_{el} : 9.4 MW
- 100% -
H^+
ion
dumps
H_2^+ dumps: 2.3%
H_2^+
calorimeter
ion
sources
neutralisers
2nd neutr.: 7.8%
magnet
plas. source: 4.0%
plas. grids: 1.5%
calorimeter
- active: 37.1%
- inert.: 2.8%
not measured: G & D-grids + 1st neutr.
estimated (similar pulses): 2.1%
20181009n0718
plasma
Ti ≈ Te ≈ 1.3 keV
ne ≈ 4 * 10 ^{19} m^{-3}
calorimeter
box exit scr.
0.6%
beam
dump
P_{inj} : 3.1 MW
- 33.2% -
copper cone: 2.1%
duct liner: 3.9%
heatshield: 1.6%
baffle: 0.7%
20181009.016

Figure 4.6: Energy accountability for two full power pulses of the NBI system at W7-X (Figure adapted from [29]). The diagram shows the water cooled components along the beam path (from left to right) of an NBI injector. The measured energy fractions are annotated. The left part shows the injector with the calorimeter in lowered position. The energy fractions are those of the commissioning pulse 20181009n0718. The total measured energy accounts to 80.6 % of the electric beam energy. The right side of the diagram shows the duct components, the W7-X plasma and the beam dump. The annotated energy fractions and plasma parameters are those of the in-vessel pulse 20181009.016. The injected Power P_{inj} is calculated to be 33.2 % of the electric beam power. The shine through is about 6.8 %.

possible for the commissioning pulse and the in-vessel pulse. Otherwise, the energy fraction of the calorimeter is not expected to match the energy fraction of the beams of the in-vessel pulse at the entry of the duct. This way, 33.2 % of the electric beam power ($P_{el} = 9.4\,\mathrm{MW}$) is calculated to be injected into the plasma, which is $P_{inj} = 3.1\,\mathrm{MW}$.
The comparison of the two pulses in Tab. 4.1 shows, that the measured energies at the components in the injector box are lower for the in-vessel pulse, although the energy fractions are similar. This is due to the fact, that the in-vessel pulse was 1.2 s shorter than the commissioning pulse. The electric beam power is the same and therefore, the energy fractions, are similar. The energy fractions of the two compared pulses differ by about ±0.8 % per component.
Calorimetric studies were also carried out on AUGs NBI system [29], which is similar to the one at W7-X. There, the energy accountability is almost complete with 98 %. They detected 92.0 % of the electric beam energy in the cooling water of the components and additional 6 % are expected at the magnet liners. The energy or power accountability schematic of the NBI system at AUG is shown in Fig. 4.7. The injected power at AUG is calculated to be 36.75 % of the electric beam power and is therefore similar, but higher than at W7-X (33.2 %). The detected energy fractions of the sources, the plasma grids, the GDGNs and the H_2^+ dumps at AUG match those at W7-X within ±0.8 % energy fraction. But the lost energy fraction at the second part of the neutralisers at AUG is lower by more than 3.4 %. This could be an indication of a larger beam divergence or a not fully optimised neutraliser gas setting or incomplete shielding from the stray field of W7-X, so that the ion beam is slightly deflected. In addition, at the actively cooled parts of

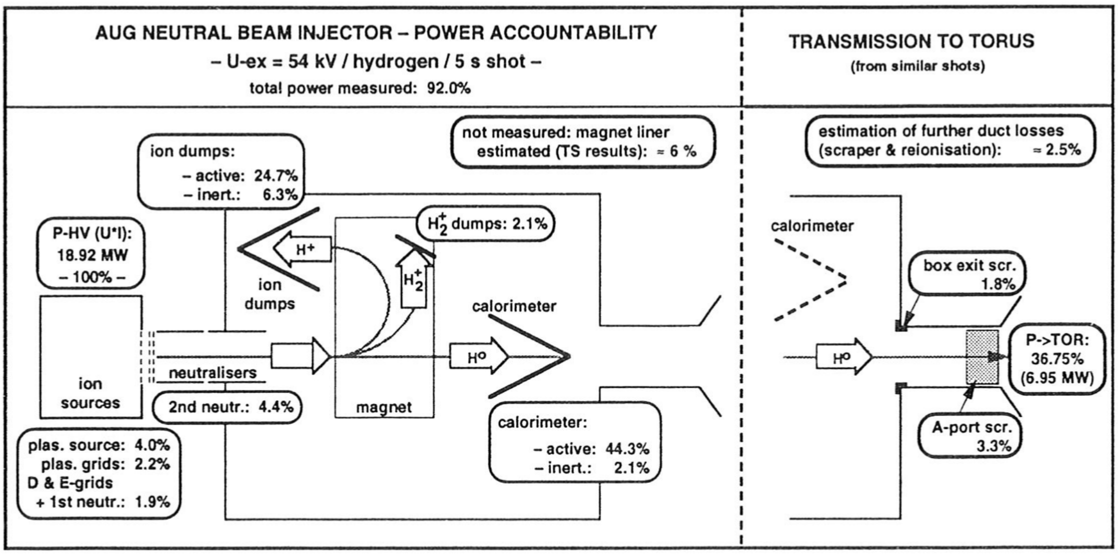
AUG NEUTRAL BEAM INJECTOR – POWER ACCOUNTABILITY
– U-ex = 54 kV / hydrogen / 5 s shot –
total power measured: 92.0%
TRANSMISSION TO TORUS
(from similar shots)
not measured: magnet liner
estimated (TS results): ≈ 6 %
estimation of further duct losses
(scraper & reionisation): ≈ 2.5%
ion dumps:
– active: 24.7%
– inert.: 6.3%
P-HV (U*I):
18.92 MW
– 100% –
H+
ion
dumps
H2+ dumps: 2.1%
H2+
calorimeter
calorimeter
box exit scr.
1.8%
ion
sources
neutralisers
2nd neutr.: 4.4%
magnet
H0
H0
P->TOR:
36.75%
(6.95 MW)
calorimeter:
– active: 44.3%
– inert.: 2.1%
A-port scr.
3.3%
plas. source: 4.0%
plas. grids: 2.2%
D & E-grids
+ 1st neutr.: 1.9%

Figure 4.7: Energy or power accountability for the NBI system at AUG (Figure from [29]). The diagram shows the water cooled components along the beam path (from left to right) of an NBI injector. The measured energy fractions are annotated. The left part shows the injector with the calorimeter in the lowered position for a commissioning pulse. The total measured energy accounts for 92.0 % of the electric beam energy. The right side of the diagram shows the duct components. The injected Power P_{inj}, which is the power into the torus (P->TOR), is calculated to be 36.75 % of the electric beam power.

H^+ dumps and calorimeter the energy fractions at W7-X are lower than at AUG by 8.0 % and 7.2 %, respectively. But the inertially cooled parts of H^+ dumps and calorimeter at W7-X have energy fractions which have 2.2 % and 0.7 % larger values. These data seem to suggest that the neutral gas density in the neutraliser is too low. Therefore, the neutralisation efficiency would be smaller, which would lead to less neutral particles and energy at the calorimeter. Moreover, this would result in less gas flow out of the neutraliser into the magnet region, which is needed to prevent space charge expansion of the beam ions [30]. Thus, this would result in increased power loads at the magnet liners and could also explain the higher energy fractions at the inertially cooled and lower energy fractions at the actively cooled parts of the H^+ dumps in comparison to AUG. Additional losses due to the deflection process would also explain less energy at H^+ dumps and calorimeter, but cannot explain the observed higher energy at the inertially cooled parts. If one or both of these theories are the reason for the results remains unclear, because the energy in the cooling water of the magnet liners could not be measured and the neutral gas density in the magnet area is unknown.

4.1.3 *Commissioning Studies*

The results of the analysis of various NBI commissioning pulses are presented in this section. First, the neutraliser gas setting is optimised for the highest NBI performance. This is followed by the study of pulses with different acceleration voltages as consistency check for the connection with the neutralisation efficiency. Finally, one NBI pulse with and one pulse without operation of the deflection magnet are compared to study the deflection process.

Influence of the Gas Setting in the Neutraliser

A systematic scan of the gas flow rate settings in the neutraliser was carried out to optimise the neutralisation process. Four pulses were performed on 15.08.2018 with S7, each with an acceleration voltage of about 46 kV. The flow rate of the gas injected into the neutraliser was increased in three steps from 21 to 31 mbar l/s. All four pulses were performed with the same parameters, which are listed in Tab. 4.2. The source gas flow rate was set to 18 mbar l/s. The beam time is different for every pulse.

Table 4.2: List of the source parameters (top) and energy fractions measured on components (bottom) of S7 for the four NBI pulses of the systematic scan of the neutraliser gas flow rate. The energy fraction detected at the calorimeter is equivalent to the neutralisation efficiency η of the NBI system. The energy fractions measured on the H^+ and H_2^+ dump are added up and labelled as *ion dumps*. The sum of the energy fractions of RF source, plasma grid and the second part of the neutraliser is referred as *box losses*.

PARAMETER	VALUES FOR THE FOUR PULSES			
Gas N [mbar l/s]	21	24	27	31
Pulse ID	20180815n1209	20180815n1228	20180815n1402	20180815n1413
Beam Time [s]	5.68	4.14	5.62	5.50
Acc. Voltage [kV]	45.6	45.6	45.7	45.7
Ext. Current [A]	67.3	68.6	67.7	66.9
El. Power [MW]	3.1	3.1	3.1	3.1
El. Energy [MJ]	17.4	13.0	17.4	16.8
COMPONENT	ENERGY FRACTIONS FOR THE FOUR PULSES [%]			
Box Losses	13.4	12.6	12.6	11.6
Ion Dumps	23.9	24.3	24.3	24.2
Calorimeter	45.2	46.5	47.4	48.0
Measured Total	82.5	83.4	84.2	83.8

The results of the systematic scan of the neutraliser gas flow rate are depicted in Fig. 4.8 and listed in Tab. 4.2. The neutralisation efficiency is rising and the box losses are decreasing with increasing gas flow rate. Neither drop nor saturation for high gas flow rates is observed. Therefore, the highest tested gas flow rate of 31 mbar l/s is the best among those tested for this setting of parameters.

The energy fraction measured at the H^+ dump is also increasing with the gas flow rate. The energy fraction on the H_2^+ dump decreases continuously with increasing gas flow rate. That indicates that the number of neutralisation processes of H_2 molecules increases with the gas flow rate. In addition, space charge expansion could cause decreasing heat loads at the H_2^+ dump for increasing neutral gas flow of the neutraliser into the magnet region. Without the calorimetric measurements at the magnet liners, where increasing heat loads with space charge expansion are expected, no conclusion can be drawn. Density measurements in the magnet region or space charge expansion simulations could also help to determine the cause for the decreasing heat load on the H_2^+ with increasing gas flow rate. The RF source and plasma grid are not influenced by the change

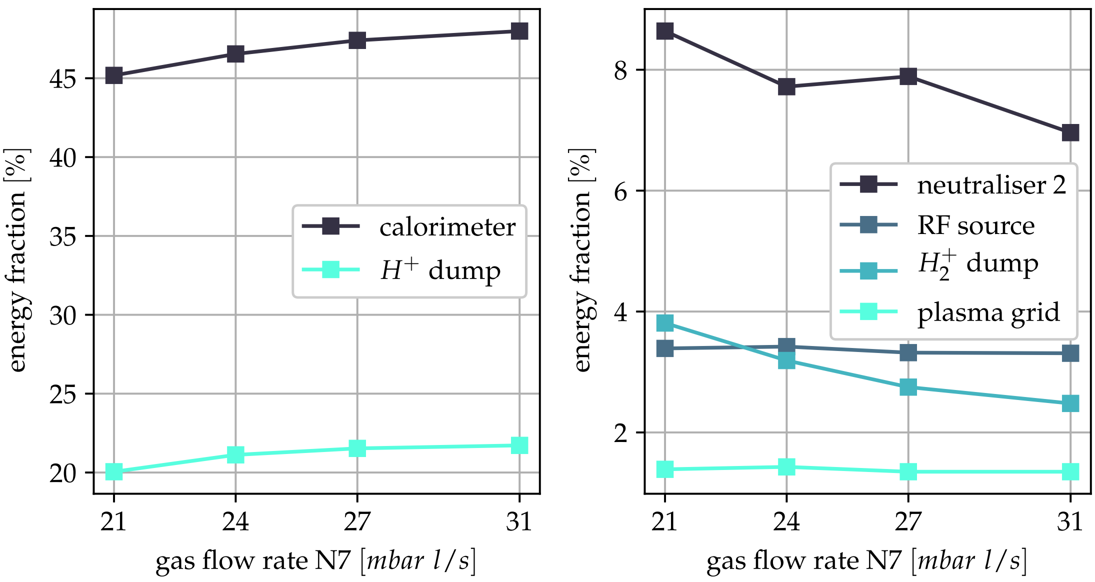

Figure 4.8: Energy fractions of the components in the injector box for various neutraliser gas flow rates for four pulses on 15.08.2018 with S7. The energy fraction detected at the calorimeter is equivalent to the neutralisation efficiency η of the NBI system.

in the neutraliser gas flow. The energy fractions for these components fluctuate by a maximum of ±0.1 % energy fraction. The second part of the neutraliser shows a decrease in the detected energy with increasing gas flow rate in total but not in a continuous way. This behaviour causes the decrease of the box losses. The total amount of energy detected on the components changes only in a range of less than 2 %. It seems unaffected by the change in the gas flow rate.
Henceforth, a source gas flow rate of 18 mbar l/s and neutraliser gas flow rate of 43 mbar l/s for active sources were used as default setting especially for pulses with acceleration voltages greater than 46 kV. The gas flow rate of an inactive source was set to 0 mbar l/s at the source and 31 mbar l/s at the corresponding neutraliser. However, no systematic scan with higher acceleration voltages or higher gas flow rates in the neutraliser was carried out, nor was a systematic scan of the gas flow rate settings in the RF sources. Whether the trend towards high neutral beam power and low box losses with increasing gas flow rate in the neutraliser, observed with these measurements, continues at higher acceleration voltages and higher gas flow rates is not clear.

Influence of the Acceleration Voltage

In this section the influence of the acceleration voltage on the NBI performance is examined, especially as a consistency check for the connection with the neutralisation efficiency (cf. 2.1.1 *Neutralisation*). The NBI system at W7-X is capable of acceleration voltages of up to 54 kV for hydrogen beams. It is the default setting for plasma experiments. The calorimetry data of three commissioning pulses with the acceleration voltages of 40 kV, 47 kV and 54 kV are compared. The other NBI settings were kept constant, except for the gas settings in the neutraliser. The 40 kV pulse was performed with only 18 mbar l/s, while the other pulses were performed with 43 mbar l/s. These pulses were chosen, because they have the least deviation of other parameters and thus

Table 4.3: List of the source parameters (top) and energy fractions measured on components (bottom) of both sources for three NBI pulses with different acceleration voltage. The energy fraction detected at the calorimeter is equivalent to the neutralisation efficiency η of the NBI system. The energy fractions measured on the H^+ and H_2^+ dump are added up and presented as *ion dumps*. The sum of the energy fractions of RF source, plasma grid and the second part of the neutraliser is referred to as *box losses*.

PARAMETER	VALUES FOR THE THREE PULSES		
Acc. Voltage S7 [kV]	39.7	47.3	54.0
Acc. Voltage S8 [kV]	39.7	47.4	54.0
Pulse ID	20181008n1209	20181008n1217	20181008n1257
Gas N [mbar l/s]	18	43	43
Ext. Current S7 [A]	51.3	75.6	92.6
Ext. Current S8 [A]	50.6	70.1	88.9
Beam Time [s]	6.70	6.84	5.20
El. Power S7 [MW]	2.0	3.6	5.0
El. Power S8 [MW]	2.0	3.3	4.8
El. Energy S7 [MJ]	13.7	24.5	26.0
El. Energy S8 [MJ]	13.5	22.7	25.0
COMPONENT	ENERGY FRACTIONS OF THE THREE PULSES [%]		
Box Losses	14.5	12.3	12.7
Ion Dumps	21.7	25.0	28.8
Calorimeter	51.1	48.1	42.2
Measured Total	87.3	85.4	83.7

come closest to a systematic parameter scan. Based on the results of the gas scan, higher losses in the neutralisers and at the H_2^+ dumps are expected for the 40 kV pulse. The data is listed in Tab. 4.3 and depicted in Fig. 4.9.

The results agree very well with the expectation of the dependence of the neutralisation efficiency on the acceleration voltage (cf. Sec. 2.1): the neutralisation efficiency decreases from 51.1 % to 42.2 % with increasing kinetic energy of the beam particles. The acceleration voltage is proportional to the electric beam energy and therefore to the kinetic energy of the beam particles. For higher voltages the number of neutral particles and thereby energy fraction on the calorimeter is lower. And the number of ions and thereby energy fraction measured on the dumps is higher for higher voltages. The box losses are highest for the 40 kV pulse. The main contributing factor to these losses is the second part of the neutraliser. Here the gas flow rate setting was changed during the scan. As expected from the results of the gas scan, the lower gas flow rate caused higher losses in the neutralisers and at the H_2^+ dumps. Both sources show these results when examined separately, as can be seen in Fig. 4.9.

However, the two sources behaved differently in this series of pulses. The current extracted from S7 is higher than from S8. For $U = 47\,\mathrm{kV}$ the difference is the largest

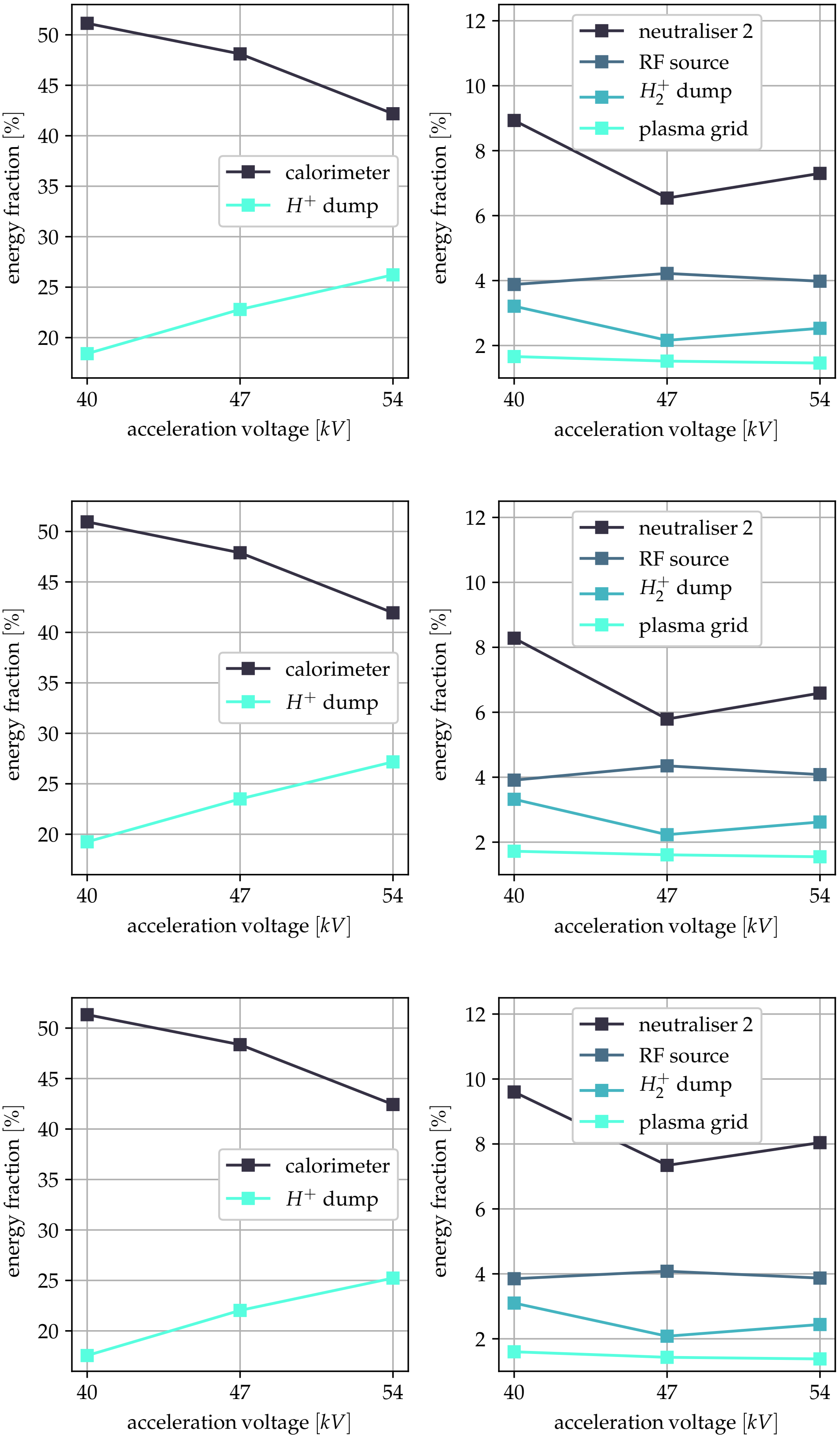

Figure 4.9: Calorimetry for various acceleration voltages for (top) both sources, (middle) S7 and (bottom) S8.

with 5.5 A. The energy fractions measured at the H^+ dumps are higher for S7 compared to S8. The difference is roughly the same for the three voltage steps with 1.5 % to 2.0 %. The energy fractions of the second part of the neutralisers and thereby the losses are also higher for S8. Here, the difference is 1.1 % to 1.2 %. In addition, the energy fractions of the calorimeter are slightly higher for S8 in comparison to S7. The difference is roughly the same for the three voltage steps with 0.3 % to 0.5 %. The cause of the different performance of the two sources is not clear yet.

Influence of the Deflection Magnet

This section focuses on the deflection process used to separate the neutrals from the ions. One pulse of S7 with operation of the deflection magnet is compared to one pulse without operation of the deflection magnet to study the influence of the deflection process on the energy accountability with calorimetry. The gas flow rate in source and neutraliser was set to 15 mbar l/s each. To protect the calorimeter the beam energy was limited. An acceleration voltage of 27.3 kV was used. That is why the neutralisation efficiency is higher than in the usual 54 kV pulses. The calorimetry data is presented in Tab. 4.4 and Fig. 4.10.

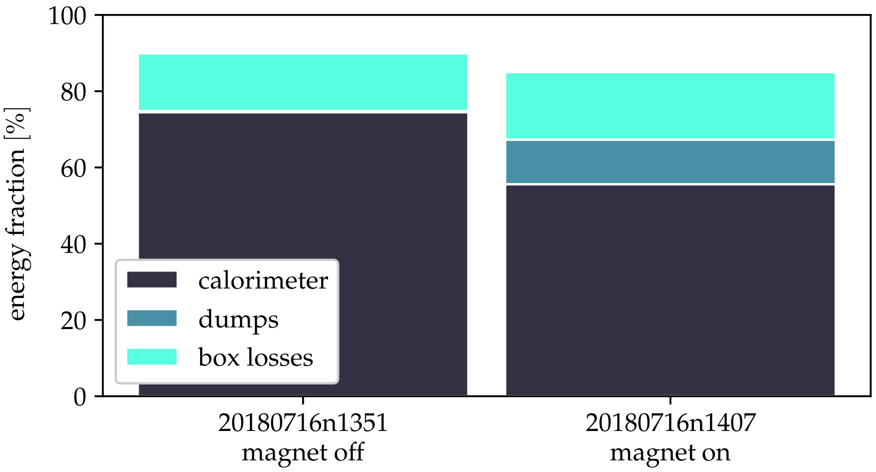

Figure 4.10: Energy fractions of the NBI components for two pulses, one with and one without operation of the deflection magnet. The experiment took place on 16.07.2018 with S7. The energy fraction detected at the calorimeter is equivalent to the neutralisation efficiency η of the NBI system. *Dumps* represents the sum of the energy fractions of the H^+ and H_2^+ dumps. The sum of the energy fractions of RF source, plasma grid and the second part of the neutraliser is referred to as *box losses*.

An energy fraction of 75 % was found at the calorimeter for the pulse without operation of the magnet. This almost matches the energy fraction of the dumps and the calorimeter for the pulse with operation of the magnet, which was 67 %. The discrepancy is a sign of undetected particle losses during the deflection process.

A part of the molecular ions in the beam was deflected past the ion dump in the deflection magnet. The trajectories then ended above the box exit scraper at the wall of the injector box and suspension of the calorimeter in case of commissioning pulses and at the calorimeter in case of in-vessel pulses. The cooling of the actively cooled parts of the calorimeter during in-vessel pulses was turned off, but the inertially cooled parts

Table 4.4: List of the source parameters (top) and energy fractions measured on components (bottom) of S7 for one NBI pulse with operation of the deflection magnet and one pulse without. The energy fraction detected at the calorimeter is equivalent to the neutralisation efficiency η of the NBI system. The sum of the energy fractions of RF source, plasma grid and the second part of the neutraliser is referred to as *box losses*. *Gas flow rate n & s* refers to the gas flow rate in the neutraliser and the RF source, each.

PARAMETER	VALUES FOR THE TWO PULSES	
Magnet Status	off	on
Pulse ID	20180716n1351	20180716n1407
Gas Flow Rate N & S [mbar l/s]	15	15
Acc. Voltage [kV]	27.3	27.3
Ext. Current [A]	35.1	35.7
Beam Time [s]	6.52	6.67
El. Power [MW]	1.0	1.0
El. Energy [MJ]	6.3	6.5
COMPONENT	ENERGY FRACTIONS FOR THE TWO PULSES [%]	
RF Source	4.3	4.4
Plasma Grid	2.4	2.4
Neutraliser 2	8.5	10.9
Box Losses	15.1	17.7
H_2^+ dump	0.1	2.8
H^+ dump	0.2	8.8
Calorimeter	74.5	55.6
Measured Total	89.9	85.0

were cooled as usual. Energy fractions of up to 0.5 % were measured there, validating the theory that the energy loss was due to deflected molecular ions. This was confirmed by calculations [39].

Simulations for deuterium operation show that the trajectories of D_3^+ and D_2^+ are only partially ending at the H_2^+ dump as well [40]. This is depicted in Fig. 4.11. More details about this simulation method can be found in [41]. Still, the amount of H_3^+ is expected to be negligibly small due to the high neutralisation efficiency of about 90 %. The amount of H_2^+ missing the H_2^+ dump is expected to be similar to the amount hitting the H_2^+ dump, which is 2.8 %, based on the simulations that show that roughly half of the H_2^+ particles are missing the dump (cf. Fig. 4.11a). Further measurements are required to calculate the actual amount of ions that do not hit any of the ion dumps. Additionally, reionisation and neutralisation along the beam path in the magnetic field of the deflection magnet lead to modifications of the typical trajectories, not all of which end on the calorimetrically observed components. In the first case, a neutral beam particle is ionised within the magnetic field and from then on influenced by the magnetic field and deflected. In the second case, a charged particle is neutralised on its bent

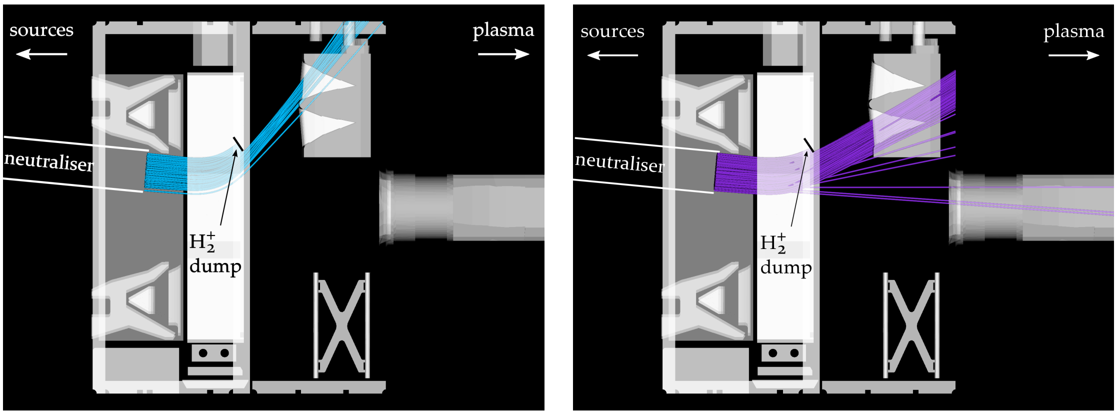

(a) (b)

Figure 4.11: Trajectories of (a) D_2^+ and (b) D_3^+ ions in the injector box at AUG with $U = 93\,\mathrm{kV}$ (Figures adapted from [40]). Six trajectories of beam particles, which are deflected less due to reionisation or neutralisation in the magnetic field of the deflection magnet, are shown in (b) exemplarily. The number of the trajectories does not represent the probability of the neutralisation and reionisation processes.

trajectory in the magnetic field and from then on moves in a straight line. Six of these trajectories are indicated in Fig. 4.11b.

The losses in the second part of the neutraliser are higher for the pulse with the deflection magnet turned on. The reason for this could be that the trajectories of ions in the neutraliser are already affected by the magnetic field of the deflection magnet and hit the neutraliser walls.

As expected, for pulses without deflection, within the error margins, no energy is found in the cooling water of the dumps. Additionally, as expected from the results of the gas scan, the low gas flow rate in the neutraliser of 15 mbar l/s caused higher losses in the neutraliser, which could be explained by space charge expansion of the ion beam. Thus, the total box losses are, with 15 % and 18 %, higher than the 13 % for typical pulses with 43 mbar l/s. And last but not least, the neutralisation efficiency is, with 56 %, higher than for pulses with higher acceleration voltages and higher gas flow rates in the neutraliser, as expected (cf. Sec. 2.1.1).

4.1.4 *Calorimetry in Duct and Beam Dump*

This section presents the results of the analysis of various NBI in-vessel pulses. The calorimetry of the vessel components is tested first with an NBI pulse into the empty vessel and compared to Beamlet Based NBI simulations [42]. The calorimetrically measured energies at all vessel components match the simulated ones within the error margins. This is followed by the analysis of in-vessel pulses with plasma and a consistency check with Fast-Ion D_α Simulation (FIDASIM) measurements [9, 10] using the charge exchange recombination spectroscopy (CXRS) diagnostic [11]. The NBI power offered to the plasma is about 3 MW. The absorption is calculated to be about 90 %.

NBI Into Empty Vessel in Comparison With Modelled Beam

Some NBI pulses into the vessel were done without W7-X plasma. One of these experiments from the 17.09.2018 is analysed in this section. First, the calorimetrically measured energies at the vessel components are compared to the heat loads calculated with a model of the NBI beam by [42]. Second, it is compared to a commissioning pulse from the 18.09.2018. Both result in the validation of the calorimetry of the vessel components. This is important for the error estimates of the measured duct losses and of the heat load by the non absorbed neutrals on the beam dump for plasma experiments. Both experiments are performed with S7 and with roughly 54 kV of acceleration voltage leading to an electric beam power of 5 MW. In order not to overload the ion dumps, with 0.39 s the duration of the empty vessel experiment is much shorter than a typical pulse. The standard gas setting was used for both pulses, but the source gas flow rate for the commissioning pulse was set to 21 mbar l/s. In Tab. 4.5 the data of the two experiments are listed.

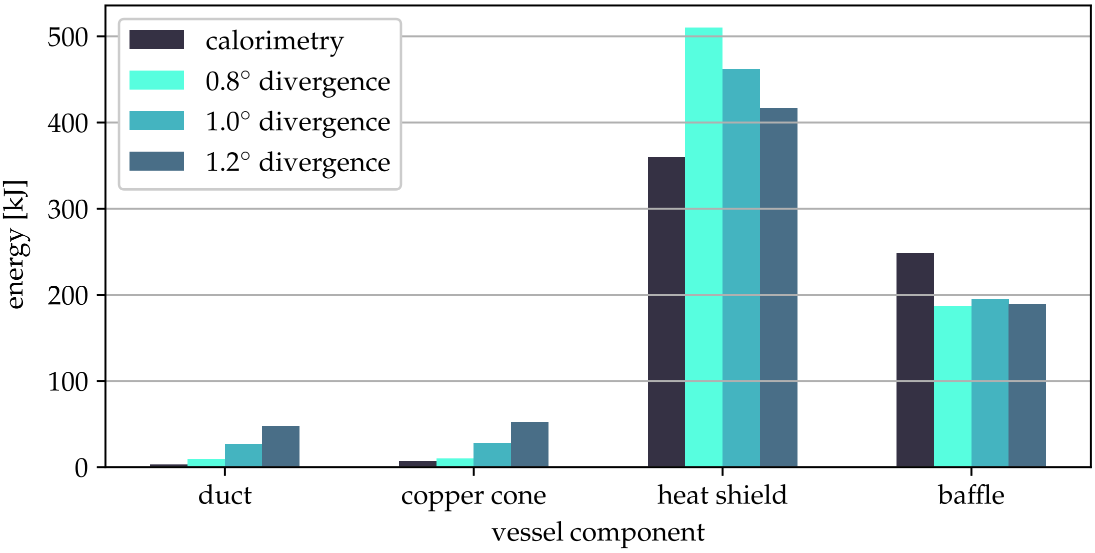

Figure 4.12: Comparison of modelled and measured energies for the vessel components for 20180917.002. The estimated energies on the vessel components by [42] are shown for different beamlet divergences.

Äkäslompolo et al. [42] applied the Beamlet Based NBI to the NBI system of W7-X and calculated the heat load at the vessel components for different degrees of beamlet divergence. The Beamlet Based NBI (BBNBI) code simulates ion ensembles from the NBI source with a Monte Carlo method. The measured acceleration voltage and extracted current of the ion beam are used in combination with the geometry of the grid apertures to model each beamlet separately. The ion ensembles are transformed to neutral ensembles with the neutralisation efficiency, which is calculated with spectroscopic data from the neutraliser. Finally the heat load on the vessel components is determined by the number and energy of particles hitting the surface of the components. In Fig. 4.12 the estimated energies on the vessel components is shown in comparison to the calorimetrically measured ones. The estimated energies are simulated with BBNBI using a neutralisation efficiency of 41 % and an initial power of 5 MW generated by S7 as input.

The calorimetrically measured energies at the vessel components fit approximately the simulated ones, but cannot give significant information about the divergence due to the uncertainty. The calorimetrically measured energies at heat shield and baffle imply that more of the beam of S7 ends at the baffle and less at the heat shield than expected from the simulation. But again, further investigation is required for any conclusion, because the observed discrepancy is within the error margins of the calorimetry at the vessel components. As explained in the sections 3.2.3 and 4.1.1, the measurement method for the vessel components is not optimal. The temperature signals have signal to noise ratios of less than ten. Therefore, the measurement error is higher for the duct and vessel components than for the components inside of the NBI box. This will be discussed in Sec. 4.3 *Error Estimation*.

Table 4.5: One NBI in-vessel pulse without plasma compared to a commissioning pulse. Both pulses were performed with S7. Source parameters are listed in the first part and calorimetrically measured energy and energy fractions of the components in the second part of the table. *Box losses* is the sum of the energy fractions of RF source, plasma grid and the second part of the neutraliser. The energy at the calorimeter for the in-vessel pulse is expected to be due to the deflection process (*, cf. Sec. above).

PARAMETER	VALUES FOR THE TWO PULSES			
Pulse ID	20180918n0924		20180917.002	
Pulse Type	commissioning		in-vessel	
Beam Time [s]	1.64		0.39	
Acc. Voltage [kV]	54.1		54.0	
Ext. Current [A]	90.8		92.2	
El. Power [MW]	4.9		5.0	
El. Energy [MJ]	8.1		1.9	
COMPONENT	[MJ]	[%]	[MJ]	[%]
RF Source	0.4	4.8	0.2	11.8
Plasma Grid	0.2	2.0	0.1	5.7
Neutraliser 2	0.5	5.8	0.2	7.8
Box Losses	1.0	12.6	0.5	25.3
H_2^+ Dump	0.2	2.2	0.1	2.5
H^+ Dump	2.1	26.3	0.6	29.5
Calorimeter	3.3	39.2	*0.0	*0.1
Box Exit Scraper			0.0	0.4
Copper Cone			0.0	0.4
Duct Liner			0.0	0.2
Heat Shield			0.4	18.5
Baffle			0.3	12.8
Measured Total	6.5	80.3	1.7	89.7

The comparison of the in-vessel pulse 20180917n1322 with the commissioning pulse 20180918n0924 shows that the sum of the energy fractions of the box exit scraper and the vessel components is less than the energy fraction of the calorimeter. 39 % of the electric beam energy is found on the calorimeter for experiment 20180918n0924. All together, 32 % of the electric beam energy of the in-vessel experiment without plasma is found on the vessel components. Note that the box losses are with 25.3 % twice as high for the in-vessel pulse as for the commissioning pulse with only 12.6 %. Typical box losses are about 13 %. The energy fractions of plasma grid and RF source contribute the most to the higher box losses. The build up of the cold plasma in the source could cause high losses at source and grids in the beginning of a pulse. This could lead to higher energy fractions due to the short beam time. The additional box losses of the in-vessel pulse of 12.7 % could be evidence of a lower beam power coming out of the neutraliser. Moreover, since the energy measured on the vessel components is lower than for the simulations, the beam energy is considered to be lower than expected. But the total measured energy fraction for the in-vessel pulse is also 9 % higher than for the commissioning pulse. Unlike the in-vessel pulse, the commissioning pulse was performed with the magnetic field of W7-X. Since the injector is not perfectly shielded against the magnetic field of W7-X, the field might have deflected some ions in the injector box onto components that are not cooled with water or the field might have influenced the measurement or performance of the NBI system in other ways. The influence of the magnetic field of W7-X on the RF source performance is analysed and discussed in Sec. 4.2.

All in all, the cause of the higher energy fraction in total for the in-vessel pulse and the lower energy fractions for the vessel components compared to the calorimeter energy fraction is not resolved, yet. The analysis of the two pulses shows, that the in-vessel and the commissioning pulses that are compared should have been performed with the same beam time to be able to draw more precise conclusions.

For the calculation of the injected beam power this means, that it is only reasonable to take the energy fraction of the calorimeter of a commissioning pulse and subtract the duct losses, if the box losses of the commissioning and the in-vessel pulses are similar. Otherwise, the box losses need to be taken into account in addition to the energy fraction of the calorimeter to calculate the injected beam power.

NBI Into W7-X Plasma in Comparison With Beam Emission Spectroscopy

The injected neutral beam power and the amount absorbed and thereby heating the plasma are the topic of this section. The calorimetrically derived injected power P_{inj} and shine through of the beams are compared with those inferred from beam emission spectroscopy analysed with Fast-Ion D_α Simulation (FIDASIM) by Poloskei et al. [9, 10]. First, the FIDASIM evaluation method is shortly described, followed by the comparison of both measurements.

FIDASIM is a Monte-Carlo based forward modelling code that predicts the Balmer-alpha emission of neutral hydrogen (H, D, T) with Doppler shifts according to their kinetic energy for tokamaks [43–45]. The adaption to the stellarator W7-X was first done by [9] in 2019. The simulations for W7-X take the geometry of the diagnostic [11] and NBI systems into account. The neutral beam particles are followed from the sources to the plasma, simulating the beam plasma interaction. FIDASIM predicts beam emission from excitation and fast-ion birth from ionisation and charge exchange. This allows to derive the beam absorption and the shine through. The input data needed are the particle fractions of the

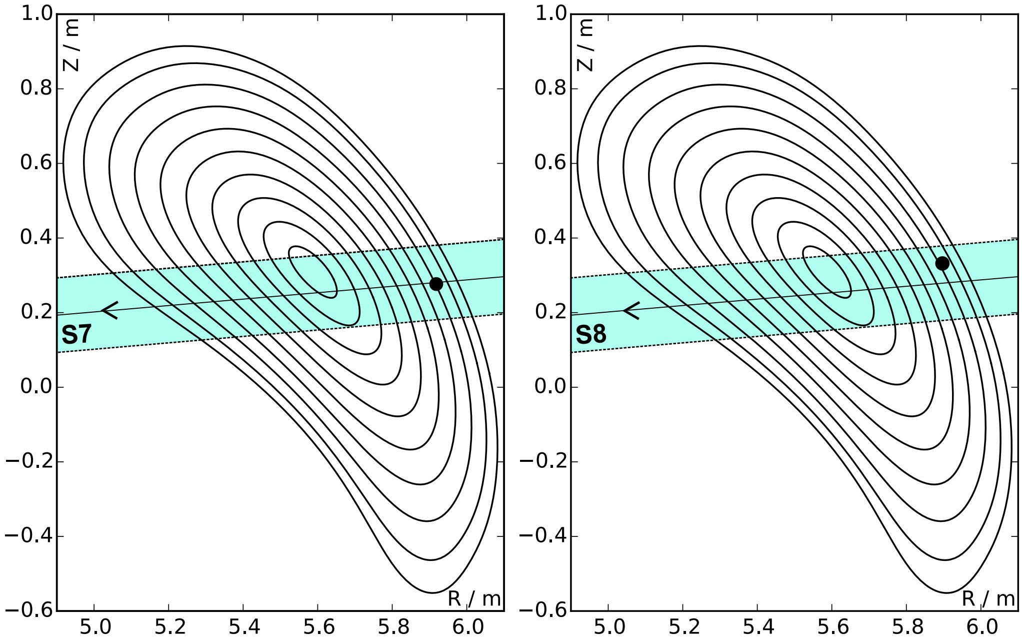

Figure 4.13: Poloidal cut through the plasma interaction volume with the injected beams of (left) S7 and (right) S8 (Figure adapted from [11]). The effective observation point of the used diagnostic port (AEM21:S7-12), is marked with a black dot (not to scale). It is at the centre of the S7 beam and at the edge of the S8 beam.

neutral beam ($H(E_0)$, $H(\frac{1}{2}E_0)$, $H(\frac{1}{3}E_0)$), the magnetic field, and the plasma parameters: the electron and ion temperature profiles and the electron density profile.

Moreover, beam emission spectra can be predicted for any (hypothetical) injected NBI power. If the beam emission spectra is also measured, the injected power can be determined. Starting with simulated spectra for a rough estimate of the injected power, the simulated spectra are adapted to the measured ones by varying the input injected power for the simulation. The processes related to the analysed beam emission are shortly described in Sec. 2.1.2. The Balmer-alpha emission from injected fast neutrals provides information on the injected neutral density and therefore neutral power in the detection volume. The analysis and adaptation of the complex spectrum can be done iteratively with the forward modelling routine FIDASIM.

For the two pulses discussed here, the beam emission spectra used for the forward modelling iteration were measured using the observation port AEM21:S7-12, marked in Fig. 4.13 (not to scale). The intensity calibration error is 10 %. The total error of the FIDASIM results is currently estimated to be 20 %. This is due to the uncertainties about the parameters at the plasma edge, due to the errors of the input parameters, mostly n_e, and due to errors in the beam geometry, mainly the beam divergence. Assuming primarily carbon impurities, the effective charge of the plasma is set to $Z_{eff} = 1.5$. The electron temperature and density profiles, measured via Thomson scattering, are shown with the ion temperature, measured with Charge Exchange Recombination Spectroscopy, in Fig. 4.14. The profiles are only valid for the plasma within the last closed flux surface. They are not determined outside of the last closed flux surface of the plasma. Therefore, two simulations were done, one with no particles in the edge region (*no edge*) and one with constant plasma parameters equal to those at the last closed flux surface (*edge*)

Table 4.6: Comparison of BES-FIDASIM and calorimetry results of 20180823.037 and 20181009.016. The input to FIDASIM is listed in the top part of the table. The results are presented in the bottom part. The measurement time is given in relation to the beginning of the plasma discharge of W7-X ($t_0 = 0$). With FIDASIM the injected power of the neutral beam for a single time point is determined. With calorimetry the averaged injected power of the whole pulse is calculated.

INPUT TO FIDASIM

PARAMETER	INPUT VALUE	INPUT VALUE	
Time	$t_1 = 5.25\,\mathrm{s}$	$t_1 = 2.15\,\mathrm{s}$	$t_2 = 4.85\,\mathrm{s}$
Particle Fraction $H(E_0)$ [%]	32	30	30
Particle Fraction $H(\frac{1}{2}E_0)$ [%]	61	50	50
Particle Fraction $H(\frac{1}{3}E_0)$ [%]	7	20	20

RESULTS

Pulse ID		20180823.037			20181009.016		
PARAMETER	TIME	CALOR.	FIDASIM		CALOR.	FIDASIM	
			no edge	edge		no edge	edge
Injected Power [MW]		2.7	2.5	2.8	3.1	3.1	3.4
Shine Through [%]	t_1	10.7	12.2	10.7	6.8	11.9	10.8
Shine Through [%]	t_2				6.8	6.1	5.6

for an additional 5 cm. This results in upper and lower boundaries for the injected neutral power and shine through estimates. To determine the injected power, 500 000 Monte-Carlo markers were used per source and measurement. In the iteration process only the injected power was varied to fit the predicted spectra to the measured ones. To simulate the absorption and thus calculate the shine through, 4000 Monte-Carlo markers were used.

From the calorimetric measurements, the injected and the absorbed power are determined as follows: the duct losses of an in-vessel pulse are subtracted from the energy on the calorimeter from a similar NBI commissioning pulse to obtain an estimate of the energy of the neutral beam injected into the W7-X plasma. Additional subtraction of the energy found on the beam dump leads to the amount of beam energy ionised in the plasma. The ratio of the energy found on the beam dump to the injected energy is the shine through. The error in the calorimetrically determined injected power is about $\sigma_{P_{inj}} = 25\,\%$ (cf. 4.3.3). The injected power and the shine through are measured with calorimetry and FIDASIM for the two pulses 20180823.037 with $U = 47\,\mathrm{kV}$ and 20181009.016 with $U = 53\,\mathrm{kV}$. For 20180823.037, an electric beam power of both sources combined of $P_{el} = 7.5\,\mathrm{MW}$ was generated, for 20181009.016, $P_{el} = 9.4\,\mathrm{MW}$. The results are compared in Tab. 4.6. The calorimetry data of pulse 20180823.037 are listed in Tab. b.1 in the Appendix. The calorimetry data relating to pulse 20181009.016 are listed in Tab. 4.1 in Sec. 4.1.2. Note that with FIDASIM the momentarily injected power of the neutral beam is determined, whereas with calorimetry the averaged injected power of the whole

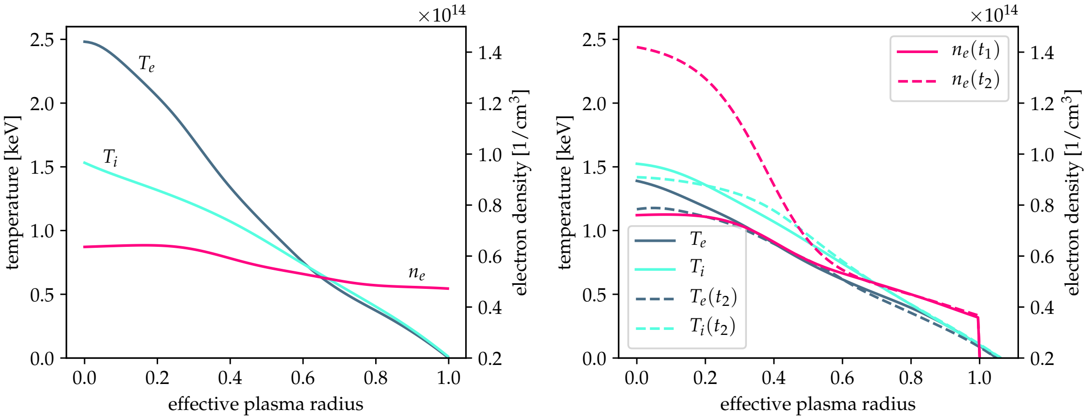

(a) 20180823.037

(b) 20181009.016

Figure 4.14: Profiles of T_e, T_i, and n_e (a) in the middle of the NBI heating phase of 20180823.037 and (b) in the beginning (t_1) and in the end (t_2) of the NBI heating phase of 20181009.016. The electron density n_e is peaking in the plasma core in 20181009.016 causing higher absorption of the neutral beam by the plasma.

pulse is calculated. The measurement time t_i is given in relation to the beginning of the plasma discharge of W7-X ($t_0 = 0$). The NBI operation of pulse 20180823.037 starts at $t = 4.5$ s and lasts $t_{NBI} = 1.2$ s. The FIDASIM measurements are performed for $t_1 = 5.25$ s. The NBI operation of pulse 20181009.016 starts at $t = 1.0$ s and lasts $t_{NBI} = 4.0$ s. Here, the evaluation with FIDASIM is done at the beginning $t_1 = 2.15$ s and also at the end $t_2 = 4.85$ s of the NBI heating phase, because the fuelling and heating of the plasma with NBI changes the plasma parameters, as can be seen in Fig. 4.14b. The rise in the electron density in the plasma core is expected to cause a drop in shine through by the end of the pulse.

The calorimetrically determined injected neutral power matches the FIDASIM measurements for both pulses within the errors. According to the calorimetry results, 33.2 % of the electric beam power is injected into the plasma for the $U = 54$ kV pulse 20181009.016. For the $U = 47$ kV pulse 20180823.037 36.0 % of the electric beam power is injected into the plasma. As expected, the conversion efficiency is higher for the pulse with lower acceleration voltage, due to the higher neutralisation efficiency (cf. Sec. 2.1.1 *Neutralisation*). The two shine through measurements are also in agreement. The variation of the results with and without absorption in the plasma edge region is within the error margins and thus no conclusions on the plasma edge can be drawn.

All in all, about 3 MW of NBI power is injected into the plasma and about 90 % of it is ionised there for parameters shown in Fig. 4.14.

4.2 INFLUENCE OF THE MAGNETIC STRAY FIELD OF W7-X ON THE EXTRACTED CURRENT

The magnetic stray field of W7-X might have an influence on the performance of the NBI sources. Thus, different magnetic configurations may cause different performances of the NBI sources. The better the performance of the RF sources, the less RF power P_{RF}, which is used to operate the RF ion sources, is needed to extract high currents I_{ext}. Therefore,

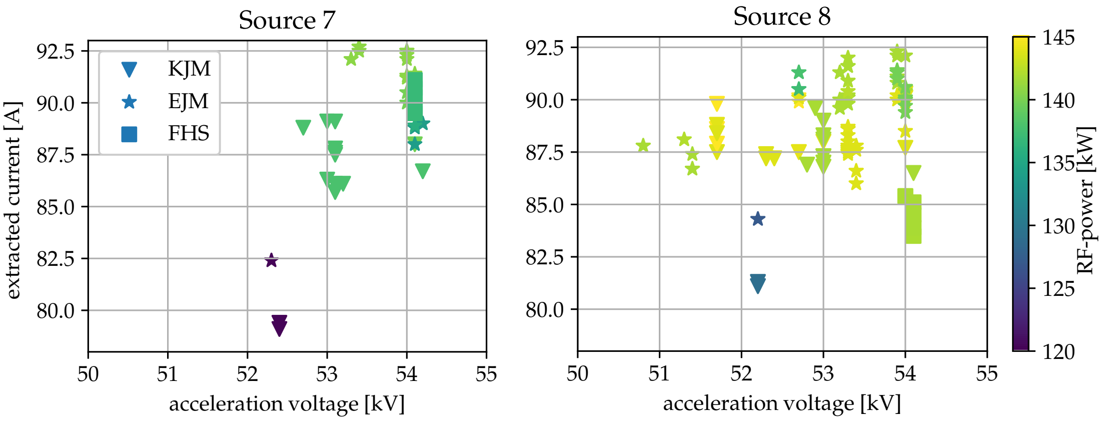

Figure 4.15: Influence of the magnetic stray field of W7-X on the extracted current for acceleration voltages in the range of 50 kV to 55 kV and RF source power in the range of 120 kW to 145 kW. Pulses with S7 are shown in the left graph. Pulses with S8 are presented in the right graph. A different shaped marker is used for each of the three types of analysed stray fields of W7-X. The colour of the marker represents the used RF power at the ion source. The better the performance of the RF sources, the less RF power is needed to extract high currents and the darker the colour of the marker at high extracted currents.

the RF power leading to the extraction of a certain beam current for a given acceleration voltage U is studied for different magnetic configurations. Firstly, the influence of stray fields from three different magnetic configurations with magnetic field strengths of more than 2 T in the centre of the W7-X plasma region are compared. The three magnetic configurations with the highest number of NBI pulses (number in brackets) were chosen: EJM configuration (69), KJM (27) and FTM (10). Secondly, the influence of the magnetic field generated by the trim coil, which is installed between the two NBI boxes (cf. Sec. 3.3), is investigated.

All successful NBI pulses with a source gas flow rate of 18 mbar l/s and acceleration voltages close to the typical value of 54 kV during the last month of W7-X operation phase 1.2b are analysed. The main commissioning of the NBI system was finished by then.

The analysed pulses are depicted in the Figures 4.15 and 4.16. Pulses with S7 are shown in the left graphs and pulses with S8 in the right graphs of the figures. The types of magnetic stray field, EJM, KJM and FHS in Fig. 4.15 and the operation of the trim coil in Fig. 4.16, are distinguished by shaped markers. The colour of the marker represents the used RF power at the source, according to the colourbar. As stated before, one speaks of a good ion source performance, if a high current can be extracted at low RF power. In Figures 4.15 and 4.16 these are dark coloured markers at high extraction currents.

Figure 4.15 shows the extracted current versus the acceleration voltage with the used RF power for the three high field configurations KJM, EJM, and FHS. At first, the results with operation of S7 are presented. This is followed by the discussion of the results with operation of S8.

Some S7 pulses show better performances with FHS than with EJM and KJM configuration and also better performances with EJM than with KJM configuration. At $U \approx 54$ kV better source performance with FHS in comparison to EJM and KJM is observed. With $P_{RF} \approx 137$ kW and FHS configuration up to 91 A can be extracted. With KJM config-

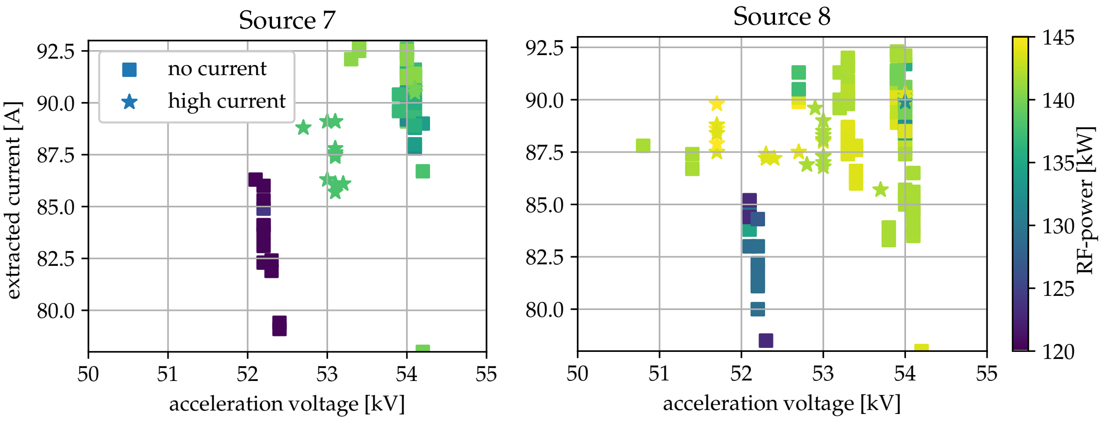

Figure 4.16: Influence of the magnetic stray field of the W7-X trim coil, which is located between the two injectors, on the extracted current for acceleration voltages in the range of 50 kV to 55 kV and RF source power in the range of 120 kW to 145 kW. Pulses with S7 are shown in the left graph. Pulses with S8 are presented in the right graph. A square is used as marker for pulses without operation of the trim coil, when there was *no current* in the coil. A star is used as a marker for the pulses with operation of the trim coil, when there was a *high current* in the trim coil. The colour of the marker represents the used RF power at the ion source. The better the performance of the RF sources, the less RF power is needed to extract high currents and the darker the colour of the marker at high extracted currents.

uration only 87 A are extracted with the same RF power. This is a change of about 5 %. With EJM configuration the same current can be extracted but higher RF power of about 141 kW is needed. Better source performance with EJM in comparison to KJM is observed at $U \approx 52$ kV and 54 kV. At $U \approx 52$ kV with about 120 kW RF power and EJM configuration more than 82 A can be extracted. With KJM configuration less than 80 A are extracted. At $U \approx 54$ kV about 140 kW is needed to extract 88 A with KJM but only about 134 kW with EJM.

But it is also observed, that with the same RF power and the same acceleration voltage the extracted current varies in the range of up to 3.7 A within pulses of one configuration. This can be seen at $U \approx 53$ kV for KJM configuration and at $U \approx 54$ kV for FHS and EJM configuration. That means, that the variations within pulses of one configuration are in the same range as the variations between pulses of different configurations. Therefore, the observed variations between pulses of different configurations are within the error margins.

A similar source performance is observed for S8: some pulses show better performances with EJM than with KJM configuration. But also the opposite is observed. At acceleration voltages of roughly 52 kV and about 128 kW RF power more than 84 A can be extracted with EJM configuration stray field. Less than 82 A are extracted with KJM configuration. But at $U \approx 53$ kV better source performance with KJM in comparison to EJM is observed. With about 144 kW of RF power and EJM configuration about 90 A can be extracted. With KJM configuration about 141 kW of RF power is needed to extract the same current. Thus, the influence of EJM and KJM stray fields on S8 is not clear.

Additionally, some pulses show better performances with EJM than with FHS configuration. At 54 kV the extracted current varies form 84 A with FHS to 92 A with EJM for pulses with a source power of about 142 kW. This is a change of up to 9 %.

Even higher variations in the extracted current of S8 can be observed in comparison to S7 for pulses with the same RF power, acceleration voltage for the three magnetic configurations. At 54 kV with a source power of about 142 kW the extracted current varies form 84 A with FHS to 92 A with EJM. This is a change of up to 11 % of the extracted current. Moreover, with the same magnetic configuration and acceleration voltage different source power is used to extract the same current with S8: at $U = 52.7\,\text{kV}$ some pulses with EJM stray field needed 136 kW of source power and some 145 kW to extract $I_{ext} \approx 90\,\text{A}$. This is a variation in the source power of 6 %. That means, as for S7, that the variations between pulses of different configurations are in the same range as the variations within pulses of one configuration.

The influence of the stray field of the trim coil on the extraction current for different acceleration voltages and RF power is shown in Fig. 4.16. No dependence of the source performances on the trim coil operation was observed. The results without operation of the trim coil are presented first. This is followed by the discussion of the results with operation of the trim coil.

Without operating the trim coil the extracted current varies in the range of up to 9 A for the same acceleration voltage and RF source power. This can be seen best at $U \approx 52\,\text{kV}$ for pulses with $P_{RF} \approx 120\,\text{kW}$ for S7 and at $U \approx 54\,\text{kV}$ for pulses with $P_{RF} \approx 142\,\text{kW}$ for S8. Also the needed RF source power to extract the same current with the same acceleration voltage varies. This variation in the RF power is up to 10 kW for S7 with $U \approx 54\,\text{kV}$. For S8 the variation is in the range of up to 12 kW at $U \approx 52\,\text{kV}$, 53 kV, and 54 kV. This is about 7 % to 8 % of 145 kW.

The performance of the RF sources is similar with and without operation of the trim coil. Approximately 90 A can be extracted, regardless whether the trim coil is operated, using the same RF source power with $U \approx 54\,\text{kV}$. This is observed for both sources. Moreover, most of the analysed pulses show that S7 needs less RF source power than S8. This is independent of the stray field configuration and the trim coil operation.

To conclude, within the error margins, no clear dependence of the source performances on the three different stray fields KJM, EJM, FHS or on the trim coil operation was observed for both sources. But, independent of the stray field, the performance of S7 was better than that of S8. The cause is not clear.

4.3 ERROR ESTIMATION

The errors to be considered for the stray field analysis are the measurement errors of the acceleration voltage, $\Delta U = 2.0\,\text{kV}$, and the extracted current, $\Delta I_{ext} = 1.5\,\text{A}$, [46]. The error estimation of the calorimetric measurements requires consideration of many additional sources of error, due to the complexity of the NBI system. It is the main topic of this Section.

The measurement method and the error sources are depicted in Fig. 4.17. The schematic shows a component that is cooled with water. The energy of the beam particles transferred to the component is mainly conducted to the water. Therefore, the temperature of the cooling water rises. The rise in temperature ΔT and the flow rate $\dot{V}$ of the water are measured with sensors in the water. The energy in the cooling water is derived from

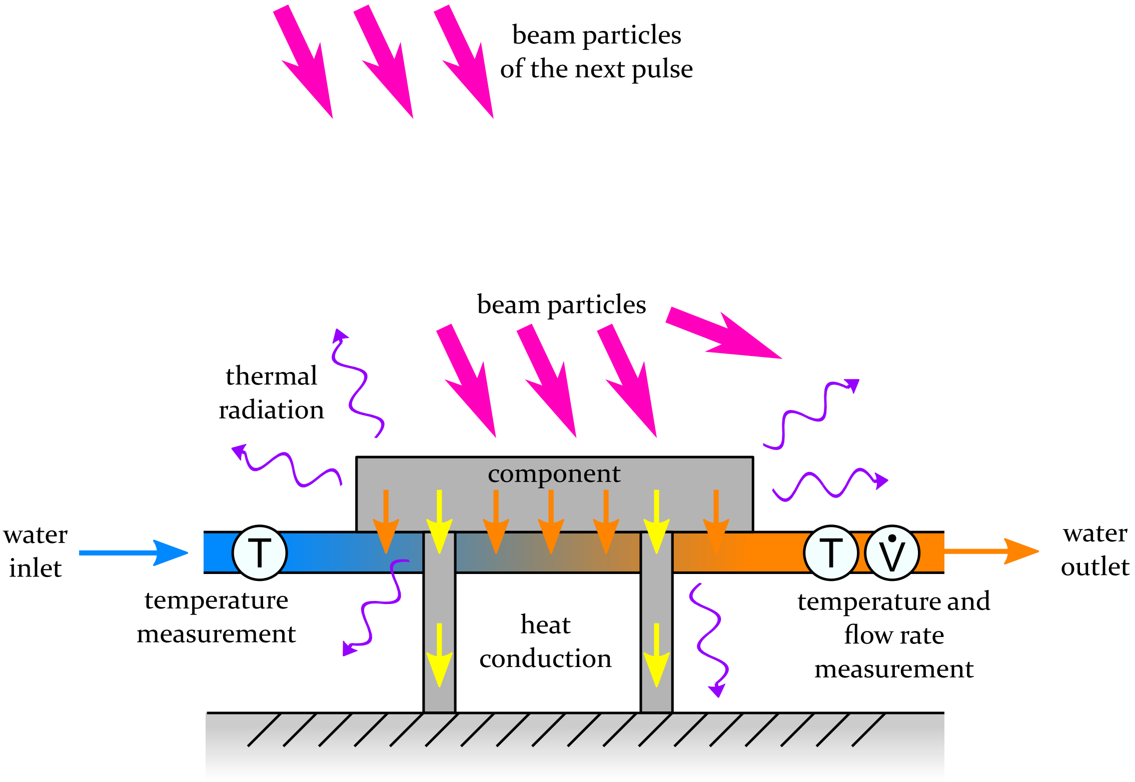

Figure 4.17: Schematic of the energy flow for a water cooled NBI component with possible energy losses and measurement errors. Pink arrows represent energetic beam particles. The beam particles transfer their energy to the water cooled component, shown as grey rectangle connected to a pipe, if they strike it. The thermal energy of the component is partially radiated (purple arrows), partially conducted to the support frame (yellow arrows) and mainly conducted to the water (orange arrows). Therefore, the temperature of the water which flows through the pipe rises. Thus, the temperature of the outlet (orange) is higher than that of the inlet (blue). The rise in temperature ΔT and the flow rate $\dot{V}$ of the water are measured with sensors in the water.

the measured quantities, $\dot{V}$ and ΔT, the flexible integration limits t_0 and t_1 and the two factors ρ and c:

$$E = c\rho \int_{t_0}^{t_1} \dot{V} \Delta T dt. \tag{4.6}$$

The energy in the cooling water equals the energy that was transferred to the component by the beam particles in the case of an isolated system with infinite integration time. Here, the system is not isolated and the *integration time is limited* due to the pulsed operation. Two types of energy losses that therefore must be considered for calorimetry were already introduced in Sec. 2.2: *thermal radiation* and *heat conduction* to the support frame. *Additional heat loads on the vessel components due to plasma operation in the W7-X vessel* add to the heat loads caused by the beam particles. Moreover, heat loads on certain components could not be measured due to *defect sensors*. *Measurement uncertainties* of the sensors and *disturbances* of the signals are additional error sources. The *measured flow rates include bypasses* to components of sources 5 and 6 (S5 and S6). The error due to *noise* *on the temperature signal of the duct and beam dump components* is estimated. In addition, the error caused by *fluctuations in the temperature of the cooling water* is studied. The ions are deflected onto the dumps by the *deflection* magnet, but partially also past the dumps. As a result, some of the ions do not land on water-cooled components and are therefore not accounted for. These sources of error are grouped to *systematic errors* and *statistic errors*. There is a titled paragraph for each error source. The parameters of the formula affected by the error are marked by a symbol at the end of the title. The results of the error analysis are concluded in the end. The errors are summarized for each component and the error of the injected power is determined.

4.3.1 *Systematic Errors*

- DEFECT SENSORS – ΔT, $\dot{V}$
  The ground grids, deceleration grids, first parts of the neutralisers, and the magnet liners are cooled with water, but the temperature is not measured. The temperature sensors at the Ground and Deceleration Grids and Neutraliser Part 1 (GDGN) of S7 and S8 broke during the commissioning of NI21. The sensor for the S8 components broke last, it worked until 25.09.2018. For the commissioning pulse 20180924n1422, with a beam time of 5.16 s, an acceleration voltage of 54.0 kV and no arcs an energy fraction of 2.1 % was measured there. This value is taken as energy fraction of the GDGN for all pulses from then on. The temperature sensor of the cooling water of the *magnet liners* broke early in the commissioning phase. Therefore, no measurement data for typical NBI pulses is available. At the test stand of the NBI system at AUG it was measured to be 6 % of the electric beam energy for $U = 54\,\mathrm{kV}$ pulses [29]. This value is also taken for the NBI system at W7-X.

  The exact flow rate of the cooling water for the H^+ dumps and H_2^+ dumps in the magnet cannot be determined, due to a defect flowmeter. The piping and instrumentation diagram is shown in the Appendix Sec. a. Since the flowmeter of the H_2^+ dumps in the magnet was defect, the signal of the flowmeter measuring the flow rate of the mixed water from the H^+ dump and H_2^+ dump in the magnet is used instead. The signal is downscaled by factors according to the initial configuration of the high flow rate water cooling circuit from June 2017. Thus, the weighing of the flow rates for the two dumps cannot be distinguished. For this reason, there is a potential error of the individual flow rates and therefore energy in the cooling water of the H^+ dumps and H_2^+ dumps in the magnet.

- DEFLECTION PROCESS – E
  The losses due to the deflection process are discussed in Sec. 4.1.3 *Influence of the Deflection Magnet*. The losses in the analysed case correspond to an energy fraction of about 8 %. Further experiments are required to analyse this in detail.

- LIMITED INTEGRATION TIME – Δt
  Formally, the exact energy transferred from the beam to the components can only be completely found in the cooling water for infinitely long integration times. Here, the integration times are up to 11 min. Usually the next pulse starts right afterwards. Thus, not all energy transferred to the cooling water is detected. As a result, the total calculated energy in the cooling water will be underestimated. The error due to finite integration is considered negligible for actively cooled

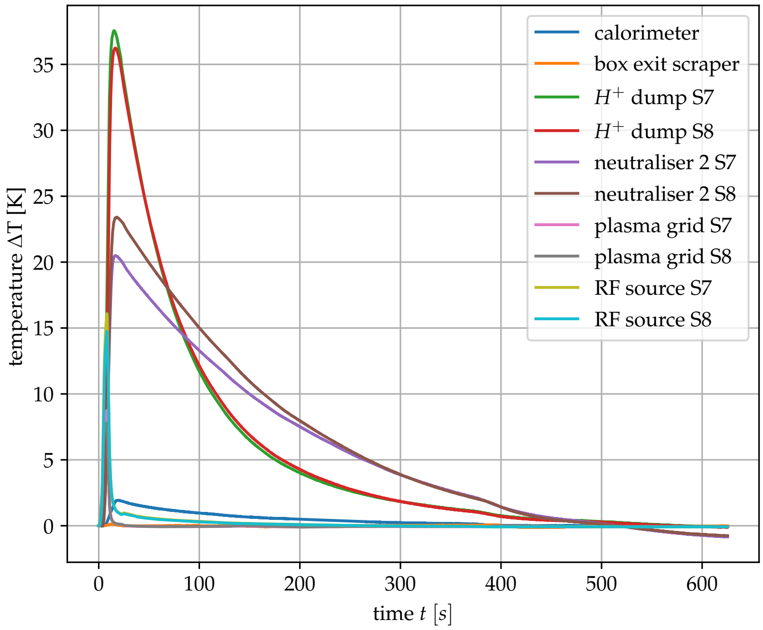

Figure 4.18: Cool down time of inertially cooled components of the injector box, exemplarily for the full power commissioning pulse 20181009n0718. The height and decrease of the temperature signal curve depend on the heat load density at the component and the flow rate of the cooling water. The second part of the neutralisers and the outer parts of the H^+ dumps take the longest to cool down, approximately 500 s.

components in general and for pulses with a pause afterwards, which allows the integration over 11 min for the inertially cooled components. The temperature of the outlet reaches the initial value with respect to the fluctuations in the inlet for all components within this time interval. But with decreasing integration time, the error increases. It depends on the total electric beam energy and the cooling of the component. In Fig. 4.18 the rise in temperature of the cooling water ΔT of the inertially cooled components of the injector box are shown for the full power 5.2 s commissioning pulse 20181009n0718. The highest errors due to finite integration time are expected for the second part of the neutralisers and the outer parts of the H^+ dumps, because the cool down time there is the longest. For all pulse data presented in this thesis, the error due to finite integration is considered negligible.

- THERMAL RADIATION – ΔT
  The thermal radiation of all hot surfaces of the analysed NBI components, that is absorbed by components that are not included in the calorimetric measurements, has to be considered as energy loss, because the system is not isolated. The highest heat load power densities occur at the actively cooled parts of the calorimeter and the H^+ dumps, the H_2^+ dumps and the beam dump. Components that can absorb the radiated energy and that are not included in the calorimetric measurements are the plasma vessel tiles apart from the beam dump, the walls of the NBI box and the support frames. The radiated energy loss was introduced in Sec. 2.2:

$$\frac{\partial E}{\partial t} = \varepsilon A \sigma (T^4 - T_0^4).$$

In the following, thermal radiation losses are estimated exemplarily for a typical 54 kV pulse (20181008n1257) for the actively cooled parts, the inertially cooled parts, the pipes surfaces and the beam dump. The surface temperature of the components that absorb this radiation is assumed to be $T_0 = 293\,\mathrm{K}$. Absorption by water cooled NBI components is neglected for a conservative estimate of the radiation losses.

All *actively cooled parts* of the H^+ dumps and the calorimeter add up to a surface of up to 1.2 m^2. The maximum allowable surface temperature of these copper tiles (emissivity $\varepsilon \approx 0.03$ [22, p. 951]) is 377 °C [31]. The temperature of the cooling water of the actively cooled parts reaches its initial value within 10 s. The total energy that is radiated of a 1.2 m^2 copper surface at 377 °C in 10 s is 3.5 kJ. Thus, the total radiation losses are less than 0.007 % of the electric beam energy (51 MJ). The thermal radiation of the water *pipes* between component and temperature sensors can also be neglected. The emissivity is larger, but the sensors are less than 5 cm behind each panel and the temperature of the water stays below 60 °C.

The conservative estimates for the hottest *inertially cooled parts* show that losses in the injector box due to thermal radiation can be neglected. The hottest calorimeter plates have a total surface (front, back and sides) of circa 0.15 m^2 per source. They are also made of copper. For 20181008n1257 their temperature rises to up to 115 °C, according to thermocouples on the backside. A cool down time of 10 min and a linear decay in temperature from the maximum to room temperature results in thermal radiation losses of less than 0.004 % of the electric beam energy. The other three plates per source of the calorimeter have temperatures of up to 61 °C, according to thermocouples on the backside, and similar surfaces. The hottest plates of the H^+ dumps are of copper as well and have a total surface of 0.32 m^2 per source. Here, thermocouples on the backside measured up to 371 °C for 20181009n1257. Estimated similarly to the calorimeter plates, the thermal radiation losses are less than 0.04 % of the electric beam energy. The other five plates per source of the H^+ dumps have temperatures of less than 82 °C according to thermocouples on the backside. Additionally, they have smaller surface areas.

The thermal radiation of the *pipes surfaces* between the inertially cooled components and the temperature sensors can also be neglected. The measured water temperature stays below 50 °C, for most components below 22 °C. The emissivity of polished stainless steel is about $\varepsilon = 0.13$ [47]. Even for a linear decrease from a maximum temperature of 50 °C over 10 min the surface area of all pipes between the components and the temperature sensors would have to be larger than 18 m^2 for thermal radiation losses of 0.1 %. But it is less than 5 m^2.

For a typical NBI pulse of about 50 MJ the relative thermal radiation losses σ_{TR} of the *beam dump* are up to 0.7 % energy fraction. Each tile of the beam dump has a plasma facing surface of roughly 0.01 m^2 made of carbon fibre composite ($\varepsilon \approx 0.95$ [22, p. 952]). The beam of one source covers about 26 tiles. The NBI is shut down in case of temperatures higher than 800 °C in order to prevent destruction of the beam dump. A conservative estimate of the thermal radiation losses is calculated with the maximum surface temperature for 5 s, corresponding to the typical beam time, followed by a linear cool down over 10 s. This leads to thermal radiation losses of up to $\Delta E_{TR} = 0.16\,\mathrm{MJ}$ per source.

- HEAT CONDUCTION – ΔT

  The energy transferred from the beam to the components can only be completely found in the cooling water for a perfectly isolated system. All components are attached with support frames to the injector box. But the support frames and the walls of the injector box are not connected to the water cooling system. For this reason, heat conduction to these parts has to be considered as energy loss. The measured and calculated energy in the cooling water is expected to be less than the energy load on the corresponding NBI components. As a result, the total calculated energy in the cooling water will be underestimated. The energy loss due to heat conduction is described as (cf. Sec. 2.2)

  $$\frac{\partial E}{\partial t} = -\lambda \frac{\partial T}{\partial x} A.$$

  The heat conduction through the support frames of inertially cooled components is estimated first, followed by that of the actively cooled components and the beam dump components.

  The heat conduction to the cooling water from the *inertially cooled components* through the 1 mm thick walls of the stainless steel pipes is compared to the heat conduction through the stainless steel support frames to the box as heat sink. The heat conduction differs in the distance Δx, the area A and sometimes in the heat conduction λ. The factor of these three parameters combined is larger than 100 for all inertially cooled components for the conduction to the cooling water compared to conduction to the walls of the box due to: (a) the larger distance to the heat sink for the support frames compared to the 1 mm distance for the pipes and (b) the smaller conduction area of the support frames compared to the conduction area of the soldered pipes. This results already in an energy loss due to heat conduction of less than 1 % of the energy transferred to the cooling water. The only exception are the top and bottom plates at the calorimeter. There, the energy loss due to heat conduction to the support frame is up to 3 % of the energy transferred to the panel. Considering a typical energy fraction of up to 3 % measured in the cooling water of all calorimeter plates, the energy loss to the support frame is less than a tenth of a percent of the electric beam energy and is therefore neglected.

  Since the cooling water is guided through the *actively cooled components*, the area for conduction to the water is much larger than the area for conduction to the support frame and no conduction through the wall of a pipe is necessary. Thus, the heat conduction losses are neglected here.

  At the components in the plasma vessel the losses due to heat conduction are also neglected. As depicted in Sec. 3.2.3 describing the water cooling system, the water which cools the *beam dump* area is also cooling the surrounding vessel area. Only 13 % of the heat shield module area and 33 % of the baffle module area is covered by the beams. Heat conduction works in both directions. The heat from the beam dump is transferred to the cooler water. Thus, downstream the heat of the water is also transferred to cooler parts of the heat shield and baffle modules. This could increase the losses to support frames. But these losses are expected to be negligible. Therefore, the heat conduction losses at the vessel components are considered negligible as well.

- WATER BYPASSES – $\dot{V}$
  The pipes for the components of the not yet installed S5 and S6 were already connected to the cooling circuits. However, the pipes were modified so that only a very small amount of water passes through them. These pipes are called bypasses. This water flow is considered negligible and not included in the calorimetric calculations. There are bypasses for the inertially and actively cooled parts of the H^+ dumps and all inertially cooled components in the injector box except for the calorimeter and the box exit scraper for S5 and S6.

- TEMPERATURE RISE DUE TO W7-X PLASMA OPERATION – ΔT
  The heat caused by the plasma operation of W7-X is transferred to the same cooling water and therefore contributes to the temperature course of the cooling water of the vessel components. The systematic error due to plasma operation is calculated in combination with the statistic error due to noise of the vessel temperature signals (see next section).

4.3.2 *Statistic Errors*

- ELECTRIC BEAM ENERGY
  The errors of the electric beam energy $E = UI_{ext}t_{NBI}$ and power $P = UI_{ext}$ are $\Delta E \leq \pm 1.3\,\mathrm{MJ}$ and $\Delta P \leq \pm 0.6\,\mathrm{MW}$ per source, which is σ_E and $\sigma_P \leq \pm 6\,\%$, for typical NBI pulses with $U = 54.0\,\mathrm{kV}$ and $I_{ext} = 90.0\,\mathrm{A}$ for $t_{NBI} = 5.00\,\mathrm{s}$, calculated with propagation rules for error margins (cf. Eq. 4.11, 4.12, 4.14, 4.15). This error is dominated by the errors of the supplied acceleration voltage $\sigma_U \leq 2.0\,\mathrm{kV}$ and the extracted current $\sigma_{I_{ext}} \leq 1.5\,\mathrm{A}$ [46].

- MEASUREMENT UNCERTAINTIES OF FLOW RATE AND TEMPERATURE – ΔT, $\dot{V}$
  Thermocouples, PT100s and flowmeters are used to measure temperature and flow rate of the cooling water of the NBI components. The temperature sensors are installed at the pipes with the measuring tips in contact with the cooling water. In the vessel cooling circuit the flowmeters also measure the temperature. The

Table 4.7: List of the installed sensor types for temperature and flow rate measurement. Here, ΔT is the absolute error in the temperature measurement and not the rise in temperature.

SENSOR	TYPE	COMPANY	UNCERTAINTY
INJECTOR BOX			
Thermocouple	K (NICr-NI)	TC Mess- und Regelungstechnik GmbH	$\Delta T = \pm 1.5\,\mathrm{K}$
PT100	MWT509	SAB Bröckskes	$\Delta T = \pm 0.35\,\mathrm{K}$
Flowmeter	FS4000-ST4	ABB	$\sigma_{\dot{V}} = \pm 0.8\,\%$
DUCT AND BEAM DUMP			
Flowmeter	Prowirl 73W/D200	Endress+Hauser	$\sigma_{\dot{V}} = \pm 5\,\%$ $\Delta T = \pm 1\,\mathrm{K}$

various sensors are listed with their measurement uncertainties specified by the manufacturer in Tab. 4.7. The observed noise levels in the temperature signals are less than those specified by the manufacturer. The temperature signals of the actively cooled components vary in the range of up to $\Delta(\Delta T) = \pm 0.02\,\mathrm{K}$. The temperature signals of all other components of the injector box vary in the range of up to $\Delta T = \pm 0.01\,\mathrm{K}$. The error of the rise in temperature is $\Delta(\Delta T) = \pm 0.02\,\mathrm{K}$, since the rise in temperature ΔT of the inertially cooled components consists of the inlet and the outlet temperature. The observed variation in the temperature signals of the vessel components is discussed in the next paragraph.

- NOISE OF VESSEL TEMPERATURE SIGNALS – ΔT
  The temperature measurements of the cooling water of the vessel cooling circuit show signal to noise ratios of less than 10. Additionally, heat caused by the plasma operation is transferred to the same cooling water and therefore contributes to the temperature evolution. Calculation of the energy in the cooling water of the duct and beam dump components with W7-X operation but without NBI is done to estimate the statistic error due to noise in combination with the systematic error due to plasma operation, ΔE_{NP}. The calculation is performed the same way as for the NBI pulse analysis. The integration time interval is moved stepwise in a 40 min time slot of operation day 10.10.2018 beginning at 08:35 UTC. This way, 990 integrations per component are used for the error estimation. The results are listed in Tab. 4.8. The difference between the signals, and thus the calculated energy, can be negative, due to the noise of the inlet and outlet temperature signals. The error in the measured energy in the cooling water is ±60 kJ for the copper cone, ±160 kJ for the duct liner, ±250 kJ for the heat shield and ±230 kJ for the baffle. The energy fractions of a typical full power NBI pulse with both sources (50 MJ) are ±0.2 % for the copper cone, ±0.4 % for the duct liner, ±0.5 % for the heat shield and ±0.5 % for the baffle. Therefore, the error on the injected power is ±0.5 % of the electric beam power.

Table 4.8: Error in the calorimetrically measured energy at the vessel components due to noise of the water temperature signals and due to plasma operation. The error is given as percentage of 50 MJ as the typical electric beam energy of a full power NBI pulse with both sources.

COMPONENT	E_{min} [kJ]	E_{max} [kJ]	ΔE_{NP} [kJ]	FRACTION OF 50 MJ [%]
Copper Cone	-52	39	±60	±0.2
Duct Liner	-139	153	±160	±0.4
Heat Shield	-249	203	±250	±0.5
Baffle	-230	103	±230	±0.5
Sum			±700	±1.4

- FLUCTUATIONS IN THE WATER TEMPERATURE – ΔT
  The cooling water is flowing in circuits. Therefore, the inlet temperature is not constant, but varies by about ± 1.0 K. Only the rise in temperature ΔT is important for calorimetry. It is calculated from two temperature measurements, one at the inlet and one at the outlet. There is an offset in temperature and time. The latter one is due to the distance between the sensors and the velocity of the water. These offsets and the correction is described in Sec. 4.1.1 in detail. However, the fluctuations do not completely vanish when subtracting the measured inlet from the outlet temperature signal. A dispersion of the inlet temperature signal is observed when studying the outlet temperature signal. Thus, after subtraction, the resulting signal still varies by up to ± 0.1 K. This is expected to be due to the convective heat transfer [22] and turbulence on the way through the pipes. The velocity and temperature at the walls of the pipes are different from those at the centre. One speaks of boundary layers. At the bends and junctions of the pipes, the slower edge water is mixed with the fast water from the centre. Therefore, also the time dependent information of the temperature is mixed. This depends on the velocity gradient. With infinite integration time this would not affect the measurement. However, with finite integration time additional heat can be measured at the beginning and at the end of the integration interval due to this dispersion. To estimate the maximum error ΔE_{Fluc} a calculation of the thermal energy at the inertially cooled components is done for $\Delta(\Delta T) = 0.1$ K: with the integration times and average flow rates on the basis of a typical NBI commissioning pulse, namely 20181008n1257, with both sources, $U = 54$ kV, and $t_{NBI} = 5.2$ s, the impact of the simulated $\Delta(\Delta T) = 0.1$ K fluctuation on the energy calculation is:

  $$\Delta E_{Fluc} = c\rho \left(25\,\mathrm{s} < \dot{V}_{Pulse} > + (t_1 - t_0 - 25\,\mathrm{s}) < \dot{V}_{Pause} >\right) \Delta(\Delta T). \tag{4.7}$$

  The absolute errors are expected to be roughly the same for all pulses, because the flow rate setting is fixed and the integration time only varies a little. The relative error will increase with decreasing electric beam energy. The input values and the results are listed in Tab. 4.9. The box exit scraper is only hit by the beam for in-vessel pulses, therefore, the data is taken from in-vessel pulse 20181009.016. The values for the GDGN are from the reference pulse for the GDGN heat load with ID 20180924n1422.

  The calculated energies for the inertially cooled components stay below 1 % energy fraction each.

  The error due to fluctuations in the inlet water temperature and finite integration is estimated to be less than 2.2 % energy fraction in total for typical NBI pulses.

- FLOW RATE SIGNAL DISTURBANCE – $\dot{V}$
  The flow rate signals of all panels, the plasma grids and RF sources are disturbed. The disturbance and the linear correction method is described in Sec. 4.1.1. There is a statistical error due to the linear correction. Taking the measurement points closest to the disturbance, so the last physical realistic value right before and after the RF power pulse, as lower and upper boundary for the time during the disturbance gives the error estimate on the flow rate. Including these boundary flow rates in the calculation of the energy in the cooling water gives the error

Table 4.9: Error for inertially cooled components of the injector box due to non-constant temperature of the inlet cooling water. The error in the energy fraction (ΔEF_{Fluc}) is calculated with the electric beam energy of 51 MJ of 20181008n1257. All values for the box exit scraper are from the in-vessel pulse 20181009.016. The values for the GDGN are from the commissioning pulse 20180924n1422.

COMPONENT	$<\dot{V}>$ PULSE/PAUSE [m^3/h]		$t_1 - t_0$ [s]	E [MJ]	ΔE_{Fluc} [MJ]	ΔEF_{Fluc} [%]
RF Sources	11.4	7.9	291	2.0	0.3	0.5
Plasma Grids	11.8	9.3	25	0.7	<0.1	<0.1
GDGNs	19.7	14.0	166	0.5	0.3	0.6
Neutralisers 2	0.9	0.9	655	3.4	0.1	0.1
H^+ Dumps	1.0	1.1	655	3.9	0.1	0.2
Calorimeter	4.7	4.8	655	1.3	0.4	0.7
Box Exit Scraper	0.4	0.2	406	0.2	<0.1	<0.1
Sum					1.2	2.2

estimate on the energy measurement due to the linear correction. This is done exemplarily for 20181008n1257, a typical NBI pulse with $U = 54\,\text{kV}$ and a beam time of $t_{NBI} = 5.2\,\text{s}$. The uncertainty of the measured energy at the calorimeter panels is up to ±4 %, at the H^+ dump it is up to ±2 %, at the H_2^+ dump the uncertainty is up to ±2 %, at the plasma grids it is up to ±1 %, and at the RF sources it is up to ±0.5 %. This adds up to an error of the total measured energy of about ±2 % energy fraction.

- SPECIFIC HEAT CAPACITY AND DENSITY OF WATER – $c\rho$
  The product of specific heat capacity and density of water vary in the range of $\sigma_{c\rho} = 1.9\,\%$ for pressures from 1 to 16 bar and temperatures from 20 °C to 60 °C. A specific heat capacity of $c_p = 4182\,\text{J}/(\text{kg}\,\text{K})$ and density of $\rho = 998.2\,\text{kg}/\text{m}^3$ are used for all calculations [38].

4.3.3 *Conclusion*

In this section the discussed errors are summarised to overall errors of the derived energies of the individual components and the injected power exemplarily for the commissioning pulse 20181009n0718 and in-vessel pulse 20181009.016.
The following errors ar neglected:

- The error due to finite integration time is considered negligible for all pulse data presented in this thesis.
- The error due to thermal radiation of the actively cooled components, inertially cooled components and the pipes is negligible.
- The error due to heat conduction to the support frames is considered negligible.

- The error in the flow rate of the dumps due to the combined measurement is not estimated.
- The error in the flow rate due to bypasses for the components of S5 and S6 is considered negligible.
- The error of the comparability of the commissioning and the in-vessel pulse cannot be estimated.

The other errors are combined to the overall absolute error of the energy measurement ΔE for every individual component (cf. Eq. 4.6):

$$E + \Delta E \quad = \quad c\rho(1 + \sigma_{c\rho}) \int_{t_0}^{t_1} \dot{V}\,(1 + \sigma_{\dot{V}})\,(\Delta T + \Delta(\Delta T))\,\mathrm{d}t + \Delta E_{NP} + \Delta E_{TR}. \tag{4.8}$$

The error in the measured energy is calculated with the positive error values and the data of commissioning pulse 20181009n0718 and in-vessel pulse 20181009.016. The error of the measured energy at the GDGNs is determined with the pulse data of 20180924n1422. This data is presented in Tab. 4.11. All individual errors included in Eq. 4.8 are listed in Tab. 4.10. The overall errors on the measured energies on the components are listed in both tables.

The product of specific heat capacity and density of water vary in the range of $\sigma_{c\rho} = 1.9\,\%$. The flow rate signals have measurement uncertainties of $\sigma_{\dot{V}} = 0.8\,\%$ and $5\,\%$ specified by the manufacturer. Where the flow rate signal $\dot{V}$ is disturbed, a constant equal to the first physical reasonable value after the disturbance is used instead of the linear interpolation. The uncertainty in the rise in temperature consists of the observed uncertainties $\Delta(\Delta T) = 0.02\,\mathrm{K}$ for all components in the injector box and additional $\Delta(\Delta T) = 0.1\,\mathrm{K}$ for the inertially cooled components of the injector box due to fluctuations. The uncertainty in the measured energy due to the error in the temperature change of the water of the vessel components ΔE_{NP} was estimated separately. Therefore, it is added at the end. The thermal radiation losses in the beam dump of up to $\Delta E_{TR} = 0.16\,\mathrm{MJ}$ per source are also added at the end. This error is not separated for the baffle and the heat shield and therefore not included in the final error values of these components, but it is included in the final error of the beam dump. All these individual errors and the concluded errors on the measured energies on the components are listed in Tab. 4.10. The observed losses during the deflection process of about $\sigma_{E_D} = 8\,\%$ are not included in this calculation. In Tab. 4.11 the error margins of the calorimetrically measured energies at the NBI components are presented next to the measurement results for the commissioning pulse 20181009n0718 and the in-vessel pulse 20181009.016. These are the two pulses that are analysed in Sec. 4.1.2 *Energy Accountability*.

The injected power P_{inj} of an in-vessel pulse is derived from the power at the calorimeter position P_{cal} minus the power losses in the duct P_{duct}:

$$P_{inj} = P_{cal} - P_{duct}. \tag{4.9}$$

The energy losses in the duct are measured directly with calorimetry for the actual in-vessel pulse. The power at the calorimeter position cannot be measured directly. Therefore, the power at the calorimeter of a commissioning pulse is scaled with the ratio of the electric beam energies of the commissioning and the in-vessel pulse to get the power at the calorimeter position for the in-vessel pulse.

$$P_{inj} = \frac{E_{cal\ ac,\ com} + E_{cal\ ic,\ com}}{E_{el,\ com}} P_{el,\ vessel} - \frac{E_{BES,\ vessel} + E_{CC,\ vessel} + E_{DL,\ vessel}}{t_{NBI,\ vessel}}. \tag{4.10}$$

The index *BES* is for the box exit scraper, *CC* for the copper cone and *DL* for the duct liner. The index *com* or *vessel* shows, whether the value is taken from the commissioning or in-vessel pulse. $E_{cal,\ ac}$ is the energy of the actively cooled parts of the calorimeter and $E_{cal,\ ic}$ is the energy of the inertially cooled parts of the calorimeter. According to the rules of the propagation of errors, the summation and subtraction results in summation of the absolute errors and multiplication and division result in summation of the relative errors:

$$\text{summation and subtraction } (x = x_1 \pm x_2): \qquad \Delta x = \Delta x_1 + \Delta x_2, \tag{4.11}$$

$$\text{multiplication and division } (x = x_1 \divideontimes x_2): \qquad \sigma_x = \sigma_{x_1} + \sigma_{x_2}. \tag{4.12}$$

Thereby, the absolute error in the injected power is determined as

$$\Delta P_{inj} = \left(\frac{\Delta E_{cal\ ac,\ com} + \Delta E_{cal\ ic,\ com}}{E_{cal\ ac,\ com} + E_{cal\ ic,\ com}} + \frac{\Delta E_{el,\ com}}{E_{el,\ com}} + \frac{\Delta P_{el,\ vessel}}{P_{el,\ vessel}} \right) P_{cal} + \frac{\Delta E_{BES,\ vessel} + \Delta E_{CC,\ vessel} + \Delta E_{DL,\ vessel}}{t_{NBI,\ vessel}}. \tag{4.13}$$

with

$$\frac{\Delta E_{el,\ com}}{E_{el,\ com}} = \left[\left(\frac{\Delta U_{S7}}{U_{S7}} + \frac{\Delta I_{S7}}{I_{S7}} \right) E_{el,\ S7} + \left(\frac{\Delta U_{S8}}{U_{S8}} + \frac{\Delta I_{S8}}{I_{S8}} \right) E_{el,\ S8} \right] \frac{1}{E_{el,\ S7} + E_{el,\ S8}}, \tag{4.14}$$

and

$$\frac{\Delta P_{el,\ vessel}}{P_{el,\ vessel}} = \left[\left(\frac{\Delta U_{S7}}{U_{S7}} + \frac{\Delta I_{S7}}{I_{S7}} \right) P_{el,\ S7} + \left(\frac{\Delta U_{S8}}{U_{S8}} + \frac{\Delta I_{S8}}{I_{S8}} \right) P_{el,\ S8} \right] \frac{1}{P_{el,\ S7} + P_{el,\ S8}}. \tag{4.15}$$

Thus, the maximum error in the injected power of in-vessel pulse 20181009.016 is $\Delta P_{inj} = 0.8\,\text{MW}$ corresponding to $\sigma_{P_{inj}} = 24.4\,\%$.

Table 4.10: Individual errors that are taken into account for the overall error estimate. The error margins of the electric beam energy and power are dominated by the error of the supplied acceleration voltage U and the extracted current I_{ext}. The error margins of the calorimetrically measured energy (ΔE, σ_E) at a component are propagated from the error of the specific heat capacity and density of water $\sigma_{c\rho}$, the uncertainty of the flow rate measurement $\sigma_{\dot{V}}$ and the error in the temperature measurement. The latter consists of the observed uncertainty – fluctuations included – of the temperature measurement for the components of the injector box $\Delta(\Delta T)$ and of the error in the temperature measurement due to noise and plasma operation ΔE_{NP} and losses due to thermal radiation ΔE_{TR} for the duct and vessel components. The error due to thermal radiation of the beam dump is estimated for the whole beam dump and therefore not included in the error estimates of the single components heat shield and baffle, marked with **. The flow rate signal disturbances are also taken into account. The components with affected flow rate signals are marked with *. Actively cooled (ac) and inertially cooled (ic) parts of H^+ dumps and calorimeter are listed separately.

PARAMETER	ABS. ERROR	REL. ERROR [%]
Acc. Voltage one source	2.0 kV	3.7
Ext. Current one source	1.5 A	1.7
El. Power one source	0.3 MW	5.3
El. Energy one source	1.3 MJ	5.3

COMPONENT	$\sigma_{c\rho}$ [%]	$\sigma_{\dot{V}}$ [%]	$\Delta(\Delta T)$ [K]	ΔE_{NP} [MJ]	ΔE_{TR} [MJ]	ΔE [MJ]	σ_E [%]
RF Sources*	1.9	0.8	0.12	-	-	0.4	19.2
Plasma Grids*	1.9	0.8	0.12	-	-	0.1	9.4
GDGNs	1.9	0.8	0.12	-	-	0.2	35.4
Neutralisers 2	1.9	0.8	0.12	-	-	0.2	4.5
H_2^+ Dumps*	1.9	0.8	0.02	-	-	0.1	5.3
H^+ Dumps ac*	1.9	0.8	0.02	-	-	0.5	5.1
H^+ Dumps ic	1.9	0.8	0.12	-	-	0.2	4.9
Calorimeter ac*	1.9	0.8	0.02	-	-	1.1	5.6
Calorimeter ic	1.9	0.8	0.12	-	-	0.4	24.4
Box Exit Scraper	1.9	0.8	0.12			0.1	8.7
Copper Cone	1.9	5	-	<0.1		0.2	14.6
Duct Liner	1.9	5	-	0.2		0.3	18.1
Heat Shield	1.9	5	-	0.3	**0.15x	**0.3	**49.4
Baffle	1.9	5	-	0.3	**0.15(1-x)	**0.3	**96.8

Table 4.11: Final results with error estimates for calorimetrically measured energies at the individual NBI components, the injected power, box losses, duct losses and beam dump, exemplarily for 20181009n0718 and 20181009.016. GDGN values are taken from 20180924n1422. The error due to thermal radiation of the beam dump is estimated for the whole beam dump and is therefore not included in the error estimate of the single components heat shield and baffle, marked with **.

PARAMETER	VALUE		ERROR		VALUE		ERROR	
NBI Pulse ID	20181009n0718				20181009.016			
Pulse Type	commissioning				in-vessel			
Beam Time [s]	5.2				4.0			
Acc. Voltage S7 [kV]	54.2				53.1			
Acc. Voltage S8 [kV]	54.1				53.0			
Ext. Current S7 [A]	86.7				87.6			
Ext. Current S8 [A]	86.5				88.4			
El. Power S7 [MW]	4.7				4.7			
El. Power S8 [MW]	4.7				4.7			
El. Energy S7 [MJ]	24.4				18.6			
El. Energy S8 [MJ]	24.3				18.7			
COMPONENT	E [MJ]	EF [%]	ΔE [MJ]	σ_E [%]	E [MJ]	EF [%]	ΔE [MJ]	σ_E [%]
RF Sources	1.9	4.0	+0.4	+19.2				
Plasma Grids	0.7	1.5	+0.1	+9.4				
GDGNs	0.5	2.1	+0.2	+35.4				
Neutralisers 2	3.8	7.8	+0.2	+4.5				
H_2^+ Dumps	1.1	2.3	+0.1	+5.3				
H^+ Dumps ac	8.2	16.7	+0.5	+5.1				
H^+ Dumps ic	4.1	8.5	+0.2	+4.9				
Calorimeter ac	18.1	37.1	+1.1	+5.6				
Calorimeter ic	1.3	2.8	+0.4	+24.4				
Box Exit Scraper					0.2	0.6	+0.1	+8.7
Copper Cone					0.8	2.1	+0.2	+14.6
Duct Liner					1.5	3.9	+0.3	+18.1
Heat Shield					0.6	1.6	**+0.3	**+49.4
Baffle					0.3	0.7	**+0.3	**+96.8
Measured Total	39.3	80.6	+2.7	+6.7	19.3	51.6	+2.2	+11.3
Box Losses	6.4	13.2	+0.7	+9.5				
Duct Losses					2.5	6.6	+0.4	+16.1
Beam Dump					0.8	2.3	**+0.9	**+100.4
Total Injected Power					(3.1 ± 0.8) MW (± 24.4 %)			

5

CONCLUSION AND OUTLOOK

In this thesis, the performance of the Neutral Beam Injection (NBI) system at Wendelstein 7-X (W7-X) has been investigated. NBI is one of the two main heating systems at W7-X. It is therefore important to optimise the performance of the NBI system for high injected power. Furthermore, the determination of the injected power is crucial inferring the energy confinement time.

To analyse the conversion of initially generated electric beam power to injected beam power, the heat loads on the individual NBI components were examined with calorimetry. The evaluation routine developed in the frame of this thesis utilises all measurement data on the temperature and flow rate of the cooling water of the individual NBI components for a single NBI pulse. It then calculates the energy in the cooling water of each component individually, depending on the cooling method of the component. This energy corresponds approximately to the heat load and thus to the conversion losses at the components.

The injected neutral beam power of both installed sources combined was determined with calorimetry to be (3.1 ± 0.8) MW for 20181009.016. This is about 33 % of the initially generated electric beam power of (9.4 ± 0.6) MW. The absorption by a plasma with $T_i \approx T_e \approx 1.3$ keV and $n_e \approx 4 \times 10^{19}/\mathrm{m}^3$ is calculated to be about 90 %. The injected beam power was validated by the comparison of beam emission evaluated with the Fast-Ion D_α Simulation (FIDASIM) by Poloskei et al. [9–11]. Moreover, within the error margins the injected beam power is consistent with that of the comparable NBI system of ASDEX Upgrade (W7-X) [29].

With the calorimetric analysis of the heat loads on the individual NBI components, about (89 ± 6) % of the initially generated electric beam energy can be accounted for. For the NBI system of AUG, with 98 %, the energy accountability is almost complete [29]. There are indications, that around 8 % of the initially generated electric beam energy of of the W7-X NBI system are deflected to uncooled components. Moreover, higher heat loads than at AUG were detected at the outer parts and lower heat loads at the central parts of the H^+ dumps and calorimeter. This could be caused by space charge expansion of the ions in the deflection magnet. Without the calorimetric measurements at the magnet liners no conclusion can be drawn. Further investigations are needed to study the energy and particle flow in the magnet region. The losses in the duct are measured to be about (7 ± 1) % of the initially generated beam energy. The calorimetrically measured energies at the duct and beam dump components were validated against the Beamlet Based NBI (BBNBI) model for an NBI pulse into the empty plasma vessel.

Furthermore, the conversion losses have been analysed for NBI pulses with different operating parameters. This way, it was possible to draw conclusions on physical processes causing the losses and some operating parameters could be optimised for low conversion losses and thus high injected power: Rising neutralisation efficiency and decreasing conversion losses were observed with increasing neutral gas flow rate in the range from 21 to 31 mbar l/s in the neutraliser. And the neutralisation efficiency decreased from 51 to 42 % with increasing acceleration voltage from 39.7 to 54.0 kV.

Both observations are consistent with the theoretical dependency of the neutralisation efficiency on the neutraliser gas density, also called target thickness, and the acceleration voltage. A high acceleration voltage is indispensable for a high injected power per particle. Thus, the neutral gas flow rate was adjusted to achieve a higher neutralisation efficiency. Additionally, the deflection process used to separate the neutrals from the ions has been investigated. The comparison of two pulses with and without operation of the deflection magnet showed additional losses of about 8 % of the initially generated electric beam energy for the pulse with operation of the magnet. The explanation is that the energy loss is partially due to deflected molecular ions. According to calculations and simulations [39, 40], approximately 3 % are expected to be due to deflected H_2^+ ions that miss the H_2^+ dump. Additionally, reionisation and neutralisation along the beam path in the magnetic field of the deflection magnet lead to modifications of the typical trajectories, not all of which end on the calorimetrically observed components. Further measurements are required to calculate the actual amount of ions that are not hitting one of the intended ion dumps. Moreover, the penetration of the deflection field into the neutralisers could be an additional reason for misguided ions which could be the cause for higher heat loads at the neutralisers, as they are in fact observed.

The dependence of the performance of the beam sources on the magnetic stray field of W7-X has been studied. No clear dependence of the source performance on the stray fields of three different magnetic field configurations (KJM, EJM, and FHS) or on the operation of the trim coil located between the injectors was observed. Independent of the stray field, the performance of S7 was better than that of S8. The cause is not clear.

The main contribution to the errors of the calorimetry results are in the temperature and flow rate measurements. In addition, the measurement errors of the acceleration voltage and the extracted current contribute significantly to the errors of both the calorimetry results and the stray field analysis. Therefore, the most promising improvements to the NBI system at W7-X for greater accuracy of the results are connected to the measurement of these four parameters. First of all, the measurement of the acceleration voltage and the extracted current could be improved. This would increase the accuracy of the initially generated electric beam energy and power and therefore the accuracy of the energy accountability and the injected power. Second, the measurement of temperature and flow rate at some NBI components could be improved. At present, there is no temperature and no flow rate measurement at the magnet liners and the temperature sensors at the ground and deceleration grids and the first part of the neutralisers and the flowmeters at the H_2^+ dumps are defect. Therefore, the energy at the magnet liners, the ground and deceleration grids and the first part of the neutralisers could not be determined. Installation or repair of the sensors would help to study the energy and particle flow at the acceleration grids, in the neutraliser and in the magnet region. Additional sensors would improve the energy accountability and would allow further optimisation of the operating parameters, such as the neutraliser gas settings or the deflection process.

For the duct and beam dump components, the errors due to noise of the signals and due to the low sampling rate and rough binning of the inlet water temperature measurement could be reduced by installing sensors with higher precision of flow rate and temperature. Individual measurement of the beam dump instead of the total heat shield and baffle modules would also increase the signal to noise ratio and decouple the temperature signal from plasma operation and heat conduction. This way, the accuracy of the calorimetry for duct and beam dump and therefore of injected power and absorbed power could be increased. Moreover, the flow rate signals of some NBI components show a disturbance coinciding with the Radio Frequency (RF) source power pulses and the high voltage pulses. The affected components are the plasma grids, the RF sources and all actively cooled components, namely the H_2^+ dumps and the centre parts of the calorimeter and the centre parts of the H^+ dumps. Eliminating these signal disturbances would increase the precision of the calorimetry results for these components and therefore, of the energy accountability and injected power. Facilitating the calorimetric analysis for every NBI pulse, the pause between pulses has to be set to at least 10 min. Moreover, the pause interval has to be increased in the case of longer NBI pulses or larger NBI power, e.g. for deuterium operation. The injected power is investigated by comparing the in-vessel pulse of interest to a pulse onto the calorimeter. Therefore, one pulse onto the calorimeter has to be carried out for every in-vessel pulse operating parameter setting to maximise the comparability of the pulses and thus to determine the injected power more precisely. Further systematic scans of operating parameters, such as the RF source gas setting, the neutraliser gas setting at higher acceleration voltage or the current of the coils in the deflection magnet are planned for the commissioning of the second injector NI20 and the restart of the injector which was studied in this thesis (NI21). Furthermore, investigation of the perveance and research on the losses at the RF sources in dependency of the beam time are intended.

a

APPENDIX A: COOLING WATER CIRCUIT DIAGRAMS

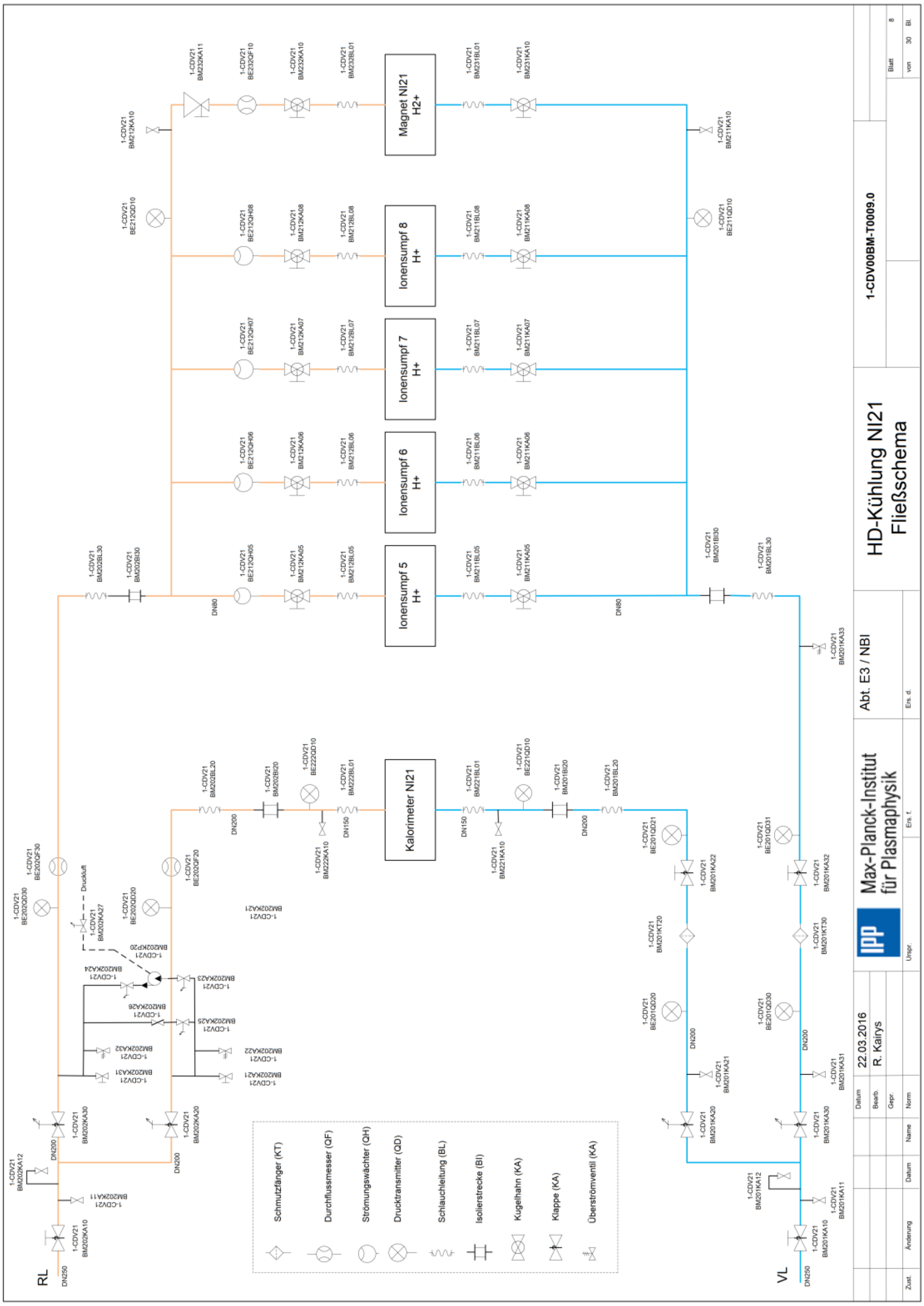

Magnet NI21 H2+
Ionensumpf 8 H+
Ionensumpf 7 H+
Ionensumpf 6 H+
Ionensumpf 5 H+
Kalorimeter NI21
RL
VL
Druckluft
Schmutzfänger (KT)
Durchflussmesser (QF)
Strömungswächter (QH)
Drucktransmitter (QD)
Schlauchleitung (BL)
Isolierstrecke (BI)
Kugelhahn (KA)
Klappe (KA)
Überströmventil (KA)
HD-Kühlung NI21
Fließschema
1-CDV00BM-T0009.0
Max-Planck-Institut für Plasmaphysik
IPP
Abt. E3 / NBI
22.03.2016
R. Kairys
Datum
Bearb.
Gepr.
Norm
Urspr.
Ers. f.
Ers. d.
Zust.
Änderung
Name
Blatt 8
von 30 Bl.

Figure a.1: Piping and instrumentation diagram of the high flow rate water cooling circuit.

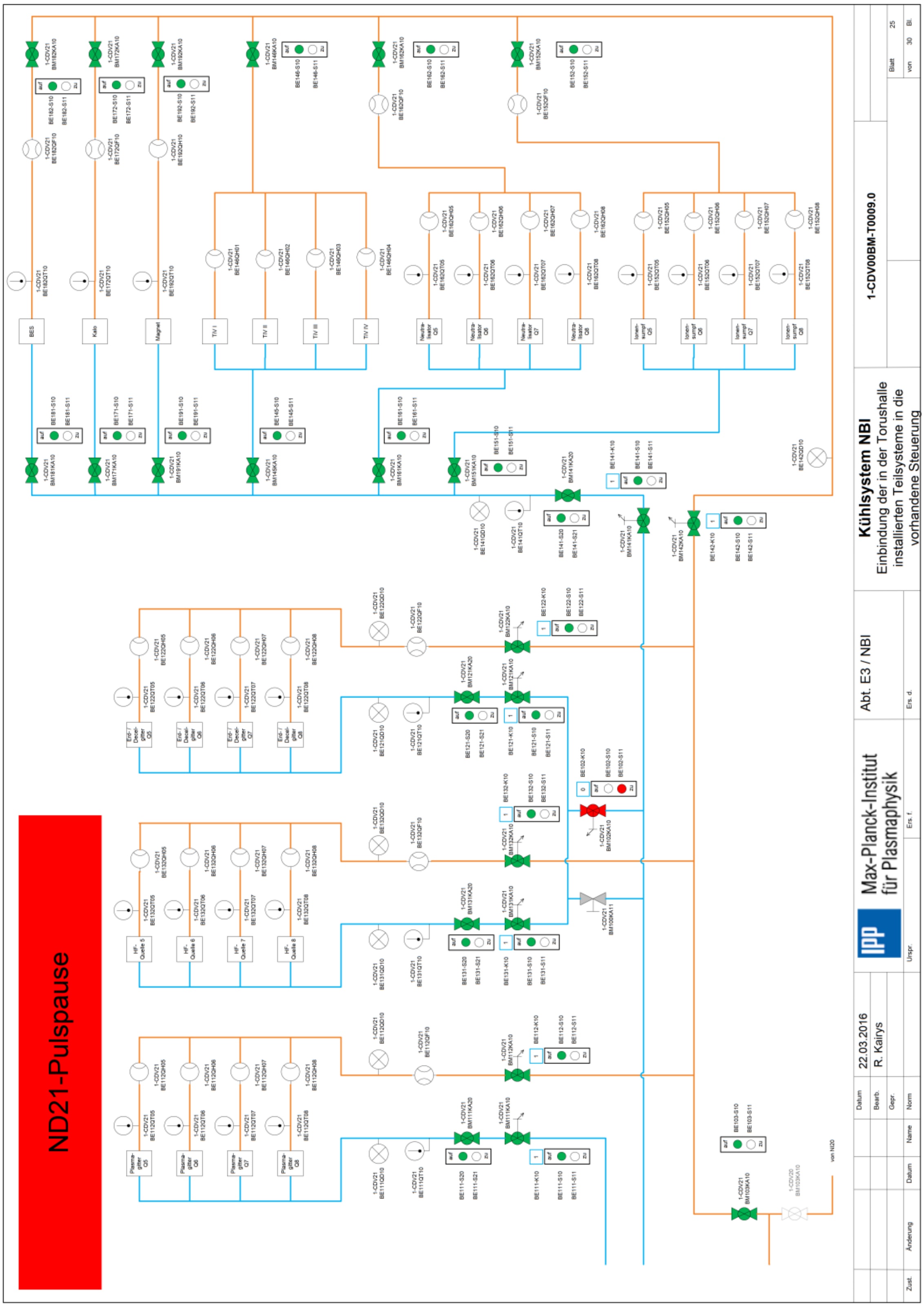
ND21-Pulspause
Kühlsystem NBI
Einbindung der in der Torushalle installierten Teilsysteme in die vorhandene Steuerung
1-CDV00BM-T0009.0
Abt. E3 / NBI
Max-Planck-Institut für Plasmaphysik
22.03.2016
R. Kairys
Blatt 25
von 30 Bl
BES
Kalo
Magnet
TIV I
TIV II
TIV III
TIV IV

Figure a.2: Piping and instrumentation diagram of the low flow rate water cooling circuit.

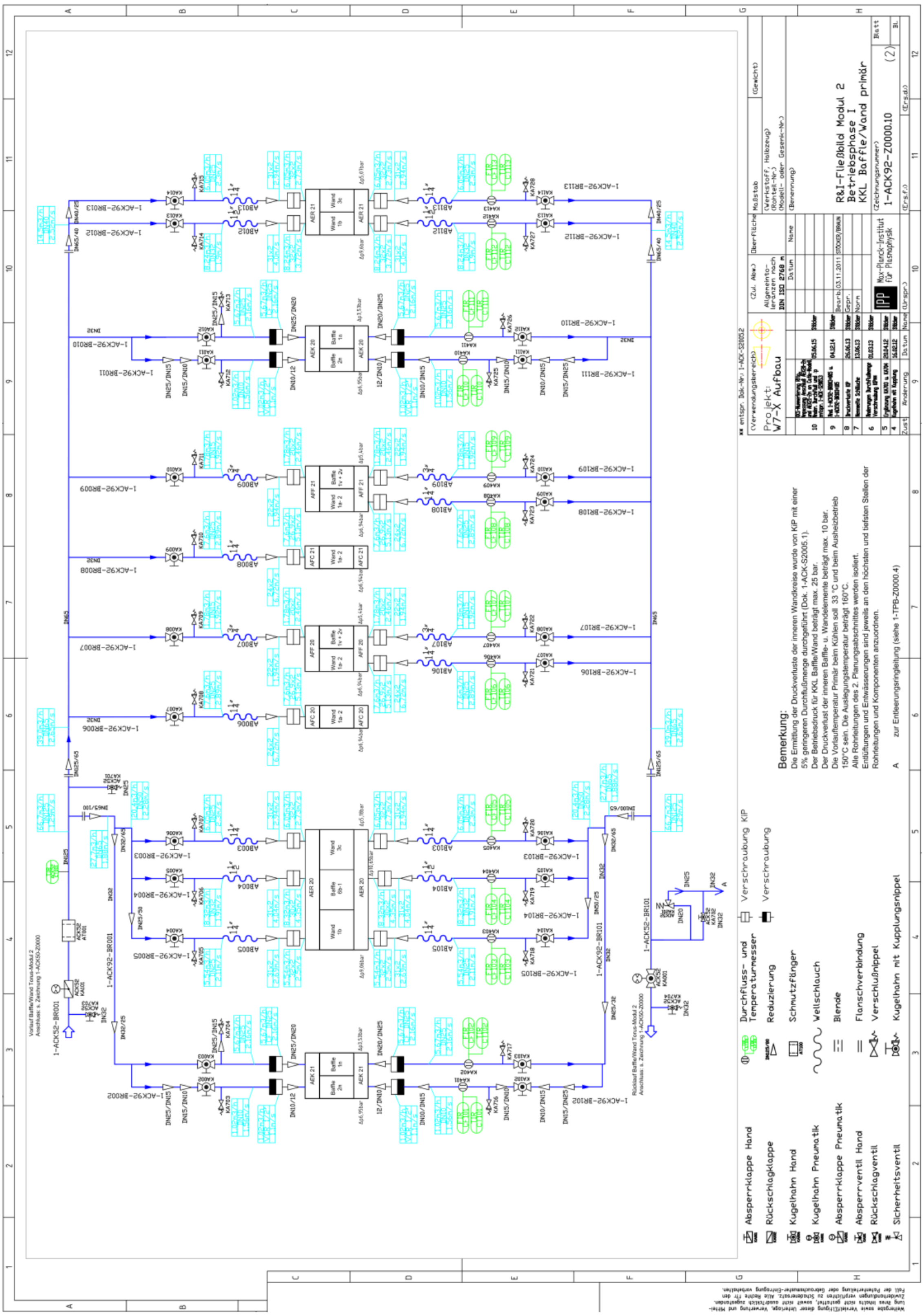

Vorlauf Baffle/Wand Torus-Modul 2
Anschluss: s. Zeichnung 1-ACK50-Z0000
1-ACK52-BR001
1-ACK92-BR001
Rücklauf Baffle/Wand Torus-Modul 2
Anschluss: s. Zeichnung 1-ACK50-Z0000
1-ACK52-BR101
1-ACK92-BR101
AEK 21
AER 20
AFC 20
AFF 20
AFC 21
AFF 21
AEK 20
AER 21
Absperrklappe Hand
Rückschlagklappe
Kugelhahn Hand
Kugelhahn Pneumatik
Absperrklappe Pneumatik
Absperrventil Hand
Rückschlagventil
Sicherheitsventil
Durchfluss- und Temperaturmesser
Reduzierung
Schmutzfänger
Wellschlauch
Blende
Flanschverbindung
Verschlußnippel
Kugelhahn mit Kupplungsnippel
Verschraubung KiP
Verschraubung
** entspr. Dok.-Nr.: 1-ACK-S2005.2
(Verwendungsbereich)
Projekt:
W7-X Aufbau
(Zul. Abw.)
Allgemeintoleranzen nach
DIN ISO 2768 m
Oberfläche
Maßstab
(Gewicht)
(Werkstoff, Halbzeug)
(Rohteil-Nr.)
(Modell- oder Gesenk-Nr.)
(Benennung)
Datum
Name
Bearb. 03.11.2011 STÖCKER/BRAUN
Gepr.
Norm
R&I-Fließbild Modul 2
Betriebsphase I
KKL Baffle/Wand primär
IPP Max-Planck-Institut für Plasmaphysik
(Zeichnungsnummer)
1-ACK92-Z0000.10
(2)
Blatt
Bl.
Zust.
Änderung
Datum
Name
(Urspr.)
(Ers.f.:)
(Ers.d.:)

Bemerkung:

Die Ermittlung der Druckverluste der inneren Wandkreise wurde von KiP mit einer 5% geringeren Durchflußmenge durchgeführt (Dok. 1-ACK-S2005.1).
Der Betriebsdruck für KKL Baffle/Wand beträgt max. 25 bar.
Der Druckverlust der inneren Baffle- u. Wandelemente beträgt max. 10 bar.
Die Vorlauftemperatur Primär beim Kühlen soll 33 °C und beim Ausheizbetrieb 150°C sein. Die Auslegungstemperatur beträgt 160°C.
Alle Rohrleitungen des 2. Planungsabschnittes werden isoliert.
Entlüftungen und Entwässerungen sind jeweils an den höchsten und tiefsten Stellen der Rohrleitungen und Komponenten anzuordnen.

A zur Entleerungsringleitung (siehe 1-TPB-Z0000.4)

Figure a.3: Piping and instrumentation diagram of the water cooling circuit for the vessel components in the NBI region of W7-X.

b

APPENDIX B: PULSE AND CALORIMETRY DATA

Table b.1: Source parameters and energy fractions of commissioning pulses 20180823n0731 and 20180823n0754 and in-vessel pulse 20180823.037 for BES comparison. Source parameters are listed in the first part and calorimetrically measured energy fractions of the components in the second part of the table. *Box losses* is the sum of the energy fractions of RF sources, plasma grids and the second parts of the neutralisers. *Duct losses* is the sum of the energy fractions of box exit scraper, copper cone and the duct liner. The energy at the calorimeter for the in-vessel pulse is expected to be due to the deflection process (**, cf. Sec. 4.1.3 *Influence of the Deflection Magnet*).

PARAMETER	VALUES FOR THE THREE PULSES			
NBI Pulse ID	20180823n0731	20180823n0754	20180823.037	
Pulse Type	commissioning S7	commissioning S8	in-vessel (S7 | S8)	
Beam Time [s]	6.7	6.6	1.2	1.2
Acc. Voltage [kV]	47.3	47.3	47.3	47.3
Ext. Current [A]	78.9	78.4	79.5	78.4
El. Power [MW]	3.7	3.7	3.8	3.7
El. Energy [MJ]	25.1	24.6	4.5	4.5
COMPONENT	ENERGY FRACTIONS OF THE THREE PULSES [%]			
RF Sources	3.9	3.8	5.2	
Plasma Grids	1.4	1.4	2.4	
Neutralisers 2	7.1	7.2	8.9	
H_2^+ Dumps	2.7	2.4	2.6	
H^+ Dumps ac	15.4	12.6	13.4	
H^+ Dumps ic	6.7	6.9	7.8	
Calorimeter ac	38.4	40.8		
Calorimeter ic	4.3	3.7	**1.6	
Box Exit Scraper			0.8	
Copper Cone			2.7	
Duct Liner			5.0	
Heat Shield			2.2	
Baffle			1.6	
Measured Total	80.0	78.7	52.6	
Box Losses	12.4	12.4	16.5	
Duct Losses			8.4	
Total Injected Power				2.7 MW

BIBLIOGRAPHY

1. Stocker, T. *et al.* Climate Change 2013: The Physical Science Basis. Contribution of Working Group I to the Fifth Assessment Report of the Intergovernmental Panel on Climate Change. *IPCC 2013,* 1535.
2. JET Team. Fusion Energy Production From a Deuterium-Tritium Plasma in the JET Tokamak. *Nuclear Fusion* **32,** 187–203. DOI: `10.1088/0029-5515/32/2/i01` (Feb. 1992).
3. Keilhacker, M. *et al.* The Scientific Success of JET. *Nuclear Fusion* **41,** 1925–1966. DOI: `10.1088/0029-5515/41/12/217` (Dec. 2001).
4. McGuire, K. M. *et al.* Review of Deuterium–Tritium Results From the Tokamak Fusion Test Reactor. *Physics of Plasmas* **2,** 2176–2188. DOI: `10.1063/1.871303` (1995).
5. Keilhacker, M. *et al.* High Fusion Performance From Deuterium-Tritium Plasmas in JET. *Nuclear Fusion* **39,** 209–234. DOI: `10.1088/0029-5515/39/2/306` (Feb. 1999).
6. Wesson, J. & Campbell, D. J. *Tokamaks* ISBN: 9780198509226 (Clarendon Press, 2004).
7. Pedersen, T. S. *et al.* First Results From Divertor Operation in Wendelstein 7-X. *Plasma Physics and Controlled Fusion* **61,** 014035. DOI: `10.1088/1361-6587/aaec25` (Nov. 2018).
8. Stäbler, A. *et al. Design of the Neutral Beam Injection System for ASDEX-Upgrade* in *15th Symposium on Fusion Technology (SOFT 1988)* (Elsevier Science Publishers B.V., 1989), 620–624.
9. Poloskei, P. Z. *et al. Analysis of Balmer Alpha Spectra in W7-X Using FIDASIM* poster P2.1055, 46th European Physical Society Conference on Plasma Physics, Milan, Italy. July 2019.
10. Poloskei, P. Z. *et al. FIDASIM Simulations for Wendelstein 7-X to Predict Balmer-Alpha Spectra* in preperation. 2020.
11. Ford, O. P. *et al.* Charge Exchange Recombination Spectroscopy at Wendelstein 7-X. *Review of Scientific Instruments* **91,** 023507. DOI: `10.1063/1.5132936` (2020).
12. Speth, E. Neutral Beam Heating of Fusion Plasmas. *Reports on Progress in Physics* **52,** 57–121. DOI: `10.1088/0034-4885/52/1/002` (Jan. 1989).
13. Gradic, D. *Plasma Start-Up in Wendelstein 7-X With Neutral Beam Injection* MA thesis (Ernst Moritz Arndt Universität Greifswald, 2013).
14. Conrads, H. & Schmidt, M. Plasma Generation and Plasma Sources. *Plasma Sources Science and Technology* **9,** 441–454. DOI: `10.1088/0963-0252/9/4/301` (2000).
15. Tabata, T. & Shirai, T. Analytic Cross Sections for Collisions of H+, H2+, H3+, H, H2, and H- With Hydrogen Molecules. *Atomic Data and Nuclear Data Tables* **76,** 1–25. DOI: `10.1006/adnd.2000.0835` (2000).
16. Berkner, K. H., Pyle, R. V. & Stearns, J. W. Intense, Mixed-Energy Hydrogen Beams for CTR Injection. *Nuclear Fusion* **15,** 249–254. DOI: `10.1088/0029-5515/15/2/009` (1975).

17. Wei, J. L. *et al.* Optimization of the Gas Flow in the Neutralization Region of EAST Neutral Beam Injector. *Fusion Engineering and Design* **88,** 3176–3179. DOI: `10.1016/j.fusengdes.2013.09.014` (2013).
18. Prelec, K. *Negative Ion Based Neutral Beams for Plasma Heating* tech. rep. (Brookhaven National Laboratory, 1978).
19. Stix, T. H. Heating of Toroidal Plasmas by Neutral Injection. *Plasma Physics* **14,** 367–384. DOI: `10.1088/0032-1028/14/4/002` (1972).
20. Wolf, R. C. *et al.* Motional Stark Effect Measurements of the Local ICRH Induced Diamagnetism in JET Plasmas. *Nuclear Fusion* **33,** 1835–1847. DOI: `10.1088/0029-5515/33/12/307` (1993).
21. Demtröder, W. *Mechanics and Thermodynamics* 452. ISBN: 9783319278773 (Springer International Publishing, 2017).
22. *VDI Heat Atlas* 2nd ed. ISBN: 9783540778776 (Springer Berlin Heidelberg, Berlin, Heidelberg, 2010).
23. Nocentini, R. *et al.* Design of the Torus Interface for the Neutral Beam Injectors of Wendelstein 7-X. *Fusion Engineering and Design* **100,** 453–460. DOI: `10.1016/j.fusengdes.2015.07.016` (2015).
24. Rust, N. *et al.* W7-X Neutral-Beam-Injection: Selection of the NBI Source Positions for Experiment Start-Up. *Fusion Engineering and Design* **86,** 728–731. DOI: `10.1016/j.fusengdes.2011.03.054` (2011).
25. Lazerson, S. *et al. Predictions of Neutral Beam Deposition and Energetic Particle Losses in W7-X* 43rd EPS Conference on Plasma Physics. European Physical Society. `http://www.euro-fusionscipub.org/wp-content/uploads/WPS1CP16_15275_submitted.pdf`. 2016.
26. Franzen, P. *et al.* Beam Current Feedback Regulation of the RF Neutral Beam Sources of ASDEX Upgrade. *Fusion Engineering and Design* **56-57,** 487–491. DOI: `10.1016/S0920-3796(01)00331-3` (2001).
27. Speth E. and Ciric, M. *et al.* Rf Ion Sources for Fusion Applications: Design, Development and Performance. *Fusion Engineering and Design* **46,** 383–388. DOI: `10.1016/S0920-3796(99)00030-7` (Nov. 1999).
28. McNeely, P. *et al.* Current Status of the Neutral Beam Heating System of W7-X. *Fusion Engineering and Design* **88,** 1034–1037. DOI: `10.1016/j.fusengdes.2013.03.006` (2013).
29. Stäbler, A. *et al.* Performance of the First ASDEX Upgrade Neutral Beam Injector. *Fusion Technology 1994. Proceedings. Vol. 1,* 593–596. DOI: `10.1016/B978-0-444-82220-8.50116-3` (1995).
30. Feist, J.-H. *et al.* Performance of the Ion Removal System for the ASDEX-Upgrade Neutral Beam Injectors. *Fusion Technology 1992,* 486–490. DOI: `10.1016/B978-0-444-89995-8.50090-4` (Jan. 1993).
31. Holtum, D. *et al.* Calorimeter Design-Aspects for Neutral Beam Injection on W7-X. *Fusion Engineering and Design* **86,** 905–908. DOI: `10.1016/j.fusengdes.2011.04.046` (2011).

32. Orozco, G. *et al.* Reviewed Design of the High Heat Flux Panels for the AUG and W7-X Neutral Beam Calorimeter. *Fusion Engineering and Design* **146,** 2105–2109. DOI: `10.1016/j.fusengdes.2019.03.116` (2019).
33. Greuner, H. *et al.* Final Design of W7-X Divertor Plasma Facing Components - Tests and Thermo-Mechanical Analysis of Baffle Prototypes. *Fusion Engineering and Design* **66-68,** 447–452. DOI: `10.1016/S0920-3796(03)00193-5` (2003).
34. Boscary, J. *et al.* Design and Technological Solutions for the Plasma Facing Components of Wendelstein 7-X. *Fusion Engineering and Design* **86,** 572–575. DOI: `10.1016/j.fusengdes.2010.11.020` (2011).
35. Geiger, J. *et al.* Physics in the Magnetic Configuration Space of W7-X. *Plasma Physics and Controlled Fusion* **57.** DOI: `10.1088/0741-3335/57/1/014004` (Nov. 2014).
36. Kick, M. *et al.* Shielding of the NBI Boxes Against W7-X Magnetic Stray Fields. *Fusion Engineering and Design* **84.** Proceeding of the 25th Symposium on Fusion Technology, 1020–1025. DOI: `10.1016/j.fusengdes.2009.04.002` (2009).
37. Orozco, G. *et al.* AC Operation of Large Titanium Sublimation Pumps in a Magnetic Field: Results of the Test Stand for the W7-X Neutral Beam Injectors. *Fusion Engineering and Design* **89,** 3070–3077. DOI: `10.1016/j.fusengdes.2014.09.014` (2014).
38. *Heat Capacity and Density of Water, NIST Chemistry WebBook, NIST Standard Reference Database Number 69* (eds Linstrom, P. J. & Mallard, W. G.) (National Institute of Standards and Technology, Gaithersburg MD, 20899).
39. McNeely, P. & Kairys, R. Max Planck Institute for Plasma Physics Greifswald, Germany, private communication. 2019.
40. Den Harder, N. Max Planck Institute for Plasma Physics Garching, Germany, private communication. 2019.
41. Den Harder, N. *et al.* Modeling Neutral Beam Transport in Fusion Experiments: Studying the Effects of Reionisation and Deflection. *Fusion Engineering and Design* **146,** 518–521. DOI: `10.1016/j.fusengdes.2019.01.011` (2019).
42. Äkäslompolo, S. *et al.* Validating Fast-Ion Wall-Load IR Analysis-Methods Against W7-X NBI Empty-Torus Experiment. *Journal of Instrumentation* **14.** DOI: `10.1088/1748-0221/14/07/p07018` (July 2019).
43. Heidbrink, W. W. *et al.* A Code that Simulates Fast-Ion D_α and Neutral Particle Measurements. *Communications in Computational Physics* **10,** 716–741. DOI: `10.4208/cicp.190810.080211a` (2011).
44. Haskey, S. R. *et al.* Deuterium Charge Exchange Recombination Spectroscopy from the Top of the Pedestal to the Scrape Off Layer in H-Mode Plasmas. *Journal of Instrumentation* **12.** DOI: `10.1088/1748-0221/12/10/C10013` (2017).
45. Geiger, B. *et al.* Fast-Ion Transport in Low Density L-Mode Plasmas at TCV Using FIDA Spectroscopy and the TRANSP Code. *Plasma Physics and Controlled Fusion* **59.** DOI: `10.1088/1361-6587/aa8340` (2017).
46. Mühle, L. Ampegon AG, private communication. Mar. 2019.
47. Baehr, H. D. & Stephan, K. *Wärme- und Stoffübertragung* 9th ed. ISBN: 978-3-662-49676-3 (Springer-Verlag Berlin Heidelberg, 2016).

COLOPHON

This document was typeset using the typographical look-and-feel `classicthesis` developed by André Miede and Ivo Pletikosić. The style was inspired by Robert Bringhurst's seminal book on typography *"The Elements of Typographic Style"*. `classicthesis` is available for both LaTeX and LyX:

`https://bitbucket.org/amiede/classicthesis/`

Happy users of `classicthesis` usually send a real postcard to the author, a collection of postcards received so far is featured here:

`http://postcards.miede.de/`

Thank you very much for your feedback and contribution.